

Banner appropriate to article type will appear here in typeset article

1 **Spatio-temporal fluctuations of interscale and** 2 **interspace energy transfer dynamics in** 3 **homogeneous turbulence**

4 **H. S. Larssen¹† and J. C. Vassilicos^{2,1}‡**

5 ¹Department of Mathematics, Imperial College London, London SW7 2AZ, UK

6 ²Univ. Lille, CNRS, ONERA, Arts et Métiers ParisTech, Centrale Lille, UMR 9014 - LMFL - Laboratoire
7 de Mécanique des fluides de Lille - Kampé de Fériet, F-59000 Lille, France

8 (Received xx; revised xx; accepted xx)

9 We study fluctuations of all co-existing energy exchange/transfer/transport processes in
10 stationary periodic turbulence including those which average to zero and are not present
11 in average cascade theories. We use a Helmholtz decomposition of accelerations which
12 leads to a decomposition of all terms in the Kármán-Howarth-Monin-Hill (KMH) equation
13 (scale-by-scale two-point energy balance) causing it to break into two energy balances, one
14 resulting from the integrated two-point vorticity equation and the other from the integrated
15 two-point pressure equation. The various two-point acceleration terms in the Navier-Stokes
16 difference (NSD) equation for the dynamics of two-point velocity differences have similar
17 alignment tendencies with the two-point velocity difference, implying similar characteristics
18 for the NSD and KMH equations. We introduce the two-point sweeping concept and show
19 how it articulates with the fluctuating interscale energy transfer as the solenoidal part of the
20 interscale transfer rate does not fluctuate with turbulence dissipation at any scale above the
21 Taylor length but with the sum of the time-derivative and the solenoidal interspace transport
22 rate terms. The pressure fluctuations play an important role in the interscale and interspace
23 turbulence transfer/transport dynamics as the irrotational part of the interscale transfer rate
24 is equal to the irrotational part of the interspace transfer rate and is balanced by two-point
25 fluctuating pressure work. We also study the homogeneous/inhomogeneous decomposition
26 of interscale transfer. The statistics of the latter are skewed towards forward cascade events
27 whereas the statistics of the former are not. We also report statistics conditioned on intense
28 forward/backward interscale transfer events.

29 **Key words:**

† Email address for correspondence: h.larssen18@imperial.ac.uk
‡ Email address for correspondence: john-christos.vassilicos@cnsr.fr

30 1. Introduction

31 Modeling of turbulence dissipation is a cornerstone of one-point turbulent flow prediction
32 methods based on the Reynolds Averaged Navier Stokes (RANS) equations such as the
33 widely used $k - \varepsilon$ and the $k - \omega$ models (see Pope (2000), Leschziner (2016)) and also
34 of two-point turbulence flow prediction methods based on filtered Navier Stokes equations,
35 namely Large Eddy Simulations (LES) (see Pope (2000), Sagaut (2000)). The turbulence
36 dissipation rate away from walls is intimately linked to the turbulence cascade (Pope
37 2000; Vassilicos 2015). The physical understanding of this cascade which, to this day,
38 has underpinned these prediction methods is based on Kolmogorov's average cascade in
39 statistically homogeneous and stationary turbulence. Notwithstanding recent advances which
40 have shown that the turbulence dissipation and cascade are different from Kolmogorov's both
41 in non-stationary (see e.g. Vassilicos (2015); Goto & Vassilicos (2016); Steiros (2022)) and
42 in non-homogeneous turbulence (Chen *et al.* 2021; Chen & Vassilicos 2022), Kolmogorov's
43 cascade is in fact valid only as an *average* cascade even in homogeneous stationary turbulence.
44 Turbulence has been known to be intermittent since the late 1940s (see Frisch (1995) and
45 references therein), and this intermittency has mainly been taken into account as structure
46 function exponent corrections to Kolmogorov's average picture. However, studies such as
47 those by Schumacher *et al.* (2014) and Yasuda & Vassilicos (2018) examined intermittent
48 fluctuations without reference to structure function exponents which require high Reynolds
49 numbers to be well defined and to be predicted from Kolmogorov's theory or various
50 intermittency-accounting variants of this theory (see Frisch (1995) and references therein).
51 Yasuda & Vassilicos (2018) concentrated their attention on the actual fundamental basis
52 of Kolmogorov's theory which is scale-by-scale equilibrium for statistically homogeneous
53 and stationary turbulence, and not on the theory's structure function and energy spectrum
54 scaling consequences. The scale-by-scale equilibrium implied by statistical homogeneity and
55 stationarity is that the average interscale turbulence energy transfer rate is balanced by nothing
56 more than average scale-by-scale viscous diffusion rate, average turbulence dissipation rate
57 and average energy input rate by a stirring force, irrespective of Reynolds number (except
58 that the Reynolds number needs to be large enough for the presence of random fluctuations).
59 It is most natural for a study of intermittency to start with the fluctuations around this
60 balance, which means that along with the fluctuations of interscale transfer, dissipation,
61 diffusion and energy input, all other fluctuating turbulent energy change rates need to be taken
62 into account as well even if their spatio-temporal average is zero in statistically stationary
63 homogeneous turbulence. The intermittency corrections to Kolmogorov's average cascade
64 theory which have been developed since the 1960s (e.g. see Frisch (1995); Sreenivasan &
65 Antonia (1997)) are often based on the intermittent fluctuations of the local (in space and
66 time) turbulence dissipation rate, yet Yasuda & Vassilicos (2018) demonstrated that these
67 dissipation fluctuations are much less intense than the fluctuations of other turbulent energy
68 change rates such as the non-linear interspace energy transfer rate (which is a scale-by-
69 scale rate of turbulent transport in physical space), the fluctuating work resulting from the
70 correlation of the fluctuating pressure gradient with the fluctuating velocity and the time-
71 derivative of the scale-by-scale turbulent kinetic energy. Yasuda & Vassilicos (2018) made
72 these observations using Direct Numerical Simulations (DNS) of statistically stationary
73 periodic turbulence at low to moderate Taylor length-based Reynolds numbers from about
74 80 to 170. Even though their Reynolds numbers were not high enough to test the high
75 Reynolds number scaling consequences of Kolmogorov's theory, they observed an energy
76 spectrum with a near-decade power law range where the power law exponent was not too
77 far from Kolmogorov's $-5/3$. However, they did not observe a significant range of scales
78 where the scale-by-scale equilibrium reduces to a scale-by-scale balance between average

79 interscale turbulence energy transfer rate and average turbulence dissipation as predicted by
80 the Kolmogorov theory for statistically stationary homogeneous turbulence at asymptotically
81 high Reynolds numbers. This high Reynolds number scale-by-scale equilibrium is the
82 hallmark of the Kolmogorov average cascade and is typically not put in question by existing
83 intermittency corrections to Kolmogorov’s theory (e.g. see Frisch (1995)).

84 Given the low to moderate Reynolds numbers of the DNS used by Yasuda & Vassilicos
85 (2018), their observations concern interscale turbulence energy transfers more than the
86 turbulence cascade per se if the concept of turbulence cascade is taken to have meaning
87 only at very large Reynolds numbers. They demonstrated that an interscale transfer picture
88 appears that is radically different from Kolmogorov’s if the average is lifted and all spatio-
89 temporal intermittent fluctuations are taken into account. This different picture involves highly
90 fluctuating processes which vanish on average in statistically stationary and homogeneous
91 turbulence and are not taken into account by the Kolmogorov theory for that very reason. We
92 stress once more that Yasuda & Vassilicos (2018) made this demonstration in statistically
93 homogeneous and stationary turbulence, the very type of turbulence where Kolmogorov’s
94 theory has been designed for.

95 It is hard to imagine that the complex turbulence energy transfer picture deduced by the DNS
96 of Yasuda & Vassilicos (2018) does not survive at asymptotically high Reynolds numbers
97 because it is known that the small-scale turbulence becomes increasingly intermittent with
98 increasing Reynolds number (e.g. see Frisch (1995); Sreenivasan & Antonia (1997)). A DNS
99 study at higher Reynolds numbers is nevertheless needed to ascertain this point. However,
100 this is not the study proposed in this paper. In this paper our aim is to gain deeper insight into
101 the fluctuating energy transfer picture revealed by the DNS of Yasuda & Vassilicos (2018)
102 and we do this in terms of Helmholtz decomposed solenoidal and irrotational acceleration
103 fields. Given that the computational cost involved in this Helmholtz decomposition is high
104 (see following two sections) it is not possible for us to carry out our study for a variety of
105 increasing Reynolds numbers and thereby combine it with a Reynolds number dependence
106 study. We therefore limit ourselves to Reynolds numbers comparable to those of Yasuda &
107 Vassilicos (2018).

108 The radically different turbulence energy transfer picture which appears when all intermit-
109 tent turbulence fluctuations are taken into account exhibits correlations between fluctuations
110 of different processes: in particular, the fluctuating pressure-velocity term mentioned above
111 is correlated with the interscale energy transfer rate, and the time derivative of the turbulent
112 kinetic energy below a certain two-point length r is correlated with the inter-space energy
113 transport rate at the same length r . Yasuda & Vassilicos (2018) explained the former
114 correlation as resulting from the link between non-linearity and non-locality (via the
115 pressure field) and the latter correlation as reflecting the passive sweeping of small turbulent
116 eddies by large ones (Tennekes 1975). However, this sweeping (also termed “random Taylor
117 hypothesis”) has been studied by reference to the one-point incompressible Navier-Stokes
118 equation (e.g. Tennekes (1975), Tsinober *et al.* (2001)) rather than the two-point Kármán-
119 Howarth-Monin-Hill (KMH) equation, used by Yasuda & Vassilicos (2018) in their study
120 of the fluctuating turbulence cascade. The KMH equation is a scale-by-scale energy budget
121 local in space and time, directly derived from the incompressible Navier-Stokes equations
122 for the instantaneous velocity field (see Hill (2002)) without decomposition (e.g. Reynolds
123 decomposition), without averages (e.g. Reynolds averages), and without any assumption made
124 about the turbulent flow (e.g. homogeneity, isotropy, etc.). The initial motivation of the present
125 paper is to substantiate the claim of Yasuda & Vassilicos (2018) concerning correlations being
126 caused by random sweeping by translating the sweeping analysis of Tsinober *et al.* (2001)
127 to the KMH equation. It is in doing so that we use the Helmholtz decomposition which
128 Tsinober *et al.* (2001) introduced for the analysis of the acceleration field. We apply it to

129 the two-point Navier-Stokes difference (NSD) equation (which is the equation governing
 130 the dynamics of two-point velocity differences) and the KMHM equation which derives
 131 from it. This decomposition into solenoidal and irrotational terms breaks the Navier-Stokes
 132 equation into two equations, one being the irrotational balance between non-linearity and
 133 non-locality (pressure) and the other being the solenoidal balance between local unsteadiness
 134 and advection which encapsulates the sweeping. With this decomposition we substantiate all
 135 the correlations observed by Yasuda & Vassilicos (2018) between different KMHM terms
 136 representing different energy change processes, not only the ones caused by sweeping. In fact,
 137 we reduce the relation between interspace turbulence energy transfer/transport and two-point
 138 sweeping (i.e. the random Taylor hypothesis that we generalise to two-point statistics), and we
 139 extend the correlation study to solenoidal and irrotational sub-terms of the KMHM equation
 140 which leads to even stronger correlations than those found by Yasuda & Vassilicos (2018).
 141 This approach sheds some light on the way that two-point sweeping and interscale energy
 142 transfer relate to each other. We then ask whether the scale-by-scale equilibrium which is
 143 at the basis of Kolmogorov's theory and which disappears when the average is lifted does
 144 nevertheless exist locally at relatively high energy transfer events, a question which leads
 145 us to consider whether two-point sweeping also holds at such events. Finally, we study the
 146 recently introduced decomposition (Alves Portela *et al.* 2020) of the interscale transfer rate
 147 into a homogeneous and an inhomogeneous interscale transfer component. We analyse their
 148 fluctuations and the correlations of these fluctuations, both unconditionally and conditionally
 149 on relatively rare intense interscale transfer events.

150 In the following section we introduce our direct numerical simulations (DNSs) of forced
 151 periodic turbulence. Subsection 3.1 is a reminder of the application of this decomposition
 152 to the one-point Navier-Stokes equation by Tsinober *et al.* (2001). In this sub-section
 153 we also validate our DNS by retrieving the conclusions of Tsinober *et al.* (2001) on
 154 sweeping and by comparing our DNS results on one-point acceleration dynamics to theirs. In
 155 subsections 3.2-3.3 we apply the Helmholtz decomposition to the two-point NSD equation
 156 for the case of homogeneous/periodic turbulence and in subsection 3.4 we derive from the
 157 Helmholtz decomposed Navier-Stokes difference equations corresponding KMHM equations.
 158 Subsection 3.4 formalises the connection between the NS and KMHM dynamics, clarifies
 159 under which conditions a link exists between NS and KMHM dynamics and provides results
 160 on scale and Reynolds number dependencies of the KMHM dynamics. By considering the
 161 NSD dynamics in terms of solenoidal and irrotational dynamics, we derive two new KMHM
 162 equations. In section 4 we use these two new KMHM equations to obtain new results on
 163 the fluctuating cascade dynamics across scales both unconditionally and conditionally on
 164 rare extreme interscale energy transfer events. In section 5 we analyse the inhomogeneous
 165 and homogeneous contributions to the interscale energy transfer rate. Finally, section 6
 166 summarises our results.

167 2. DNS of body-forced period turbulence

168 Our study requires turbulence data from a turbulent flow where the Kolmogorov equilibrium
 169 theory for statistically homogeneous and stationary turbulence is applicable. We therefore
 170 follow Yasuda & Vassilicos (2018) and perform Direct Numerical Simulations of body-forced
 171 periodic Navier-Stokes turbulence with the same pseudo-spectral code that they used. This
 172 code solves numerically the vorticity equation

$$173 \quad \frac{\partial \boldsymbol{\omega}}{\partial t} = \nabla_{\mathbf{x}} \times (\mathbf{u} \times \boldsymbol{\omega}) + \nu \nabla_{\mathbf{x}}^2 \boldsymbol{\omega} + \nabla_{\mathbf{x}} \times \mathbf{f}, \quad (2.1)$$

N	$\langle Re_\lambda \rangle_t$	$\nu/10^3$	$k_{\max} \langle \eta \rangle_t$	$2\pi/\langle L \rangle_t$	$\langle \lambda \rangle / \langle L \rangle_t$	T_s/T	$\Delta T/T$
256	112	1.80	1.88	5.6	3.5	21	0.01
512	174	0.72	1.89	5.4	5.2	27	0.12

Table 1: Specifications of the numerical simulations. N denotes the number of grid points in each Cartesian coordinate, Re_λ the Taylor-scale Reynolds number, ν the kinematic viscosity, $k_{\max} = \sqrt{2}/3N$ is the highest resolved wavenumber, η and λ are, respectively, the Kolmogorov and Taylor lengths and $\langle \dots \rangle_t$ denotes a time-average. L is the integral lengths calculated from the three-dimensional energy spectrum $E(k, t)$:

$L(t) = (3\pi/4) \int_0^\infty k^{-1} E(k, t) dk / K(t)$ where $K(t)$ is the kinetic energy per unit mass. T_s denotes the total sampling time over which converged statistics are calculated by sampling randomly in space-time, ΔT denotes the time between samples and $T \equiv \langle L \rangle_t / \sqrt{2/3 \langle K \rangle_t}$ is the turnover time.

174 subjected to the continuity equation

$$175 \quad \nabla_{\mathbf{x}} \cdot \mathbf{u} = 0, \quad (2.2)$$

176 where $\mathbf{u}(\mathbf{x}, t)$, $\mathbf{f}(\mathbf{x}, t)$ and $\boldsymbol{\omega}(\mathbf{x}, t)$ are the velocity, force and vorticity fields respectively and
 177 ν is the kinematic viscosity. All fields are 2π -periodic in each one of the three orthogonal
 178 spatial coordinates x_1, x_2 and x_3 , and $\mathbf{x} = (x_1, x_2, x_3)$. The pseudo-spectral method is fully
 179 dealised with a combination of phase-shifting and spherical truncation (Patterson & Orszag
 180 1971). The forcing method is a negative damping forcing (Linkmann & Morozov 2015;
 181 McComb *et al.* 2015b)

$$182 \quad \widehat{\mathbf{f}}(\mathbf{k}, t) = (\epsilon_W / 2K_f) \widehat{\mathbf{u}}(\mathbf{k}, t) \quad \text{for } 0 < |\mathbf{k}| < k_f, \quad (2.3)$$

$$183 \quad = 0 \quad \text{otherwise,} \quad (2.4)$$

185 where $\widehat{\mathbf{f}}(\mathbf{k}, t)$ and $\widehat{\mathbf{u}}(\mathbf{k}, t)$ are the Fourier transforms of $\mathbf{f}(\mathbf{x}, t)$ and $\mathbf{u}(\mathbf{x}, t)$ respectively, k_f is
 186 the cutoff wavenumber, ϵ_W is the energy input rate per unit mass and K_f is the kinetic energy
 187 per unit mass in the wavenumber band $0 < |\mathbf{k}| < k_f$. Note that this forcing is incompressible
 188 and has therefore no irrotational part. The addition of a potential, i.e. irrotational, term to
 189 the forcing would effectively just be subsumed into the pressure required to keep the flow
 190 incompressible.

191 We perform two DNS of forced periodic/homogeneous turbulence with forcing parameters
 192 $\epsilon_W = 0.1$ and $k_f = 2.5$ at both simulation sizes 256^3 grid points and 512^3 grid points. Average
 193 statistics are given in table 1. For these two simulation sizes respectively, deviations around
 194 these averages are as follows: the standard deviations of L are $0.007L_b$ and $0.006L_b$ (where
 195 $L_b = 2\pi$) and the maximum L values are $0.188L_b$ and $0.202L_b$; the standard deviations of
 196 λ are 2.5% and 3.7% of $\langle \lambda \rangle_t$; and the standard deviation of $k_{\max} \eta$ are 0.025 and 0.035.

197 McComb *et al.* (2015a) performed DNS with the same combinations of N , ν and forcing
 198 as in our simulations. The time-averaged Taylor-scale Reynolds numbers $\langle Re_\lambda \rangle_t$, the ratios of
 199 the box size to the time-averaged integral length $2\pi/\langle L \rangle_t$ and the time-averaged Kolmogorov
 200 microscales $\langle \eta \rangle_t$ are all very similar (and $\langle \dots \rangle_t$ denotes a time-average). This study reports
 201 slightly poorer small-scale resolution $k_{\max} \langle \eta \rangle_t$ than ours due to their more severe spherical
 202 truncation for dealiasing.

203 We have also verified that the results do not significantly change when the flow is forced
 204 at small wavenumbers with an ABC forcing with $A = B = C$ (Podvigina & Pouquet 1994).
 205 In contrast to the negative damping forcing, this forcing is independent of time and of the
 206 velocity field and is also maximally helical as $\nabla_{\mathbf{x}} \times \mathbf{f}$ is parallel to \mathbf{f} (Galanti & Tsinober

207 2000). The helicity input of the ABC forcing has been studied in the context of the energy
208 cascade in terms of its effect on the dissipation coefficient in Linkmann (2018).

209 Our Reynolds numbers are relatively limited due to the high computational expense of our
210 NSD and KMHM post-processing (which is typically at least one order of magnitude more
211 expensive than the DNS). We detail the computational expense of the post-processing once
212 the relevant terms have been introduced in section 3.3.

213 In the following section we show how we apply the Helmholtz decomposition to the KMHM
214 equation. We start in subsection 3.1 by applying this decomposition to the one-point Navier-
215 Stokes equation following Tsinober *et al.* (2001). In this sub-section we also validate our
216 DNS by retrieving the conclusions of Tsinober *et al.* (2001), in particular on sweeping, and
217 by comparing our DNS results on one-point acceleration dynamics to theirs. In subsections
218 3.2 and 3.3 we apply the Helmholtz decomposition to the two-point Navier-Stokes difference
219 equation for the case of homogeneous/periodic turbulence and in subsection 3.4 we derive
220 from the Helmholtz-decomposed Navier-Stokes difference equations corresponding KMHM
221 equations.

222 3. Helmholtz decomposition of two-point Navier-Stokes dynamics and 223 corresponding turbulent energy exchanges

224 3.1. Solenoidal and irrotational acceleration fluctuations

225 The Helmholtz decomposition states that a twice continuously differentiable 3D vector field
226 $\mathbf{q}(\mathbf{x}, t)$ defined on a domain $V \subseteq \mathbb{R}^3$ can be expressed as the sum of an irrotational vector
227 field $\mathbf{q}_I(\mathbf{x}, t)$ and a solenoidal vector field $\mathbf{q}_S(\mathbf{x}, t)$ (Helmholtz 1867; Stewart 2012; Bhatia
228 *et al.* 2013)

$$229 \quad \mathbf{q}_I(\mathbf{x}, t) = -\nabla_{\mathbf{x}}\phi(\mathbf{x}, t), \quad \mathbf{q}_S(\mathbf{x}, t) = \nabla_{\mathbf{x}} \times \mathbf{B}(\mathbf{x}, t), \quad (3.1)$$

230 where $\phi(\mathbf{x}, t)$ is a scalar potential and $\mathbf{B}(\mathbf{x}, t)$ is a vector potential. The Helmholtz decom-
231 position and its interpretation can be applied to any vector field $\mathbf{q}(\mathbf{x}, t)$ satisfying the above
232 conditions, and Tsinober *et al.* (2001) applied it to fluid accelerations and the incompressible
233 Navier-Stokes equation.

234 The solenoidal and irrotational Navier-Stokes equations in homogeneous/periodic turbu-
235 lence can be derived from the incompressible Navier-Stokes equation in Fourier space (see
236 appendix A). After transformation back to physical space, one obtains

$$237 \quad \frac{\partial \mathbf{u}}{\partial t} + (\mathbf{u} \cdot \nabla_{\mathbf{x}} \mathbf{u})^T = \nu \nabla_{\mathbf{x}}^2 \mathbf{u} + \mathbf{f}^T, \quad (3.2)$$

$$238 \quad (\mathbf{u} \cdot \nabla_{\mathbf{x}} \mathbf{u})^L = -\frac{1}{\rho} \nabla_{\mathbf{x}} p + \mathbf{f}^L, \quad (3.3)$$

240 where superscripts L and T denote fields obtained from longitudinal and transverse parts
241 of respective Fourier vector fields (see appendix A for precise definitions and (Pope 2000;
242 Stewart 2012)), $p = p(\mathbf{x}, t)$ is the pressure field and ρ is the density. For any periodic vector
243 field \mathbf{q} , \mathbf{q}^L equals the irrotational field \mathbf{q}_I and \mathbf{q}^T equals the solenoidal field \mathbf{q}_S (see appendix
244 A and Stewart (2012)). From equations (3.2)-(3.3), one arrives at (Tsinober *et al.* 2001)

$$245 \quad \frac{\partial \mathbf{u}}{\partial t} + (\mathbf{u} \cdot \nabla_{\mathbf{x}} \mathbf{u})_S = \nu \nabla_{\mathbf{x}}^2 \mathbf{u} + \mathbf{f}_S, \quad (3.4)$$

$$246 \quad (\mathbf{u} \cdot \nabla_{\mathbf{x}} \mathbf{u})_I = -\frac{1}{\rho} \nabla_{\mathbf{x}} p + \mathbf{f}_I, \quad (3.5)$$

247
248 which we refer to as Tsinober equations. (3.4) contains only solenoidal vector fields and (3.5)
249 contains only irrotational vector fields. Note that in the case of an incompressible periodic

	\mathbf{a}_c	\mathbf{a}_l	\mathbf{a}_{c_S}	\mathbf{a}_{c_I}	\mathbf{a}_p	\mathbf{a}	\mathbf{a}_v	\mathbf{f}	$\langle Re_\lambda \rangle_t$
$\langle \mathbf{q}^2 \rangle / (3\langle \epsilon \rangle^{3/2} \nu^{-1/2})$	8.47	5.87	5.93	2.55	2.55	2.60	0.05	0.007	112
$\langle \mathbf{q}^2 \rangle / (3\langle \epsilon \rangle^{3/2} \nu^{-1/2})$	14.28	11.21	11.26	3.03	3.03	3.09	0.05	0.005	174
$\langle \mathbf{q}^2 \rangle / \langle \mathbf{a}_c^2 \rangle$	1	0.69	0.70	0.30	0.30	0.31	0.0062	0.00081	112
$\langle \mathbf{q}^2 \rangle / \langle \mathbf{a}_c^2 \rangle$	1	0.78	0.79	0.21	0.21	0.22	0.0038	0.00032	174

Table 2: Normalised average magnitudes $\langle \mathbf{q}^2 \rangle / (3\langle \epsilon \rangle^{3/2} \nu^{-1/2})$ and $\langle \mathbf{q}^2 \rangle / \langle \mathbf{a}_c^2 \rangle$ for Navier-Stokes accelerations and forces \mathbf{q} defined in the fourth paragraph of 3.1 for our two $\langle Re_\lambda \rangle_t$. The accelerations and forces \mathbf{q} are listed on the top row, $\mathbf{q}^2 \equiv q_i q_i$, ϵ denotes the viscous dissipation rate and $\langle \dots \rangle$ denotes a spatio-temporal average.

250 velocity field, the velocity field is solenoidal, i.e. $\mathbf{u} = \mathbf{u}_S$. This follows immediately from the
 251 scalar potential ϕ being the solution to $\nabla_x^2 \phi = 0$ with periodic boundary conditions for $\nabla_x \phi$,
 252 yielding $\phi = const$.

253 In appendix C we show that (3.4) is the integrated vorticity equation and that (3.5) is
 254 the integrated Poisson equation for pressure. The procedure presented in appendix C for
 255 obtaining the Tsinober equations is also used in this same appendix to obtain generalised
 256 Tsinober equations for non-homogeneous/non-periodic turbulence with arbitrary boundary
 257 conditions.

258 Following the notation of Tsinober *et al.* (2001), we define $\mathbf{a}_l \equiv \partial \mathbf{u} / \partial t$, $\mathbf{a}_c \equiv \mathbf{u} \cdot$
 259 $\nabla_x \mathbf{u}$, $\mathbf{a} \equiv \mathbf{a}_l + \mathbf{a}_c$, $\mathbf{a}_p \equiv -1/\rho \nabla_x p$ and $\mathbf{a}_v \equiv \nu \nabla_x^2 \mathbf{u}$. In such notation, equations (3.4)-
 260 (3.5) are $\mathbf{a}_l + \mathbf{a}_{c_S} = \mathbf{a}_v + \mathbf{f}_S$ and $\mathbf{a}_{c_I} = \mathbf{a}_p + \mathbf{f}_I$. Tsinober *et al.* (2001) in fact wrote
 261 these equations for statistically homogeneous/periodic Navier-Stokes turbulence without
 262 body forces, i.e. with $\mathbf{f} = 0$. In general, however, the body forcing can be considered, as
 263 in the present work, to be non-zero and typically incompressible, i.e. $\mathbf{f}_I = \mathbf{0}$ but $\mathbf{f}_S \neq \mathbf{0}$,
 264 given that a compressible component of the forcing can be subsumed into the pressure field
 265 in incompressible turbulence. In body-forced statistically stationary homogeneous/periodic
 266 turbulence, the average forcing magnitude $\langle \mathbf{f}^2 \rangle$, where the brackets denote spatio-temporal
 267 averaging, tends to be small compared to $\langle \mathbf{a}_v^2 \rangle$ when the forcing is applied only to the largest
 268 scales (Vedula & Yeung 1999). Given that $\langle \mathbf{f} \cdot \mathbf{u} \rangle = \langle \epsilon \rangle$, where ϵ is the local turbulence
 269 dissipation rate, \mathbf{f}^2 can be quite small if \mathbf{f} is not close to orthogonal to the velocity field. This
 270 is indeed the case with the negative damping and ABC forcings used in this study. In cases
 271 where \mathbf{f} is close to orthogonal to the velocity field, which is conceivable in electromagnetic
 272 situations (Lorentz force), \mathbf{f}^2 needs to be large enough for $\langle \mathbf{f} \cdot \mathbf{u} \rangle$ to balance $\langle \epsilon \rangle$. In this
 273 study we have not considered such forcings and some of our results might not be applicable
 274 to such situations. Our results for the forcings we used indicate that $\langle \mathbf{f}^2 \rangle$ is indeed much
 275 smaller than $\langle \mathbf{a}_v^2 \rangle$ (see results from our DNS in table 2) and the probability to find values of
 276 \mathbf{f}^2 large enough to be comparable to the other terms in the Tsinober equations is extremely
 277 small (see results from our DNS in figure 1 and table 3 where we see, in particular, that
 278 $|\mathbf{f}| > 0.1|\mathbf{a}_{c_S}|$ in 15.3% and 6.3% of the spatio-temporal domain for the two Reynolds
 279 numbers respectively, the percentage being smaller for the higher Reynolds number. If we
 280 consider $|\mathbf{f}| > \sqrt{0.1}|\mathbf{a}_{c_S}| \approx 0.32|\mathbf{a}_{c_S}|$, we see that this is only satisfied in 0.8% and 0.3%
 281 of the spatio-temporal domain respectively. Furthermore, figure 1 and table 3 show that \mathbf{f}
 282 is also typically much smaller than \mathbf{a}_v . We can therefore write $\mathbf{a}_l + \mathbf{a}_{c_S} \approx \mathbf{a}_v$, this being a
 283 good approximation in the majority of the flow for the majority of the time. With $\mathbf{a}_{c_I} = \mathbf{a}_p$
 284 given that $\mathbf{f}_I = \mathbf{0}$, these two equations are very close to the way that Tsinober *et al.* (2001)

α	0.001	0.01	0.1	1
$\text{Prob}(\mathbf{a}_v^2 > \alpha \mathbf{a}_{c_S}^2)$	(0.893, 0.808)	(0.441, 0.308)	(0.068, 0.037)	(0.004, 0.002)
$\text{Prob}(\mathbf{f}^2 > \alpha \mathbf{a}_{c_S}^2)$	(0.707, 0.476)	(0.155, 0.063)	(0.008, 0.003)	$(3 * 10^{-4}, 9 * 10^{-5})$

Table 3: Probabilities of events $\mathbf{q}^2 > \alpha \mathbf{p}^2$ for NS terms (\mathbf{q}, \mathbf{p}) with α specified on the top row. The two probability values in the brackets for each $(\mathbf{q}, \mathbf{p}, \alpha)$ combination refer to $\langle Re_\lambda \rangle_t = 112$ and $\langle Re_\lambda \rangle_t = 174$ respectively.

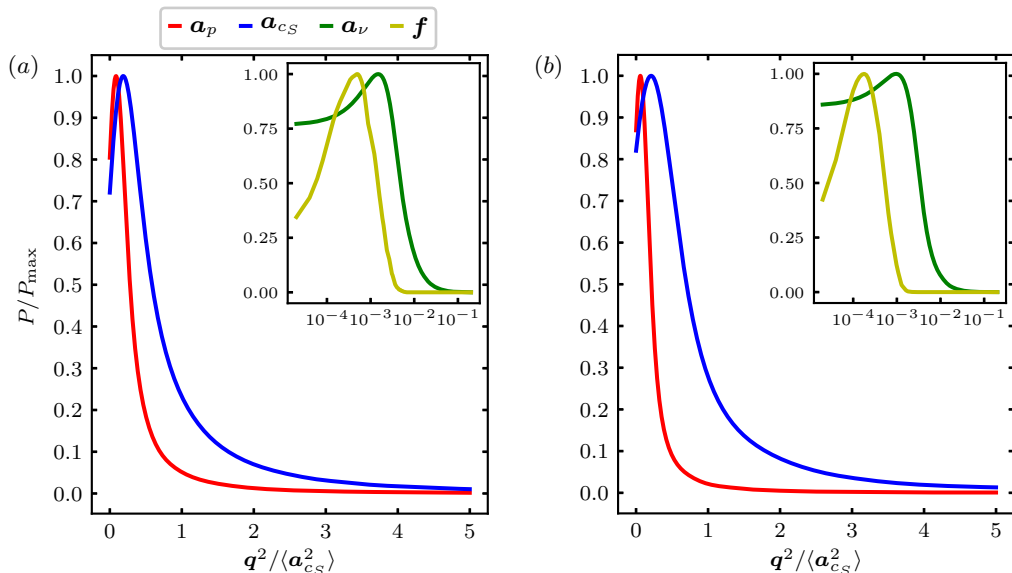


Figure 1: Probability density functions (PDFs) P of Navier-Stokes acceleration and force magnitudes \mathbf{q}^2 for terms \mathbf{q} listed at the top of (a). P_{\max} for the PDF of \mathbf{q}^2 denotes its maximum value. (a) $\langle Re_\lambda \rangle_t = 112$, (b) $\langle Re_\lambda \rangle_t = 174$.

285 originally wrote them ($\mathbf{a}_l + \mathbf{a}_{c_S} = \mathbf{a}_v$ and $\mathbf{a}_{c_I} = \mathbf{a}_p$ for the $\mathbf{f} \equiv 0$ case) and we can therefore
 286 expect our DNS to retrieve the DNS results and conclusions of Tsinober *et al.* (2001).

287 The DNS of Tsinober *et al.* (2001) showed that \mathbf{a}_v is typically negligible (i.e. in a statistical
 288 sense, not everywhere at any time in the flow) compared to all the other acceleration terms in
 289 the Tsinober equations, namely \mathbf{a}_l , \mathbf{a}_{c_S} , \mathbf{a}_{c_I} and \mathbf{a}_p . This is confirmed by our DNS results in
 290 tables 2-3 and in figure 1 which are for similar Reynolds numbers to those of Tsinober *et al.*
 291 (2001) and where we report rms values, and probabilities of various acceleration terms. It is
 292 worth noting that \mathbf{a}_v is not everywhere always negligible, at these Reynolds numbers at least.
 293 For example, $|\mathbf{a}_v| > 0.1|\mathbf{a}_{c_S}|$ in 44.1% and 30.8% of the space-time domain for our lower and
 294 higher Reynolds number respectively; and if we consider $|\mathbf{a}_v| > 0.32|\mathbf{a}_{c_S}|$, this is satisfied
 295 in 6.8% and 3.7% of cases. Note that the DNS results of Tsinober *et al.* (2001) suggest
 296 that the viscous force *typically* decreases in magnitude compared to \mathbf{a}_{c_S} as the Reynolds
 297 number increases and our results for our two Reynolds numbers agree with this trend. One
 298 may therefore expect the the first of the two Tsinober equations for homogeneous/periodic
 299 turbulence with the kind of forcing we consider here to *typically* reduce to

$$300 \quad \mathbf{a}_l + \mathbf{a}_{c_S} \approx 0, \quad (3.6)$$

$\langle Re_\lambda \rangle_t$	$\langle \cos(\mathbf{a}_{c_I}, \mathbf{a}_p) \rangle$	$\langle \cos(\mathbf{a}, \mathbf{a}_p) \rangle$	$\langle \cos(\mathbf{a}_I, \mathbf{a}_{c_S}) \rangle$	$\langle \cos(\mathbf{a}_I, \mathbf{a}_c) \rangle$	$\langle \cos(\mathbf{a}_c, \mathbf{a}_p) \rangle$
112	0.9999	0.972	-0.985	-0.726	0.388
174	0.9999	0.975	-0.990	-0.796	0.308

Table 4: NS average alignments $\langle \cos(\mathbf{q}, \mathbf{p}) \rangle$ for NS acceleration pairs (\mathbf{q}, \mathbf{p}) .

301 at high enough Reynold numbers, the approximation being valid in the sense that the neglected
302 terms are significantly smaller than the retained ones in the majority of the flow for the
303 majority of the time. There exist, however, some relatively rare spacio-temporal events
304 where the neglected viscous force and/or body force are significant (for example, as stated
305 a few lines above, $|\mathbf{a}_v|$ is larger than $0.32|\mathbf{a}_{c_S}|$ in 6.8% and 3.7% of all spacio-temporal
306 events for our lower and higher Reynolds numbers respectively) and where the right hand
307 side of (3.6) is therefore not zero. In fact, many of these relatively rare events can be expected
308 to account for some or even much of the average turbulence dissipation which is a sum of
309 squares of fluctuating velocity gradients. More generally, one cannot use equation (3.6) to
310 derive statistics of fluctuating velocity gradients, as in Tang *et al.* (2022) for example.

311 The second of the two Tsinober equations, namely

$$312 \quad \mathbf{a}_{c_I} = \mathbf{a}_p, \quad (3.7)$$

313 is exact everywhere and at any time and we keep it as it is.

314 Equations (3.6)-(3.7) suggest similar magnitudes and strong alignment between \mathbf{a}_I and
315 $-\mathbf{a}_{c_S}$ and equal magnitudes as well as perfect alignment between \mathbf{a}_{c_I} and \mathbf{a}_p . Such
316 magnitudes and alignments were observed in the DNS of Tsinober *et al.* (2001) and are also
317 strongly confirmed by our own DNS in table 4 (\mathbf{a}_{c_S} and \mathbf{a}_{c_I} are calculated on the basis of
318 equation (A 1) in appendix A and aliasing errors associated with non-linear terms are removed
319 by phase-shifting and truncation (Patterson & Orszag 1971)). As suggested by previous DNS
320 and experimental results (e.g. Tsinober *et al.* (2001); Chevillard *et al.* (2005); Yeung *et al.*
321 (2006)), and as also supported by our own DNS results in tables 2 and 4, $\mathbf{a} \approx \mathbf{a}_p$ and
322 $\langle \mathbf{a}_I^2 \rangle / \langle \mathbf{a}^2 \rangle \sim \langle Re_\lambda \rangle_t^{1/2}$. In fact, the scaling $\langle \mathbf{a}_I^2 \rangle / \langle \mathbf{a}^2 \rangle \sim \langle Re_\lambda \rangle_t^{1/2}$ follows from the analysis of
323 Tennekes (1975) who expressed the concept of passive sweeping by pointing out that "at high
324 Reynolds number the dissipative eddies flow past an Eulerian observer in a time much shorter
325 than the time scale which characterizes their own dynamics". It then follows from equations
326 (3.6)-(3.7), from $\langle \mathbf{a}_I^2 \rangle / \langle \mathbf{a}^2 \rangle \sim \langle Re_\lambda \rangle_t^{1/2}$ and from $\langle \mathbf{a}_p^2 \rangle \approx \langle \mathbf{a}^2 \rangle$ that $\langle \mathbf{a}_{c_S}^2 \rangle / \langle \mathbf{a}_{c_I}^2 \rangle \sim \langle Re_\lambda \rangle_t^{1/2}$
327 with increasing $\langle Re_\lambda \rangle_t$, i.e., \mathbf{a}_c becomes increasingly solenoidal with increasing $\langle Re_\lambda \rangle_t$. In
328 this way, the anti-alignment in (3.6) leads to an increasing anti-alignment tendency between
329 \mathbf{a}_I and \mathbf{a}_c with increasing Reynolds number, which is consistent with the notion of passive
330 sweeping of small eddies by large ones, i.e. the random Taylor hypothesis of Tennekes (1975).
331 These observations and conclusions were all made by Tsinober *et al.* (2001). They are now
332 confirmed by our DNS results in table 2 and this reiterates that they do not require a large
333 Taylor length-based Reynolds number to emerge.

334 As a final point, it is a general property of isotropic random vector fields \mathbf{q} that $\langle \mathbf{q}_I(\mathbf{x}, t) \cdot$
335 $\mathbf{q}_S(\mathbf{x} + \mathbf{r}, t) \rangle_x = 0$ for any \mathbf{r} (including $\mathbf{r} = 0$), where $\langle \dots \rangle_x$ signifies a spatial average (Monin
336 *et al.* 1975). Thus, $\langle \mathbf{a}_c^2 \rangle = \langle \mathbf{a}_{c_I}^2 \rangle + \langle \mathbf{a}_{c_S}^2 \rangle$ if the small-scale turbulence is isotropic. Both our
337 DNS and the DNS of Tsinober *et al.* (2001) confirm this equality. From this equality and
338 from (3.6), $\langle \mathbf{a}_{c_S}^2 \rangle / \langle \mathbf{a}_{c_I}^2 \rangle \sim \langle Re_\lambda \rangle_t^{1/2}$, (3.7), $\mathbf{a} \approx \mathbf{a}_p$ and $\langle \mathbf{a}^2 \rangle \gg \langle \mathbf{a}_v^2 \rangle \gg \langle \mathbf{f}^2 \rangle$, we have all in
339 all

$$340 \quad \langle \mathbf{a}_c^2 \rangle \gg \langle \mathbf{a}_{c_S}^2 \rangle \approx \langle \mathbf{a}_I^2 \rangle \gg \langle \mathbf{a}_{c_I}^2 \rangle = \langle \mathbf{a}_p^2 \rangle \approx \langle \mathbf{a}^2 \rangle \gg \langle \mathbf{a}_v^2 \rangle \gg \langle \mathbf{f}^2 \rangle, \quad (3.8)$$

341 for large enough $\langle Re_\lambda \rangle_t$. The average magnitude ordering in (3.8) is confirmed in our DNS
 342 (see table 2) and the DNS of Tsinober *et al.* (2001) even though the Reynolds numbers of these
 343 DNS are moderate and so the difference between $\langle a_{c_I}^2 \rangle$ and $\langle a_I^2 \rangle$ is not so large. Tsinober's
 344 way to formulate sweeping is encapsulated in $\langle a_{c_S}^2 \rangle \approx \langle a_I^2 \rangle \gg \langle a_{c_I}^2 \rangle = \langle a_p^2 \rangle \approx \langle a^2 \rangle$ and in
 345 the alignments implied by equations (3.6)-(3.7) which are also statistically confirmed by our
 346 DNS in table 4.

347 3.2. From one-point to two-point Navier-Stokes dynamics in periodic/homogeneous 348 turbulence

349 The Navier-Stokes difference (NSD) equation at centroid \mathbf{x} and separation vector \mathbf{r} is derived
 350 by subtracting the Navier-Stokes (NS) equation at location $\mathbf{x}^+ = \mathbf{x} + \mathbf{r}/2$ from the NS equation
 351 at location $\mathbf{x}^- = \mathbf{x} - \mathbf{r}/2$. Defining $\delta \mathbf{q}(\mathbf{x}, \mathbf{r}, t) \equiv \mathbf{q}(\mathbf{x} + \mathbf{r}/2, t) - \mathbf{q}(\mathbf{x} - \mathbf{r}/2, t)$ for any NS
 352 term $\mathbf{q}(\mathbf{x}, t)$, the NSD equation (Hill 2002) reads

$$353 \quad \frac{\partial \delta \mathbf{u}}{\partial t} + \delta \mathbf{a}_c = -\frac{1}{\rho} \nabla_x \delta p + \delta \mathbf{a}_v + \delta \mathbf{f}, \quad (3.9)$$

354 The NSD equation governs the evolution of $\delta \mathbf{u}$, which can be thought of as pertaining to the
 355 momentum at scales smaller or comparable to $|\mathbf{r}|$. We derive the solenoidal NSD equation by
 356 subtracting equation (3.4) at $\mathbf{x} - \mathbf{r}/2$ from the same equation at $\mathbf{x} + \mathbf{r}/2$. The same operation
 357 is used to derive the irrotational NSD equation. The resulting equations read

$$358 \quad \frac{\partial \delta \mathbf{u}}{\partial t} + \delta \mathbf{a}_{c_S} = \delta \mathbf{a}_v + \delta \mathbf{f}_S, \quad (3.10)$$

$$359 \quad \delta \mathbf{a}_{c_I} = -\frac{1}{\rho} \nabla_x \delta p + \delta \mathbf{f}_I, \quad (3.11)$$

361 where $\delta \mathbf{a}_{c_S}(\mathbf{x}, \mathbf{r}, t) \equiv \mathbf{a}_{c_S}(\mathbf{x} + \mathbf{r}/2, t) - \mathbf{a}_{c_S}(\mathbf{x} - \mathbf{r}/2, t)$ and $\delta \mathbf{a}_{c_I}(\mathbf{x}, \mathbf{r}, t) \equiv \mathbf{a}_{c_I}(\mathbf{x} + \mathbf{r}/2, t) -$
 362 $\mathbf{a}_{c_I}(\mathbf{x} - \mathbf{r}/2, t)$ and note that these terms refer to solenoidal and irrotational terms in \mathbf{x} -space
 363 rather than \mathbf{r} -space. The forcings we consider have no irrotational part and so $\delta \mathbf{f}_I = 0$.
 364 At the moderate $\langle Re_\lambda \rangle_t$ of our DNS, the approximate equation (3.6) is valid in the sense
 365 explained in the text which accompanies it in the previous sub-section, i.e. for a majority
 366 of spacio-temporal events. If the magnitude of the separation vector \mathbf{r} is not too small for
 367 viscosity to matter directly nor too large for the forcing to be directly present, we may safely
 368 subtract equation (3.6) at $\mathbf{x} - \mathbf{r}/2$ from equation (3.6) at $\mathbf{x} + \mathbf{r}/2$ to obtain an approximation
 369 to (3.10) for sufficiently high Reynolds number: this is the first of the two equations below
 370 where $\delta \mathbf{a}_I \equiv \partial \delta \mathbf{u} / \partial t$:

$$371 \quad \delta \mathbf{a}_I + \delta \mathbf{a}_{c_S} \approx 0, \quad (3.12)$$

$$372 \quad \delta \mathbf{a}_{c_I} = -\frac{1}{\rho} \nabla_x \delta p. \quad (3.13)$$

374 The second equation, equation (3.13), follows directly from (3.11) with $\delta \mathbf{f}_I = 0$ without any
 375 restriction on either \mathbf{r} or Reynolds number and is exact.

376 Like equation (3.6), (3.12) can be expected to be valid broadly except where and when
 377 $\delta \mathbf{a}_v + \delta \mathbf{f}_S$ is large enough not to be negligible. Figure 2 shows statistically converged
 378 estimations of exceedance probabilities of NSD viscous and external force terms which
 379 suggest that (3.12) is indeed a good approximation for most of space and time at the Reynolds
 380 numbers of our two DNS, at the very least for separation distances larger than $\langle \lambda \rangle_t$ and
 381 smaller than $\langle L \rangle_t$. With regards to the forcing, $\text{Prob}(|\delta \mathbf{f}| > 0.32 |\delta \mathbf{a}_{c_S}|)$ is typically of the
 382 order of 1%, in particular for our higher Reynolds number. With regards to the viscous force,

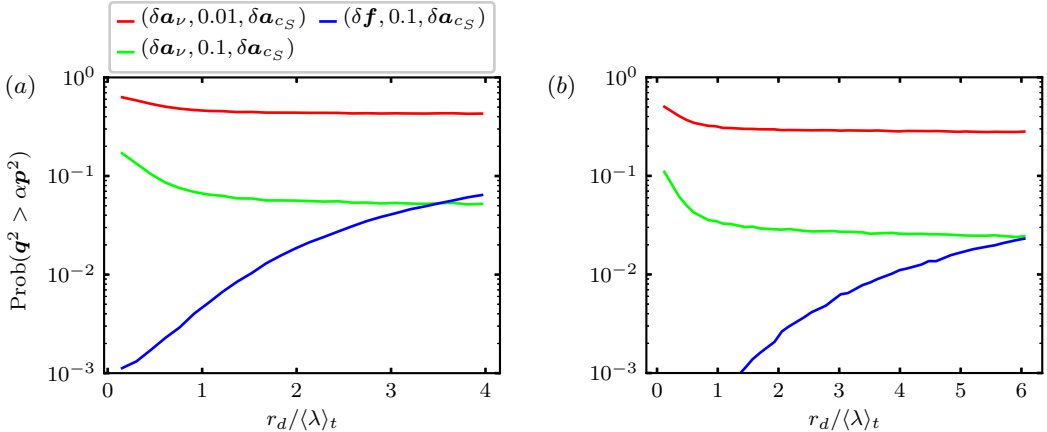


Figure 2: Navier-Stokes difference (NSD) exceedance probabilities $\text{Prob}(\mathbf{q}^2 > \alpha \mathbf{p}^2)$ for the NSD terms on top of (a) as a function of separation length $r_d = |\mathbf{r}|$. The legend entries read $(\mathbf{q}, \alpha, \mathbf{p})$ for the NSD terms introduced in the first paragraph of 3.2. (a) $\langle Re_\lambda \rangle_t = 112$, $\langle L \rangle_t = 3.5 \langle \lambda \rangle_t$. (b) $\langle Re_\lambda \rangle_t = 174$, $\langle L \rangle_t = 5.2 \langle \lambda \rangle_t$. NSD terms are sampled at scale $r_d = |\mathbf{r}|$ at random orientations \mathbf{r} .

383 $\text{Prob}(|\delta \mathbf{a}_\nu| > 0.32 |\delta \mathbf{a}_{c_S}|)$ is typically of the order of 5% for $r \geq \langle \lambda \rangle_t$ and even less for our
 384 higher Reynolds number.

385 The link between non-linearity and non-locality (via the pressure field) invoked in the two-
 386 point analysis of Yasuda & Vassilicos (2018) has its root in equation (3.13) which parallels
 387 (3.7) and states that $\delta \mathbf{a}_{c_l}$ and $\delta \mathbf{a}_p$ are perfectly aligned and have the same magnitudes.
 388 Furthermore, similarly to the way that equation (3.6) supports the concept of sweeping of
 389 small turbulent eddies by large ones in the usual one-point sense, (3.12) suggests similar
 390 magnitudes for and strong alignment between $\delta \mathbf{a}_l$ and $-\delta \mathbf{a}_{c_S}$. A two-point concept of
 391 sweeping similar to the one of Tennekes (1975) which relies on alignment between $\delta \mathbf{a}_l$ and
 392 $-\delta \mathbf{a}_c$ should also require that $\delta \mathbf{a}_c$ tends towards $\delta \mathbf{a}_{c_S}$ with increasing Reynolds number,
 393 i.e. that $\delta \mathbf{a}_c$ becomes increasingly solenoidal. We therefore seek to obtain inequalities and
 394 approximate equalities similar to (3.8). Note that equations (3.12)-(3.13) immediately imply
 395 $\langle \delta \mathbf{a}_{c_S}^2 \rangle \approx \langle \delta \mathbf{a}_l^2 \rangle$, $\langle \delta \mathbf{a}_{c_l}^2 \rangle = \langle \delta \mathbf{a}_p^2 \rangle$ and $\langle \delta \mathbf{a}_p^2 \rangle \approx \langle \delta \mathbf{a}^2 \rangle$. It therefore remains to argue that
 396 $\langle \delta \mathbf{a}_c^2 \rangle \geq \langle \delta \mathbf{a}_{c_S}^2 \rangle \gg \langle \delta \mathbf{a}_{c_l}^2 \rangle$ which is exactly what we need to complete the new concept of
 397 two-point sweeping.

398 We start from

$$399 \quad \langle \delta \mathbf{q} \cdot \delta \mathbf{q} \rangle(\mathbf{r}) = \langle \mathbf{q}^+ \cdot \mathbf{q}^+ \rangle - \langle \mathbf{q}^+ \cdot \mathbf{q}^- \rangle + \langle \mathbf{q}^- \cdot \mathbf{q}^- \rangle - \langle \mathbf{q}^- \cdot \mathbf{q}^+ \rangle, \quad (3.14)$$

$$400 \quad = 2[\langle \mathbf{q} \cdot \mathbf{q} \rangle - \langle \mathbf{q}^+ \cdot \mathbf{q}^- \rangle(\mathbf{r})], \quad (3.15)$$

402 where $\mathbf{q}^+ \equiv \mathbf{q}(\mathbf{x} + \mathbf{r}/2)$ and $\mathbf{q}^- \equiv \mathbf{q}(\mathbf{x} - \mathbf{r}/2)$ and where we used $\langle \mathbf{q}^+ \cdot \mathbf{q}^+ \rangle = \langle \mathbf{q}^- \cdot \mathbf{q}^- \rangle =$
 403 $\langle \mathbf{q} \cdot \mathbf{q} \rangle$ because of statistical homogeneity/periodicity. Previous studies (Hill & Thoroddsen
 404 1997; Vedula & Yeung 1999; Xu *et al.* 2007; Gulitski *et al.* 2007) demonstrated that fluid
 405 accelerations, pressure-gradients and viscous forces have limited spatial correlations in terms
 406 of alignments at scales larger than $\langle \lambda \rangle_t$ for moderate and high $\langle Re_\lambda \rangle_t$. Thus, if we assume
 407 the two-point term to be negligible compared to the one-point term in Eq. (3.15) for scales
 408 $|\mathbf{r}|$ larger than $\langle \lambda \rangle_t$, we have that $\langle \delta \mathbf{q} \cdot \delta \mathbf{q} \rangle(\mathbf{r})$ is approximately equal to $2\langle \mathbf{q} \cdot \mathbf{q} \rangle$ for $|\mathbf{r}|$ larger
 409 than $\langle \lambda \rangle_t$. From (3.8) we therefore obtain

$$410 \quad \langle \delta \mathbf{a}_c^2 \rangle \geq \langle \delta \mathbf{a}_{c_S}^2 \rangle \approx \langle \delta \mathbf{a}_l^2 \rangle \gg \langle \delta \mathbf{a}_{c_l}^2 \rangle = \langle \delta \mathbf{a}_p^2 \rangle \approx \langle \delta \mathbf{a}^2 \rangle \gg \langle \delta \mathbf{a}_\nu^2 \rangle \gg \langle \delta \mathbf{f}^2 \rangle, \quad (3.16)$$

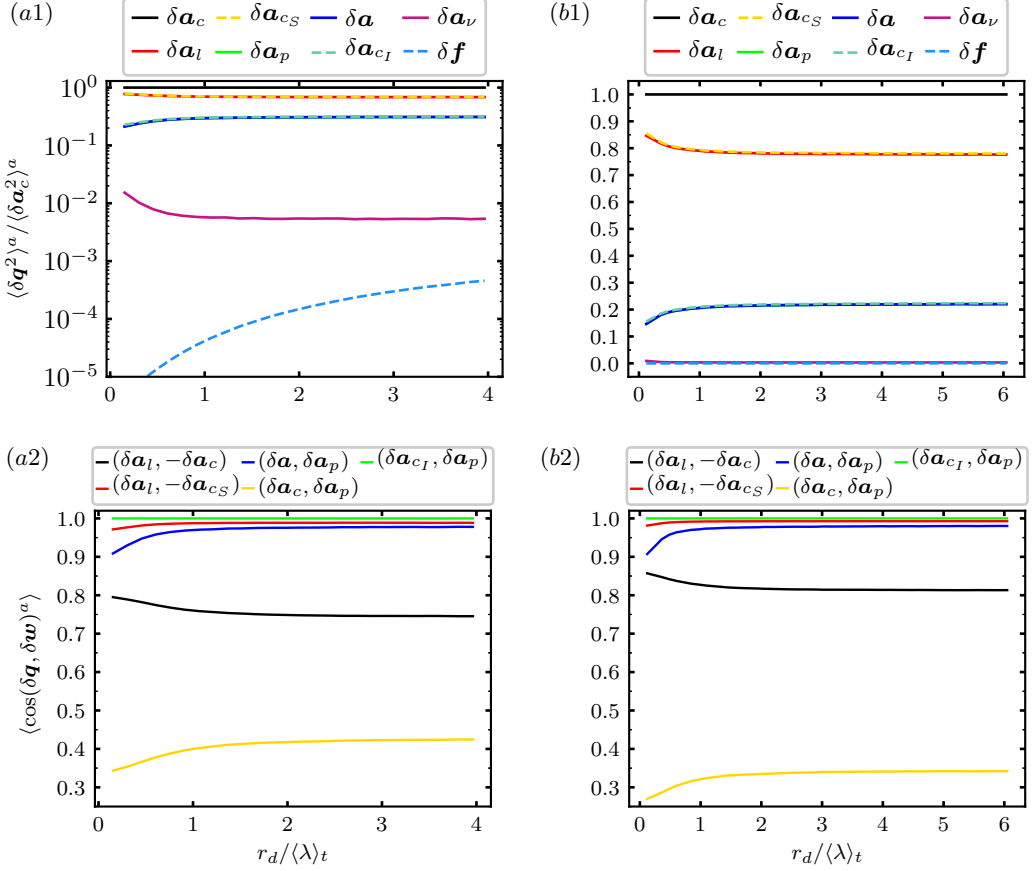


Figure 3: (a1,b1) spatio-temporal averages of spherically averaged NSD magnitudes $\langle \delta \mathbf{q}^2 \rangle^a \equiv (\pi r_d^2)^{-1} \iiint_{|\mathbf{r}|=r_d} \delta \mathbf{q}(\mathbf{x}, \mathbf{r}, t) \cdot \delta \mathbf{q}(\mathbf{x}, \mathbf{r}, t) d\mathbf{r}$ for NSD terms $\delta \mathbf{q}$ listed on top of the figures as a function of r_d : (a1) $\langle Re_\lambda \rangle_t = 112$, (b1) $\langle Re_\lambda \rangle_t = 174$. The magnitudes of the terms $\delta \mathbf{a}_l$ and $\delta \mathbf{a}_{c_S}$ overlap and the magnitudes of the terms $(\delta \mathbf{a}_p, \delta \mathbf{a}$ and $\delta \mathbf{a}_{c_I})$ also overlap. (a2, b2) average NSD alignments between NSD terms $(\delta \mathbf{q}, \delta \mathbf{w})$ listed on top of the figures as a function of r_d : (a2) $\langle Re_\lambda \rangle_t = 112$, (b2) $\langle Re_\lambda \rangle_t = 174$.

411 for $|\mathbf{r}|$ larger than $\langle \lambda \rangle_t$, but $\langle \delta \mathbf{a}_c^2 \rangle \geq \langle \delta \mathbf{a}_{c_S}^2 \rangle$ and $\langle \delta \mathbf{a}_{c_I}^2 \rangle = \langle \delta \mathbf{a}_p^2 \rangle$ are in fact valid for any
 412 \mathbf{r} . Inequality $\langle \delta \mathbf{a}_c^2 \rangle \geq \langle \delta \mathbf{a}_{c_S}^2 \rangle$ follows from $\langle \delta \mathbf{a}_c^2 \rangle = \langle \delta \mathbf{a}_{c_I}^2 \rangle + \langle \delta \mathbf{a}_{c_S}^2 \rangle$ which itself follows
 413 from $\langle \mathbf{a}_{c_I}(\mathbf{x}, t) \cdot \mathbf{a}_{c_S}(\mathbf{x} + \mathbf{r}, t) \rangle_x = 0$ for any \mathbf{r} if the turbulence is isotropic (Monin *et al.*
 414 1975). Equality $\langle \delta \mathbf{a}_{c_I}^2 \rangle = \langle \delta \mathbf{a}_p^2 \rangle$ follows directly from (3.13) which is exact and holds for
 415 any \mathbf{r} and any Reynolds number. Of equalities/inequalities (3.16), the ones that we did not
 416 already directly derive from/with equations (3.12)-(3.13) are $\langle \delta \mathbf{a}_c^2 \rangle \geq \langle \delta \mathbf{a}_{c_S}^2 \rangle \gg \langle \delta \mathbf{a}_{c_I}^2 \rangle$
 417 and $\langle \delta \mathbf{a}_v^2 \rangle \gg \langle \delta \mathbf{f}^2 \rangle$. The present way to formulate the new concept of two-point sweeping
 418 follows from Tsinober's way to formulate sweeping and is encapsulated in $\delta \mathbf{a}_{c_S}^2 \approx \langle \delta \mathbf{a}_l^2 \rangle \gg$
 419 $\langle \delta \mathbf{a}_{c_I}^2 \rangle = \langle \delta \mathbf{a}_p^2 \rangle \approx \langle \delta \mathbf{a}^2 \rangle$ and in the alignments implied by equations (3.12)-(3.13). We
 420 confirm equations (3.12)-(3.13)-(3.16) with our DNS in the remainder of this subsection.

421 To test (3.16) with our DNS data in a manageable way, we calculate spatio-temporal

422 averages of \mathbf{r} -orientation-averaged quantities

$$423 \quad (\delta\mathbf{q} \cdot \delta\mathbf{q})^a(\mathbf{x}, r_d, t) \equiv \frac{1}{\pi r_d^2} \iiint_{|\mathbf{r}|=r_d} \delta\mathbf{q}(\mathbf{x}, \mathbf{r}, t) \cdot \delta\mathbf{q}(\mathbf{x}, \mathbf{r}, t), \quad \mathbf{dr}, \quad (3.17)$$

424 which we plot in figure 3(a1,a2) as ratios of such quantities versus two-point length r_d .
 425 In figure 3(a1,a2) we plot spatio-temporal averages of \mathbf{r} -orientation-averaged quantities
 426 (3.17) for various acceleration/force terms in the NSD and the Helmholtz decomposed
 427 NSD equations. A comparison of relative magnitudes in the plots of figure 3(a1,a2) with
 428 relative magnitudes in table 2 makes it clear that the results are consistent with (3.16) and
 429 $\langle \delta\mathbf{q} \cdot \delta\mathbf{q} \rangle(\mathbf{r}) / \langle \mathbf{q} \cdot \mathbf{q} \rangle$ close to 2 for $r_d \geq \langle \lambda \rangle_t$ at both $\langle Re_\lambda \rangle_t$ to a good degree of accuracy
 430 ($\langle \delta\mathbf{q} \cdot \delta\mathbf{q} \rangle(\mathbf{r}) / \langle \mathbf{q} \cdot \mathbf{q} \rangle$ increases from 1.8 to 2.0 as r_d grows from $\langle \lambda \rangle_t$ to $\langle L \rangle_t$). Note, in
 431 particular, that in Figure 3(a1,b1) the average quantities corresponding to $\delta\mathbf{a}_l$ and $\delta\mathbf{a}_{c_S}$
 432 overlap and those corresponding to $\delta\mathbf{a}_p$, $\delta\mathbf{a}$ and $\delta\mathbf{a}_{c_I}$ also overlap. At scales below $\langle \lambda \rangle_t$, the
 433 average relative magnitudes change slightly, but the NSD magnitude separations still abide
 434 by (3.16), the NSD analogue to (3.8), at all scales.

435 In figure 3(b1,b2) we use our DNS data to plot spatio-temporal averages of \mathbf{r} -orientation-
 436 averaged cosines of angles between various NSD terms $\delta\mathbf{q}$ and $\delta\mathbf{w}$ to test for average
 437 alignments as a function of r_d . These alignment results are of course in perfect agreement
 438 with (3.13) but they are also in good agreement with (3.12) and acceptable agreement
 439 with $\delta\mathbf{a} \approx \delta\mathbf{a}_p$ (the cosine of the angle between these two acceleration vectors is higher
 440 than 0.9 for all r_d). They also show that we should not expect $\delta\mathbf{a}_l$ to be extremely well
 441 aligned with $-\delta\mathbf{a}_c$ at our moderate Reynolds numbers. This demonstrates the pertinence of
 442 the solenoidal-irrotational decomposition which has revealed very good alignments at our
 443 moderate Reynolds numbers for which there are significantly weaker alignments without this
 444 decomposition.

445 In conclusion, figure 3 provides strong support for equations (3.12)-(3.13)-(3.16) which
 446 establish the two-point link between non-linearity and non-locality, and also a concept of
 447 two-point sweeping.

448 3.3. Interscale transfer and physical space transport accelerations

449 The convective non-linearity is responsible for non-linear turbulence transport through
 450 space and non-linear transfer through scales. We want to separate these two effects and
 451 therefore decompose the two-point non-linear acceleration term $\delta\mathbf{a}_c$ into an interscale transfer
 452 acceleration \mathbf{a}_Π and a physical space transport acceleration $\mathbf{a}_\mathcal{T}$ (Hill 2002), i.e $\delta\mathbf{a}_c = \mathbf{a}_\Pi + \mathbf{a}_\mathcal{T}$
 453 with

$$454 \quad \mathbf{a}_\mathcal{T}(\mathbf{x}, \mathbf{r}, t) = \frac{1}{2}(\mathbf{u}^+ + \mathbf{u}^-) \cdot \nabla_{\mathbf{x}} \delta\mathbf{u}, \quad \mathbf{a}_\Pi(\mathbf{x}, \mathbf{r}, t) = \delta\mathbf{u} \cdot \nabla_{\mathbf{r}} \delta\mathbf{u}. \quad (3.18)$$

455 With this decomposition of the non-linear term, the NSD equation (3.9) reads

$$456 \quad \frac{\partial \delta\mathbf{u}}{\partial t} + \mathbf{a}_\Pi + \mathbf{a}_\mathcal{T} = -\frac{1}{\rho} \nabla_{\mathbf{x}} \delta p + \delta\mathbf{a}_v + \delta\mathbf{f}. \quad (3.19)$$

457 We note relations $\mathbf{a}_\Pi = \delta\mathbf{a}_c + u_j^+ \frac{\partial}{\partial x_j^-} \mathbf{u}^- - u_j^- \frac{\partial}{\partial x_j^+} \mathbf{u}^+$ and $\mathbf{a}_\mathcal{T} = \delta\mathbf{a}_c - u_j^+ \frac{\partial}{\partial x_j^-} \mathbf{u}^- + u_j^- \frac{\partial}{\partial x_j^+} \mathbf{u}^+$
 458 which can be easily used to show that $\langle \mathbf{a}_\Pi^2 \rangle$ and $\langle \mathbf{a}_\mathcal{T}^2 \rangle$ tend towards each other as the amplitude
 459 of the separation vector \mathbf{r} grows above the integral length scale. We report DNS evidence of
 460 this tendency, below in this paper.

461 We want to consider the effects of the interscale transfer and interspace transport terms in
 462 the solenoidal and irrotational NSD dynamics and we therefore need to break down the NSD
 463 equation (3.19) into two equations, one irrotational and one solenoidal. We therefore perform
 464 Helmholtz decompositions in centroid space \mathbf{x} for a given separation \mathbf{r} at time t , for example

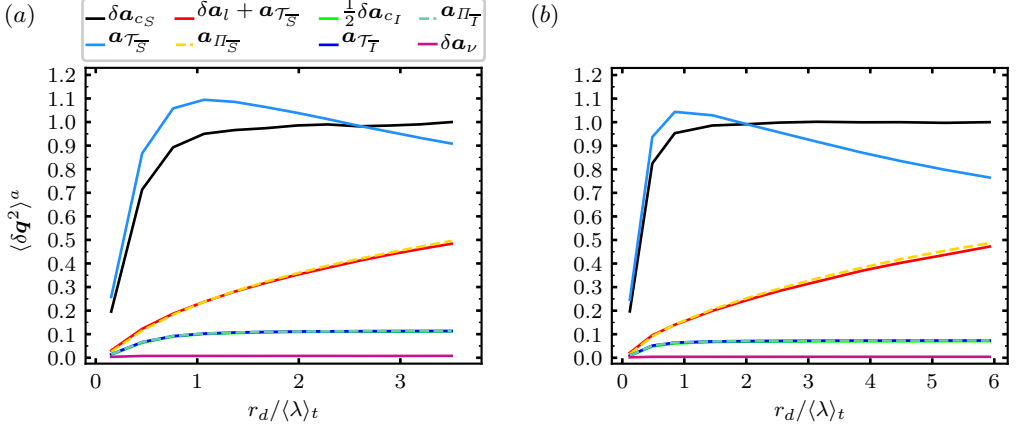


Figure 4: Average magnitudes $\langle \delta q^2 \rangle^a$ of NSD terms present in the irrotational and solenoidal NSD equations (3.21)-(3.22) listed on top of (a). All values have been normalised with $\langle \delta a_{c_S}^2 \rangle^a$ at the largest considered separation r_d . The magnitudes of the terms $(\delta a_l + a_{\tau_S})$ and a_{Π_S} overlap and the magnitudes of the terms $(1/2 \delta a_{c_I}, a_{\tau_I}$ and $a_{\Pi_I})$ also overlap. (a) $\langle Re \lambda \rangle_t = 112$, (b) $\langle Re \lambda \rangle_t = 174$.

465 $\delta \mathbf{q}(\mathbf{x}, \mathbf{r}, t) = \delta \mathbf{q}_I(\mathbf{x}, \mathbf{r}, t) + \delta \mathbf{q}_S(\mathbf{x}, \mathbf{r}, t)$ where $\delta \mathbf{q}_I(\mathbf{x}, \mathbf{r}, t)$ and $\delta \mathbf{q}_S(\mathbf{x}, \mathbf{r}, t)$ are, respectively,
 466 the irrotational and solenoidal parts in centroid space of $\delta \mathbf{q}(\mathbf{x}, \mathbf{r}, t)$. This decomposition in
 467 centroid space differs in general from the difference of the Helmholtz decomposed terms in the
 468 NS equations which gives equations (3.10)-(3.11), but in periodic/homogeneous turbulence
 469 $\delta \mathbf{q}_I = \delta \mathbf{q}_I$ and $\delta \mathbf{q}_S = \delta \mathbf{q}_S$ (see appendix B). Furthermore, from $\delta \mathbf{a}_c = \mathbf{a}_{\Pi} + \mathbf{a}_{\tau}$ immediately
 470 follow $\delta a_{c_S} = a_{\Pi_S} + a_{\tau_S}$ and $\delta a_{c_I} = a_{\Pi_I} + a_{\tau_I}$. Thus, we can rewrite the NSD solenoidal
 471 and irrotational equations (3.10)-(3.11) as

$$472 \quad \mathbf{a}_{\Pi_I} + \mathbf{a}_{\tau_I} = \delta \mathbf{a}_p, \quad (3.20)$$

$$473 \quad \delta a_l + \mathbf{a}_{\Pi_S} + \mathbf{a}_{\tau_S} = \delta \mathbf{a}_v + \delta \mathbf{f}, \quad (3.21)$$

475 in periodic/homogeneous turbulence.

476 We emphasize that the interscale transfer term \mathbf{a}_{Π_S} is related non-locally in space to two-
 477 point vortex stretching and compression terms governing the evolution of vorticity difference
 478 $\delta \omega$. This follows from the fact that, as for the Tsinober equations, the NSD solenoidal
 479 equation is an integrated vorticity difference equation. We provide mathematical detail on
 480 the connection between \mathbf{a}_{Π_S} and $\delta \omega$ in appendix C. This relation between \mathbf{a}_{Π_S} and the
 481 vorticity difference dynamics provides an instantaneous connection between the interscale
 482 momentum dynamics and two-point vorticity stretching and compression dynamics.

483 Equation (3.20) can also be obtained by integrating the Poisson equation for δp in centroid
 484 space similarly to equation (3.21) which, as already mentioned, can be obtained by integrating
 485 the vorticity difference equation in that same space. We use this approach in appendix C
 486 to derive these equations for periodic/homogeneous turbulence but also their generalised
 487 form for non-homogeneous turbulence. By deriving the exact equations for $\mathbf{a}_{\tau_I}(\mathbf{x}, \mathbf{r}, t)$ and
 488 $\mathbf{a}_{\Pi_I}(\mathbf{x}, \mathbf{r}, t)$ in Fourier centroid space we show in appendix B that we have $\mathbf{a}_{\tau_I}(\mathbf{x}, \mathbf{r}, t) =$
 489 $\mathbf{a}_{\Pi_I}(\mathbf{x}, \mathbf{r}, t)$ in periodic/homogeneous turbulence. This result combined with (3.20) yields

$$490 \quad \mathbf{a}_{\Pi_I} = \mathbf{a}_{\tau_I} = \frac{1}{2} \delta \mathbf{a}_p = \frac{1}{2} \delta \mathbf{a}_{c_I}, \quad (3.22)$$

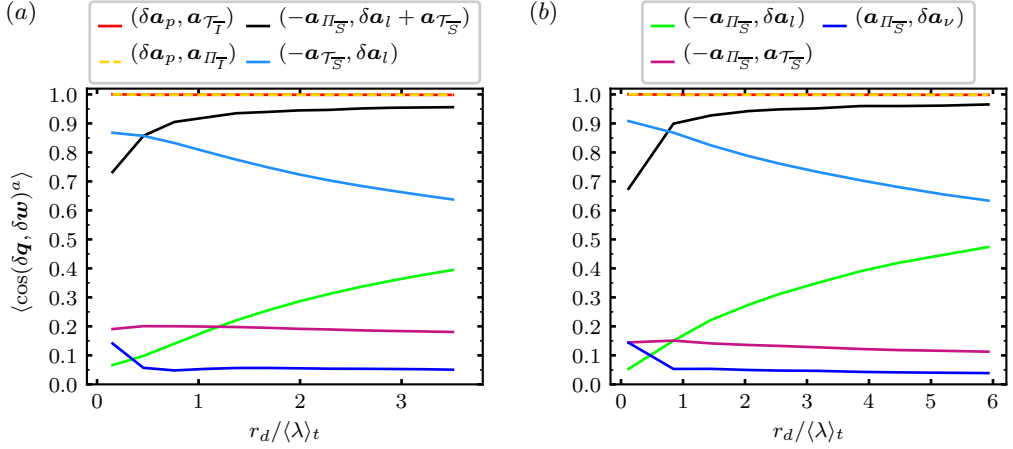


Figure 5: Average alignments of NSD terms $(\delta \mathbf{q}, \delta \mathbf{w})$ listed on top of (a) and (b). The average alignments of $(\delta \mathbf{a}_p, \mathbf{a}_{\mathcal{T}_T})$ and $(\delta \mathbf{a}_p, \mathbf{a}_{\Pi_T})$ overlap: (a) $\langle Re \lambda \rangle_t = 112$, (b) $\langle Re \lambda \rangle_t = 174$.

491 in periodic/homogeneous turbulence. In figure 4 we plot spatio-temporal averages of \mathbf{r} -
 492 orientation-averaged quantities (3.17) for various acceleration/force terms in the NSD and
 493 the Helmholtz decomposed NSD equations and in figure 5 we plot spatio-temporal averages
 494 of \mathbf{r} -orientation-averaged cosines of angles between various two-point acceleration terms in
 495 these equations. The overlapping magnitudes in figure 4 and the average alignments in figure
 496 5 confirm (3.22), or rather validate our DNS given that (3.22) is exact.

497 The computational procedure to calculate the various \mathbf{r} -orientation-averaged terms in
 498 these figures is computationally expensive. To calculate the NSD irrotational and solenoidal
 499 parts of the interscale and interspace transport terms at a given time t and separation \mathbf{r} ,
 500 we use the pseudo-spectral algorithm of Patterson & Orszag (1971) with one phase-shift
 501 and spherical truncation. We apply this algorithm to δu_j and $\partial \delta u_i / \partial r_j$ for the interscale
 502 transfer and for $(u_j^+ + u_j^-) / 2$ and $\partial \delta u_i / \partial x_j$ for the interspace transfer. Hence, we express
 503 these vectors/tensors in Fourier-space (see equations B 13-B 16 in appendix B) and apply the
 504 pseudo-spectral method of Patterson & Orszag (1971) to calculate $\widehat{\mathbf{a}}_{\mathcal{T}}(\mathbf{k}, \mathbf{r}, t)$ and $\widehat{\mathbf{a}}_{\Pi}(\mathbf{k}, \mathbf{r}, t)$
 505 without aliasing errors. We next decompose these fields to irrotational and solenoidal fields
 506 with the projection operator and inverse these fields to physical space to obtain $\mathbf{a}_{\Pi_S}(\mathbf{x}, \mathbf{r}, t)$,
 507 $\mathbf{a}_{\Pi_T}(\mathbf{x}, \mathbf{r}, t)$, $\mathbf{a}_{\mathcal{T}_S}(\mathbf{x}, \mathbf{r}, t)$ and $\mathbf{a}_{\mathcal{T}_T}(\mathbf{x}, \mathbf{r}, t)$. These fields can then be sampled over \mathbf{x} to calculate
 508 e.g. $\mathbf{a}_{\Pi_S}^2(\mathbf{x}, \mathbf{r}, t)$ or KMHM terms such as $2\delta \mathbf{u} \cdot \mathbf{a}_{\Pi_S}(\mathbf{x}, \mathbf{r}, t)$ (see section 3.4). If we assume
 509 that the cost of a DNS time-step is similar to the cost of the pseudo-spectral method to
 510 calculate the NS non-linear term, the calculation of solenoidal and irrotational interspace
 511 and interscale transfers for one t and one \mathbf{r} has similar cost to one DNS time-step. The total
 512 cost of the pseudo-spectral post-processing method is proportional to the total number N_r of
 513 separation vectors \mathbf{r} that we use in our spherical averaging across scales r_d and to the total
 514 number $T_s / \Delta T$ of samples in time (see table 1). With a total number of separation vectors
 515 $N_r \sim 10^3 - 10^4$ and our $T_s / \Delta T$ values, the total cost of the pseudo-spectral post-processing
 516 method in terms of DNS time-steps is at least one order of magnitude larger than the cost of
 517 the DNS itself. This high post-processing cost limits the possible number of grid points in
 518 this study. If we estimate the wall time of a 1024^3 simulation to be approximately 10 days,
 519 the post-processing would require approximately three to four months.

520 The NSD solenoidal equation (3.21) describes a balance between the time-derivative,
 521 solenoidal interscale transfer, solenoidal interspace transport, viscous and forcing terms.
 522 From the point we made in the sentence directly following equation (3.19), we expect $\langle \mathbf{a}_{\tau_S}^2 \rangle$
 523 and $\langle \mathbf{a}_{\Pi_S}^2 \rangle$ to tend to become equal to each other as the amplitude of \mathbf{r} tends to values
 524 significantly larger than $\langle L \rangle_t$. Figure 4 confirms this trend for the second order orientation-
 525 averaged moments of \mathbf{a}_{τ_S} and \mathbf{a}_{Π_S} . For brevity, in what follows we refer to such statistics
 526 as second order magnitudes. With decreasing r_d , the magnitudes of \mathbf{a}_{Π_S} decrease relative to
 527 those of \mathbf{a}_{τ_S} . At all scales $r_d \geq \langle \lambda \rangle_t$ the second order magnitudes of \mathbf{a}_{τ_S} and \mathbf{a}_{Π_S} are one
 528 order of magnitude larger than those of the viscous term $\delta \mathbf{a}_v$ and this separation is greater
 529 for the larger $\langle Re_\lambda \rangle_t$. The magnitudes of $\delta \mathbf{a}_v$ are themselves much larger than those of $\delta \mathbf{f}$
 530 (not shown in figure 4 for not overloading the figure but see figure 3a1). These observations
 531 suggest that the solenoidal NSD equation (3.21) reduces to the approximate

$$532 \quad \delta \mathbf{a}_l + \mathbf{a}_{\tau_S} \approx -\mathbf{a}_{\Pi_S}, \quad (3.23)$$

533 where this equation is understood as typical in terms of second order magnitudes: i.e. in
 534 most regions of the flow for the majority of the time, the removed terms are at least one
 535 order of magnitude smaller than the retained terms. (As for the NS dynamics, we do expect
 536 dynamically important regions localised in space and time where the dynamics differ from
 537 (3.23).) Figure 4 confirms equation (3.23) in a second order sense and shows that the
 538 relatively rare spatio-temporal events which are neglected when writing equation (3.23) are
 539 indeed present as the second order statistics do show a very small deviation from equation
 540 (3.23). An additional important observation to be made from figure 4 is that $\delta \mathbf{a}_{c_S}$ tends to
 541 become increasingly dominated by \mathbf{a}_{τ_S} rather than \mathbf{a}_{Π_S} as r_d decreases.

542 Equation (3.23) is the same as equation (3.12), and similarly to figure 3 which provides
 543 support for equation (3.12), figures 4 and 5 provide strong support for equation (3.23), in
 544 particular for $r_d > \langle \lambda \rangle_t$. It is interesting to note that the average alignment between the left
 545 and the right hand side of equation (3.23) lies between 90% and 100% (typically 95%) for
 546 $r_d > \langle \lambda \rangle_t$. Whilst this is strong support for approximate equation (3.23), the fact that the
 547 alignment is not 100% is a reminder of the nature of the approximation, i.e. that relatively rare
 548 spatio-temporal events do exist where the viscous and/or driving forces are not negligible.

549 At length-scales $r_d \leq \langle \lambda \rangle_t$, the alignment between $\delta \mathbf{a}_l$ and $-\mathbf{a}_{\tau_S}$ improves while the
 550 alignment between $\delta \mathbf{a}_l + \mathbf{a}_{\tau_S}$ and $-\mathbf{a}_{\Pi_S}$ worsens with decreasing r_d (see figure 5) presumably
 551 because of direct dissipation and diffusion effects, so that $\delta \mathbf{a}_l + \mathbf{a}_{\tau_S} \approx 0$ becomes a better
 552 approximation than equation (3.23) at $r_d < 0.5 \langle \lambda \rangle_t$. This observation is consistent with
 553 our parallel observation that the magnitude of \mathbf{a}_{τ_S} increases while the magnitude of \mathbf{a}_{Π_S}
 554 decreases with decreasing r_d and that $\delta \mathbf{a}_{c_S}$ in equation (3.12) tends to be dominated by \mathbf{a}_{τ_S}
 555 at the very smallest scales.

556 On the other end of the spectrum, i.e. as the length scale r_d grows towards $\langle L \rangle_t$, the
 557 alignment between $\delta \mathbf{a}_l$ and $-\mathbf{a}_{\tau_S}$ worsens while the alignment between $\delta \mathbf{a}_l$ and $-\mathbf{a}_{\Pi_S}$
 558 improves (see figure 5), both reaching a comparable level of alignment/misalignment
 559 which contribute together to keep approximation (3.23) statistically well satisfied with 95%
 560 alignment between $\delta \mathbf{a}_l + \mathbf{a}_{\tau_S}$ and $-\mathbf{a}_{\Pi_S}$.

561 The strong anti-alignment between \mathbf{a}_{τ_S} and $\delta \mathbf{a}_l$, increasingly so at smaller r_d (see figure
 562 5) expresses the sweeping of the two-point momentum difference $\delta \mathbf{u}$ at scales r_d and smaller
 563 by the mainly large scale velocity $(\mathbf{u}^+ + \mathbf{u}^-)/2$. Note that this two-point sweeping differs
 564 from anti-alignment between $\delta \mathbf{a}_l$ and $\delta \mathbf{a}_c$ for two reasons. Firstly, by using the Helmholtz
 565 decomposition we have removed the pressure effect embodied in the \mathbf{a}_{c_l} contribution to \mathbf{a}_c
 566 which balances the pressure-gradient. This was first understood in Tsinober *et al.* (2001) in
 567 a one-point setting and is here extended to a two-point setting. Secondly, $\delta \mathbf{a}_{c_S}$ is the sum of

568 an interspace transport $\mathbf{a}_{\mathcal{T}_S}$ and an interscale transfer term \mathbf{a}_{Π_S} such that the interpretation
 569 of two-point sweeping as anti-alignment between \mathbf{a}_{c_S} and \mathbf{a}_l as sweeping cannot be exactly
 570 accurate. The advection of $\delta\mathbf{u}$ by the large scale velocity is attributable to $\mathbf{a}_{\mathcal{T}_S}$, and figure
 571 5 shows that the two-point sweeping anti-alignment between $\delta\mathbf{a}_l$ and $\mathbf{a}_{\mathcal{T}_S}$ increases with
 572 decreasing r_d .

573 The sweeping anti-alignment between $\delta\mathbf{a}_l$ and $\mathbf{a}_{\mathcal{T}_S}$ is by no means perfect even if it reaches
 574 about 90% accuracy at $r_d < \langle\lambda\rangle_t$, as is clear from the similar magnitudes and very strong
 575 alignment tendency between $\delta\mathbf{a}_l + \mathbf{a}_{\mathcal{T}_S}$ and $-\mathbf{a}_{\Pi_S}$ at scales $|\mathbf{r}| \geq \langle\lambda\rangle_t$ (see figures 4 and 5).
 576 Note, in passing, that the Lagrangian solenoidal acceleration $\delta\mathbf{a}_l + \mathbf{a}_{\mathcal{T}_S}$ and \mathbf{a}_{Π_S} are both
 577 Galilean invariant. Equation (3.23) may be interpreted to mean that the Lagrangian solenoidal
 578 acceleration of $\delta\mathbf{u}$ (which is actually solenoidal) moving with the mainly large scale velocity
 579 $(\mathbf{u}^+ + \mathbf{u}^-)/2$, namely $\delta\mathbf{a}_l + \mathbf{a}_{\mathcal{T}_S}$, is evolving in time and space in response to $-\mathbf{a}_{\Pi_S}$: when
 580 there is an influx of momentum from larger scales there is an increase in $\delta\mathbf{a}_l + \mathbf{a}_{\mathcal{T}_S}$ and $\delta\mathbf{u}$
 581 and vice versa.

582 3.4. From NSD dynamics to KHMH dynamics in homogeneous/periodic turbulence

583 The scale-by-scale evolution of $|\delta\mathbf{u}|^2$ locally in space and time is governed by a KHMH
 584 equation. This makes KHMH equations crucial tools for examining the turbulent energy
 585 cascade. The original KHMH equation and the new solenoidal and irrotational KHMH
 586 equations that we derive below are simply projections of the corresponding NSD equations
 587 onto $2\delta\mathbf{u}$. Hence, KHMH dynamics depend on NSD dynamics and the various NSD terms'
 588 alignment or non-alignment tendencies with $2\delta\mathbf{u}$. In this subsection we present five KHMH
 589 results all clearly demarcated and identified in *italics*.

590 By contracting the NSD equation (3.9) with $2\delta\mathbf{u}$, one obtains the KHMH equation (Hill
 2002; Yasuda & Vassilicos 2018):

$$592 \quad \frac{\partial}{\partial t} |\delta\mathbf{u}|^2 + \frac{u_k^+ + u_k^-}{2} \frac{\partial}{\partial x_k} |\delta\mathbf{u}|^2 + \frac{\partial}{\partial r_k} (\delta u_k |\delta\mathbf{u}|^2) = -\frac{2}{\rho} \frac{\partial}{\partial x_k} (\delta u_k \delta p) + 2\nu \frac{\partial^2}{\partial r_k^2} |\delta\mathbf{u}|^2$$

$$593 \quad + \frac{\nu}{2} \frac{\partial^2}{\partial x_k^2} |\delta\mathbf{u}|^2 - \left[2\nu \left(\frac{\partial u_i^+}{\partial x_k^+} \right)^2 + 2\nu \left(\frac{\partial u_i^-}{\partial x_k^-} \right)^2 \right] + 2\delta u_k \delta f_k, \quad (3.24)$$

594 where no fluid velocity decomposition nor averaging operations have been used. In line with
 595 the naming convention of Yasuda & Vassilicos (2018) this equation can be written

$$596 \quad \mathcal{A}_t + \mathcal{T} + \Pi = \mathcal{T}_p + \mathcal{D}_{r,\nu} + \mathcal{D}_{x,\nu} - \epsilon + \mathcal{I}, \quad (3.25)$$

597 where the first, second and third terms on the left hand sides of equations (3.24) and (3.25)
 598 correspond to each other and so do the first, second, third, fourth and fifth terms on the
 599 right hand sides. Preempting notation used further down in this paper, equation (3.25) is also
 600 written $\mathcal{A} = \mathcal{T}_p + \mathcal{D} + \mathcal{I}$ or $\mathcal{A}_t + \mathcal{A}_c = \mathcal{T}_p + \mathcal{D} + \mathcal{I}$ where $\mathcal{A}_c \equiv \mathcal{T} + \Pi$, $\mathcal{A} \equiv \mathcal{A}_t + \mathcal{A}_c$ and
 601 $\mathcal{D} \equiv \mathcal{D}_{r,\nu} + \mathcal{D}_{x,\nu} - \epsilon$.

602 To examine the KHMH dynamics in terms of irrotational and solenoidal dynamics we
 603 contract the irrotational and solenoidal NSD equations with $2\delta\mathbf{u}$ to derive what we refer to as
 604 irrotational and solenoidal KHMH equations. Each of the KHMH terms can be subdivided
 605 into a contribution from the NSD irrotational part and a contribution from the NSD solenoidal
 606 part of the respective term in the NSD equation. A solenoidal KHMH term corresponding
 607 to a $\delta\mathbf{q}(\mathbf{x}, \mathbf{r}, t)$ or $\mathbf{q}(\mathbf{x}, \mathbf{r}, t)$ term in equation (3.21) equals $\mathcal{Q}_S = 2\delta\mathbf{u} \cdot \delta\mathbf{q}_S$ or $\mathcal{Q}_S = 2\delta\mathbf{u} \cdot \mathbf{q}_S$,
 608 and an irrotational KHMH term corresponding to a $\delta\mathbf{q}(\mathbf{x}, \mathbf{r}, t)$ or $\mathbf{q}(\mathbf{x}, \mathbf{r}, t)$ term in equation
 609 (3.22) equals $\mathcal{Q}_I = 2\delta\mathbf{u} \cdot \delta\mathbf{q}_I$ or $\mathcal{Q}_I = 2\delta\mathbf{u} \cdot \mathbf{q}_I$. With $\mathcal{Q} = 2\delta\mathbf{u} \cdot \delta\mathbf{q}$ or $\mathcal{Q} = 2\delta\mathbf{u} \cdot \mathbf{q}$, we have
 610 $\mathcal{Q} = \mathcal{Q}_I + \mathcal{Q}_S$. The irrotational and solenoidal KHMH equations for periodic/homogeneous

611 turbulence follow from equations (3.21) and (3.22) respectively and read

$$612 \quad \mathcal{A}_t + \mathcal{T}_{\overline{S}} + \Pi_{\overline{S}} = \mathcal{D}_{r,v} + \mathcal{D}_{x,v} - \epsilon + \mathcal{I}, \quad (3.26)$$

$$613 \quad \Pi_{\overline{I}} = \mathcal{T}_{\overline{I}} = \frac{1}{2} \mathcal{T}_p, \quad (3.27)$$

614 where use has been made of the fact that the velocity and velocity difference fields are solenoidal. *These two equations are our first KMHM result.*

617 Space-local changes in time of $|\delta\mathbf{u}|^2$, expressed via \mathcal{A}_t , are only due to solenoidal KMHM
618 dynamics in equation (3.26) which include interspace transport, interscale transport, viscous
619 and forcing effects. The irrotational KMHM equation (3.27) formulates how the imposition
620 of incompressibility by the pressure field affects interspace and interscale dynamics and, in
621 turn, energy cascade dynamics. Generalised solenoidal and irrotational KMHM equations
622 also valid for non-periodic/non-homogeneous turbulence are given in appendix C.

623 We first consider the spatio-temporal average of these equations in statistically steady
624 forced periodic/homogeneous turbulence. As $\langle \mathcal{T}_p \rangle = 0$, we obtain from equation (3.27),
625 $\langle \Pi_{\overline{I}} \rangle = \langle \mathcal{T}_{\overline{I}} \rangle = 0$. As $\langle \mathcal{T}_{\overline{S}} \rangle + \langle \mathcal{T}_{\overline{I}} \rangle = \langle \mathcal{T} \rangle = 0$, we have $\langle \mathcal{T}_{\overline{S}} \rangle = 0$, such that the spatio-temporal
626 average of (3.26) reads

$$627 \quad \langle \Pi \rangle = \langle \Pi_{\overline{S}} \rangle = \langle \mathcal{D}_{r,v} \rangle - \langle \epsilon \rangle + \langle \mathcal{I} \rangle. \quad (3.28)$$

628 If an intermediate inertial subrange of scales $|\mathbf{r}|$ can be defined where viscous diffusion
629 and forcing are negligible, equation (3.28) reduces to $\langle \Pi_{\overline{S}} \rangle \approx -\langle \epsilon \rangle$ in that range. This
630 theoretical conclusion (which is not part of our DNS study) is the backbone of the Kolmogorov
631 (1941a,b,c) theory for high Reynolds number statistically homogeneous stationary small-
632 scale turbulence with the additional information that *the part of the average interscale transfer*
633 *rate involved in Kolmogorov's equilibrium balance is the solenoidal interscale transfer rate*
634 *only. This is our second KMHM result.* On average, there is a cascade of turbulence energy
635 from large to small scales where the rate of interscale transfer is dominated by two-point
636 vortex stretching (see appendix C for the relation between the solenoidal interscale transfer
637 and vortex stretching) and is equal to $-\langle \epsilon \rangle$ independently of $|\mathbf{r}|$ over a range of scales where
638 viscous diffusion and forcing are negligible.

639 In this paper we concentrate on the fluctuations around the average picture described by
640 the scale-by-scale equilibrium (3.28) for any Reynolds number. If we subtract the spatio-
641 temporal average solenoidal KMHM equation (3.28) from the solenoidal KMHM equation
642 (3.26) and use the generic notation $Q' \equiv Q - \langle Q \rangle$, we attain the fluctuating solenoidal KMHM
643 equation

$$644 \quad \mathcal{A}_t + \mathcal{T}_{\overline{S}} + \Pi'_{\overline{S}} = \mathcal{D}'_{r,v} + \mathcal{D}_{x,v} - \epsilon' + \mathcal{I}'. \quad (3.29)$$

645 This equation governs the fluctuations of the KMHM solenoidal dynamics around its spatio-
646 temporal average. Clearly, if these non-equilibrium fluctuations are large relative to their
647 average values, the average picture expressed by equation (3.28) is not characteristic of the
648 interscale transfer dynamics. We now study the KMHM fluctuations in statistically stationary
649 periodic/homogeneous turbulence on the basis of equations (3.27) and (3.29). Concerning
650 equation (3.27), note that $\Pi'_{\overline{I}} = \Pi_{\overline{I}}$, $\mathcal{T}'_{\overline{I}} = \mathcal{T}_{\overline{I}}$ and $\mathcal{T}'_p = \mathcal{T}_p$.

651 We start by determining the relative fluctuation magnitudes of the spatio-temporal
652 fluctuations of each term in the KMHM equations (3.27) and (3.29). These relative fluctuation
653 magnitudes can emulate those of respective terms in the NSD equations under the following
654 sufficient conditions: (i) the fluctuations are so intense that they dwarf averages, so that
655 $\langle (Q')^2 \rangle \approx \langle Q^2 \rangle$; (ii) the mean square of any KMHM term $Q = 2\delta\mathbf{u} \cdot \delta\mathbf{q}$ corresponding
656 to a NSD term $\delta\mathbf{q}(\mathbf{x}, \mathbf{r}, t)$ (equivalently $Q = 2\delta\mathbf{u} \cdot \mathbf{q}$ corresponding to $\mathbf{q}(\mathbf{x}, \mathbf{r}, t)$) can be

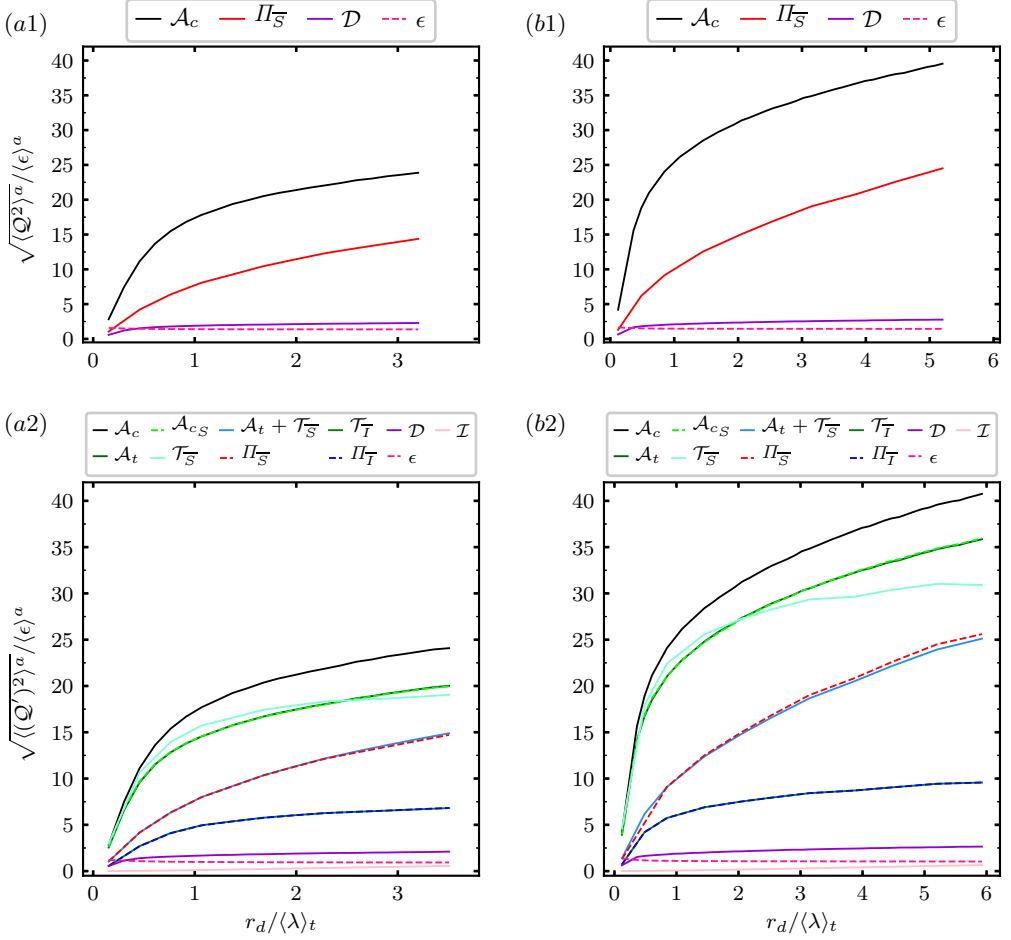


Figure 6: (a1, b1) KHMH average square magnitudes $\langle Q^2 \rangle^a$ and (a2, b2) KHMH average square fluctuating magnitudes $\langle (Q')^2 \rangle^a$, where $Q' = Q - \langle Q \rangle$, for the KHMH terms Q listed above the figures and introduced in the third and fourth paragraph of 3.4. All entries are normalised with $\langle \epsilon \rangle^a$ (see equations (3.24)-(3.25)). The following pairs of KHMH terms have overlapping magnitudes in (a2, b2): \mathcal{A}_t and \mathcal{A}_{cS} ; $\mathcal{A}_t + \mathcal{T}_{\overline{S}}$ and $\Pi_{\overline{S}}$; $\mathcal{T}_{\overline{T}}$ and $\Pi_{\overline{T}}$. (a1, a2) $\langle Re \lambda \rangle_t = 112$, (b1, b2) $\langle Re \lambda \rangle_t = 174$.

657 approximated as

$$658 \quad \langle Q^2 \rangle(\mathbf{r}) \approx 4 \langle |\delta \mathbf{u}|^2 \rangle \langle |\delta \mathbf{q}|^2 \rangle \langle \cos^2(\theta_q) \rangle, \quad (3.30)$$

659 where the approximate equality results from a degree of decorrelation and θ_q is the angle
 660 between $\delta \mathbf{q}(\mathbf{x}, \mathbf{r}, t)$ (or $\mathbf{q}(\mathbf{x}, \mathbf{r}, t)$) and $\delta \mathbf{u}(\mathbf{x}, \mathbf{r}, t)$; (iii) $\langle \cos^2(\theta_q) \rangle$ is not very sensitive to the
 661 choice of NSD term $\delta \mathbf{q}$ (or \mathbf{q}). Under these conditions, we get

$$662 \quad \frac{\langle (2\delta \mathbf{u} \cdot \delta \mathbf{q})^2 \rangle(\mathbf{r})}{\langle (2\delta \mathbf{u} \cdot \delta \mathbf{w})^2 \rangle(\mathbf{r})} \approx \frac{\langle |\delta \mathbf{u}|^2 \rangle \langle |\delta \mathbf{q}|^2 \rangle \langle \cos^2(\theta_q) \rangle(\mathbf{r})}{\langle |\delta \mathbf{u}|^2 \rangle \langle |\delta \mathbf{w}|^2 \rangle \langle \cos^2(\theta_w) \rangle(\mathbf{r})} \approx \frac{\langle |\delta \mathbf{q}|^2 \rangle(\mathbf{r})}{\langle |\delta \mathbf{w}|^2 \rangle(\mathbf{r})}, \quad (3.31)$$

663 which means that KHMH relative fluctuation magnitudes and NSD relative fluctuation
 664 magnitudes are approximately identical. The first approximate equality in (3.31) follows

665 directly from (3.30) and the second approximate equality follows from hypothesis (iii) that
 666 $\cos^2(\theta_q)$ and $\cos^2(\theta_w)$ are about equal.

667 We test hypothesis (i) by comparing the plots in figure 6(a1, b1) with those in figure 6(a2,
 668 b2). Figure 6(a1, b1) shows average magnitudes of KHMH spatio-temporal fluctuations
 669 for terms with non-zero spatio-temporal averages. Comparing with figure 6(a2, b2), we find
 670 $\langle(Q')^2\rangle^a \approx \langle Q^2\rangle^a$, i.e. hypothesis (i), for all four terms plotted in figure 6(a1, b1) at all length
 671 scales r_d considered. Note that this does not hold for $\mathcal{D}'_{r,\nu}$ and \mathcal{I}' which are the only KHMH
 672 fluctuations such that $\sqrt{\langle(Q')^2\rangle^a}/\langle\epsilon\rangle^a$ is smaller (in fact significantly smaller) than 1 at all
 673 scales. Figure 6 makes it also clear that the magnitudes of the fluctuations of all other KHMH
 674 terms (solenoidal and irrotational) are much higher than those of the turbulence dissipation
 675 at all scales $r_d > 0.5\langle\lambda\rangle_t$, and more so for the higher of the two Reynolds numbers. For scales
 676 $r_d \geq \langle\lambda\rangle_t$, the largest average fluctuating magnitudes are those of \mathcal{A}'_c , followed closely by
 677 \mathcal{A}_t and \mathcal{F}'_S . Next come the magnitudes of Π'_S and $\mathcal{A}_t + \mathcal{F}'_S$. Thereafter follow the irrotational
 678 terms $\Pi'_T = \mathcal{T}'_T (= 0.5\mathcal{T}_p)$ and finally the viscous, dissipative and forcing terms \mathcal{D}' , ϵ' and
 679 \mathcal{I}' in that order. *This order of fluctuations is our third KHMH result.* An average description
 680 of the interscale turbulent energy transfer dynamics in terms of its spatio-temporal average
 681 cannot, therefore, be accurate. In order to characterise these dynamics, attention must be
 682 directed at most if not all KHMH term fluctuations, and in fact to much more than just the
 683 turbulence dissipation fluctuations given that they are among the weakest.

684 Next, we test hypothesis (ii) by testing the validity of (3.30) and hypothesis (iii) concerning
 685 approximately similar $\cos^2(\theta_q)$ behaviour for different KHMH terms. In figure 7(a1, b1) we
 686 plot ratios of right hand sides to left hand sides of equation (3.30) and see that (3.30) is not
 687 valid, but that it is nevertheless about 65% to 98% accurate for $r_d \geq \langle\lambda\rangle_t$. Note that (3.30)
 688 might be sufficient but that it is by no means necessary for the left-most and the right-most
 689 sides of (3.31) to approximately balance. In those cases where the variations between the
 690 ratios plotted in figure 7(a1, b1) are not too large and the assumption of approximately similar
 691 $\cos^2(\theta_q)$ for different KHMH terms more or less holds, the left-most and the right-most sides
 692 of (3.31) can approximately balance.

693 Incidentally, figure 7(a2, b2) also shows that the angles θ_q are not random but that they are
 694 more likely to be small rather than large in an approximately similar way for all important NSD
 695 terms: $\cos^2(\theta_q)$ ranges between about 0.28 and 0.36 for all NSD terms (except the viscous
 696 acceleration difference and the viscous force difference) at all scales r_d . These values are
 697 much smaller than 0.5, the value that $\cos^2(\theta_q)$ would have taken if the angles θ_q were random.
 698 There is therefore an alignment tendency between $\delta\mathbf{u}$ and NSD terms which is similar for
 699 all the important NSD terms, thereby allowing the balance between the left-most (ratio of
 700 KHMH terms) and the right-most (ratio of NSD terms) sides of (3.31) to approximately hold
 701 as seen by comparing the plots (a1)-(b1) (mean square NSD terms) with the plots (a2)-(b2)
 702 (mean square KHMH terms) in figure 8. (Note that the viscous term is bounded from above,
 703 $\langle\mathcal{D}^2\rangle(\mathbf{r}) \leq 4\langle|\delta\mathbf{u}|^2|\delta\mathbf{a}_\nu|^2\rangle$, which indicates limited magnitudes compared to the irrotational
 704 and the dominant solenoidal terms because of the limited magnitude of $\langle\delta\mathbf{a}_\nu^2\rangle$. The limited
 705 fluctuations of the viscous terms are clearly seen in figure 6.)

706 Figure 8 does indeed confirm the close correspondence between NSD and KHMH statistics
 707 which is a significant step further from the correspondence reported earlier in this paper
 708 between NS and NSD statistics. We can therefore use the approximate NSD relation (3.23)
 709 to deduce the following approximate KHMH relation:

$$710 \quad \mathcal{A}_t + \mathcal{F}'_S + \Pi'_S \approx 0, \quad (3.32)$$

712 understood in the sense that it holds in the majority of the domain for the majority of the

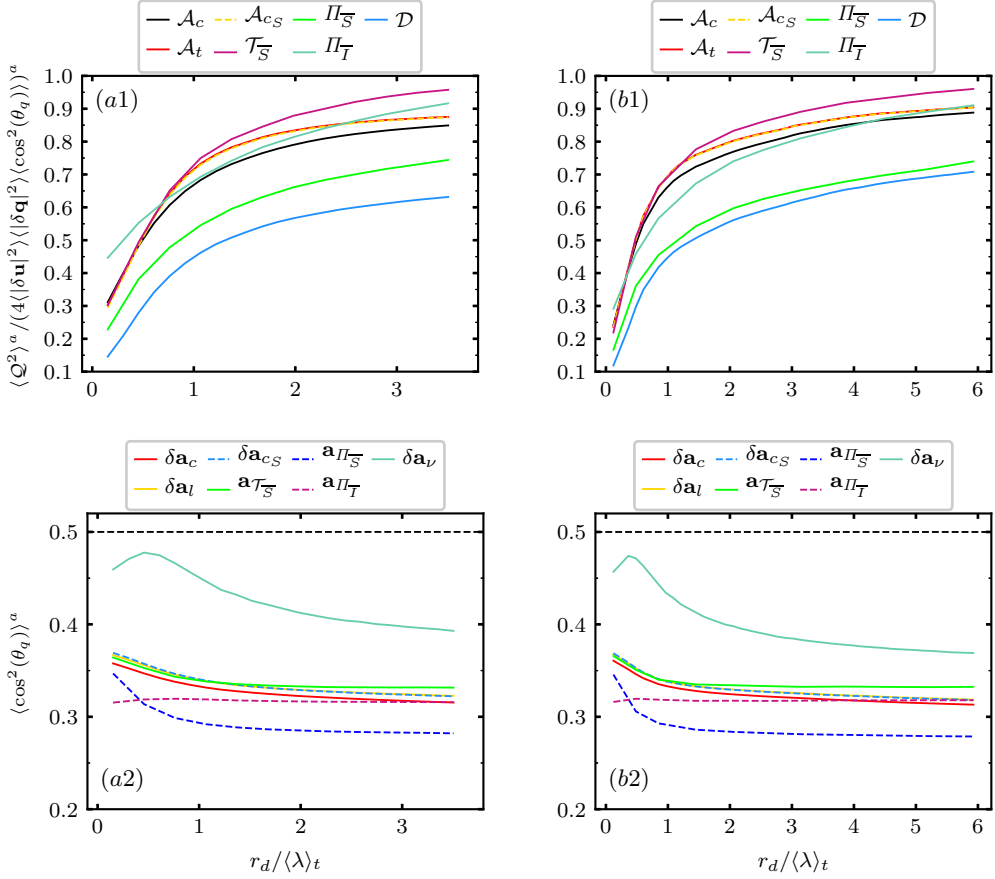


Figure 7: Test of the assumptions (ii) and (iii) in the seventh paragraph of subsection 3.4 related to relations (3.30)-(3.31) connecting NSD and KHMH relative magnitudes. (a1,b1) Test of assumption (ii) by taking the ratio of the left-hand and right-hand sides of (3.30) for the KHMH terms Q listed above the figures. (a2,b2) test of assumption (iii) used in (3.31) by comparing the behaviour of $\langle \cos^2(\theta_q) \rangle^\alpha$ for the various NSD terms listed above the figures. The black horizontal line 0.5 corresponds to the value of $\langle \cos^2(\theta_q) \rangle^\alpha$ if θ_q is uniformly distributed. (a1, a2) $\langle Re_\lambda \rangle_t = 112$, (b1, b2) $\langle Re_\lambda \rangle_t = 174$.

713 time but that there surely exist relatively rare events within the flow where this approximate
 714 KHMH relation is violated.

715 *This approximate equation $\mathcal{A}_t + \mathcal{T}_{\overline{S}} + \Pi'_{\overline{S}} \approx 0$ can be considered to be our fourth KHMH*
 716 *result.* It is consistent with the order of fluctuation magnitudes in figure 8 which shows, in
 717 agreement with the NSD - KHMH correspondence just established, that the largest fluctuating
 718 magnitudes are those of \mathcal{A}_c , followed by the fluctuating magnitudes of $\mathcal{T}_{\overline{S}}$, \mathcal{A}_t and \mathcal{A}_{c_S}
 719 ($\mathcal{A}_{c_S} = \mathcal{T}_{\overline{S}} + \Pi'_{\overline{S}}$). Note though that there is a cross over at about $r_d \approx 2 \langle \lambda \rangle_t$ for both
 720 Reynolds numbers considered here between the fluctuation magnitudes of $\mathcal{T}_{\overline{S}}$ and those of
 721 \mathcal{A}_t and \mathcal{A}_{c_S} which are about equal to each other in agreement with equation (3.32).

722 The fluctuation magnitudes of $\Pi'_{\overline{S}}$ and $\Pi'_{\overline{I}}$ are both smaller than those just mentioned,
 723 and those of $\Pi'_{\overline{I}}$ are significantly smaller than those of $\Pi'_{\overline{S}}$. Even smaller, are the fluctuation
 724 magnitudes of \mathcal{D} and \mathcal{I} , in that order. In agreement with (3.16), our third and fourth KHMH

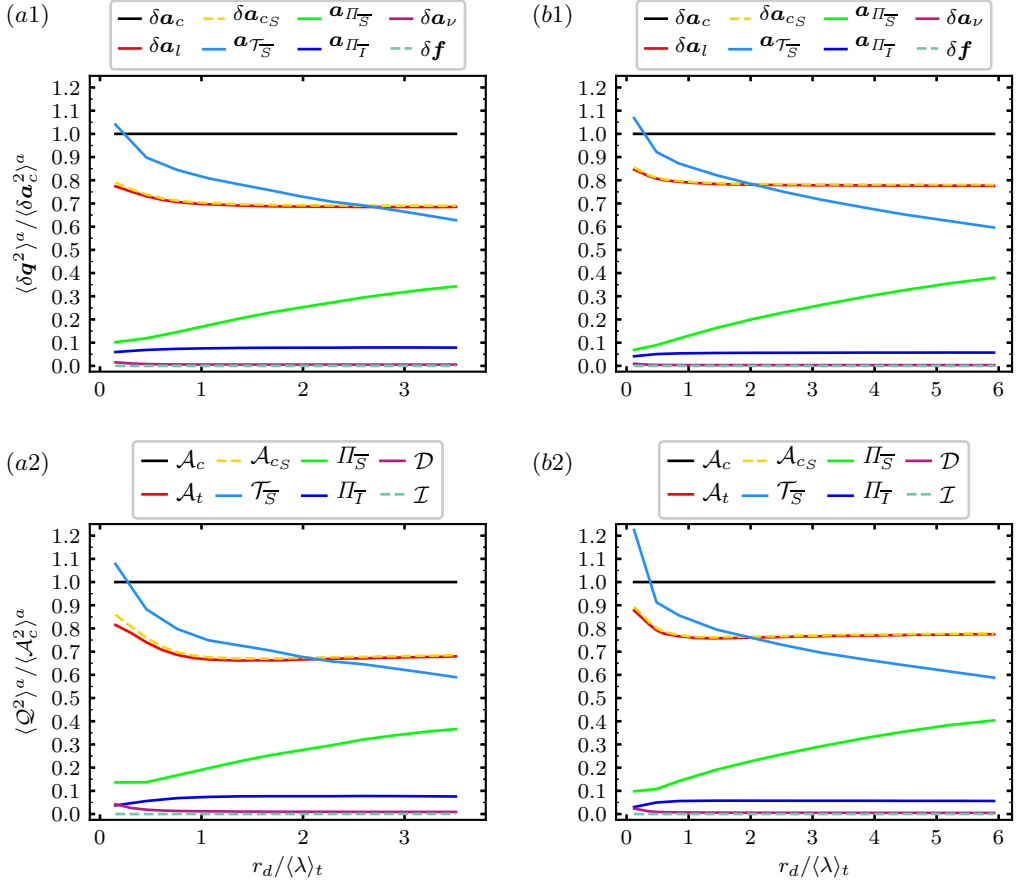


Figure 8: NSD and KHMH relative average square magnitudes (which should be similar on the basis of (3.31)) for the terms listed above the figures: (a1) NSD and (a2) KHMH for $\langle Re\lambda \rangle_t = 112$, (b1) NSD and (b2) KHMH for $\langle Re\lambda \rangle_t = 174$.

725 conclusions incorporate the following:

$$726 \quad \langle \mathcal{A}_t^2 \rangle \approx \langle \mathcal{A}_{c_s}^2 \rangle \gg \langle \mathcal{T}_p^2 \rangle = 4\langle \Pi_T^2 \rangle = 4\langle \mathcal{T}_S^2 \rangle = \langle \mathcal{A}_{c_t}^2 \rangle \gg \langle \mathcal{D}^2 \rangle \gg \langle \mathcal{I}^2 \rangle, \quad (3.33)$$

727 where $\mathcal{A}_{c_t} = \mathcal{T}_T + \Pi_T$.

728 An additional significant observation from figure 8 which we can count as our *fifth KHMH*
 729 *result* is that, as r_d decreases towards about $0.5\langle\lambda\rangle_t$, the fluctuation magnitude of $\mathcal{A}_{c_s} =$
 730 $\mathcal{T}_S + \Pi_S$ remains about constant but that of \mathcal{T}_S increases while that of Π_S decreases. (At
 731 scale r_d smaller than $0.5\langle\lambda\rangle_t$, the fluctuation magnitudes of both \mathcal{A}_{c_s} and \mathcal{T}_S increase with
 732 diminishing r_d whereas those of Π_S remain about constant.) The convective non-linearity is
 733 increasingly of the spatial transport type and diminishingly of the interscale transfer type as
 734 the two-point separation length decreases.

735 We now consider correlations between different intermediate and large scale fluctuating
 736 KHMH terms in light of equations (3.27) and (3.32).

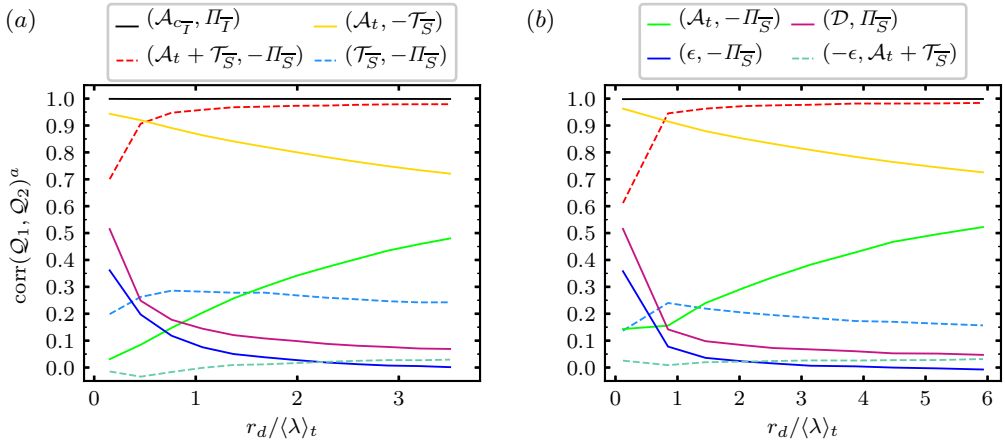


Figure 9: Spherically averaged correlation coefficients between KHMH terms (Q_1, Q_2) listed above the plots (a) and (b). They are plotted as functions of scale r_d . (a) $\langle Re_\lambda \rangle_t = 112$, (b) $\langle Re_\lambda \rangle_t = 174$.

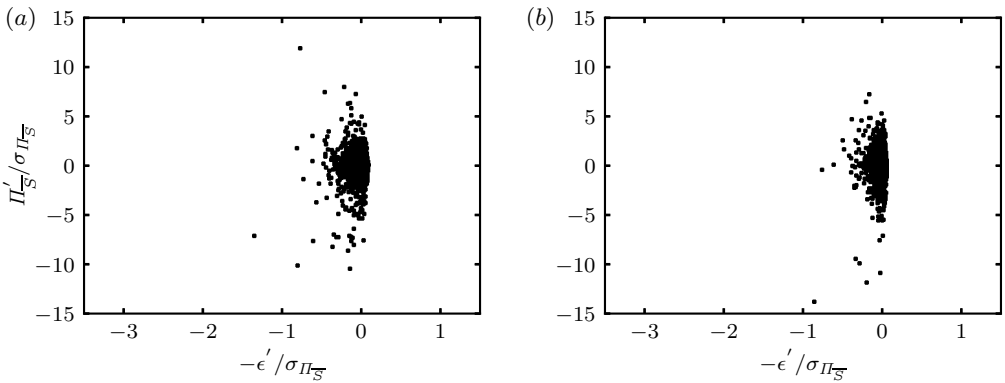


Figure 10: Scatter plots of $\Pi'_{\overline{S}}$ and ϵ' at random orientations \mathbf{r} with $r_d / \langle \lambda \rangle_t = (1.45, 3.1)$ for (a, b), $\sigma_{\Pi'_{\overline{S}}}$ is the standard deviation of $\Pi'_{\overline{S}}$ and $\langle Re_\lambda \rangle_t = 174$.

737 4. Fluctuating KHMH dynamics in homogeneous/periodic turbulence

738

4.1. Correlations

739 We start this section by assessing the existence or non-existence of local (in space and
 740 time) equilibrium between interscale transfer and dissipation at some intermediate scales.
 741 In figure 9 we plot correlations between various KHMH terms. In particular, this figure
 742 shows that the correlation coefficient between $\Pi'_{\overline{S}}$ and $-\epsilon'$ lies well below 0.1 for all
 743 scales $r_d \geq \langle \lambda \rangle_t$. The scatter plots of these quantities in figure 10 confirm the absence
 744 of local relation between interscale transfer rate and dissipation rate. For example, for
 745 a given local/instantaneous dissipation fluctuation, the corresponding local/instantaneous
 746 interscale transfer rate fluctuation can be close to equally positive or negative. There is no
 747 local equilibrium between these quantities as they fluctuate at scales $r_d \geq \langle \lambda \rangle_t$. Such a
 748 correlation should of course not necessarily be expected. However, as r_d decreases below

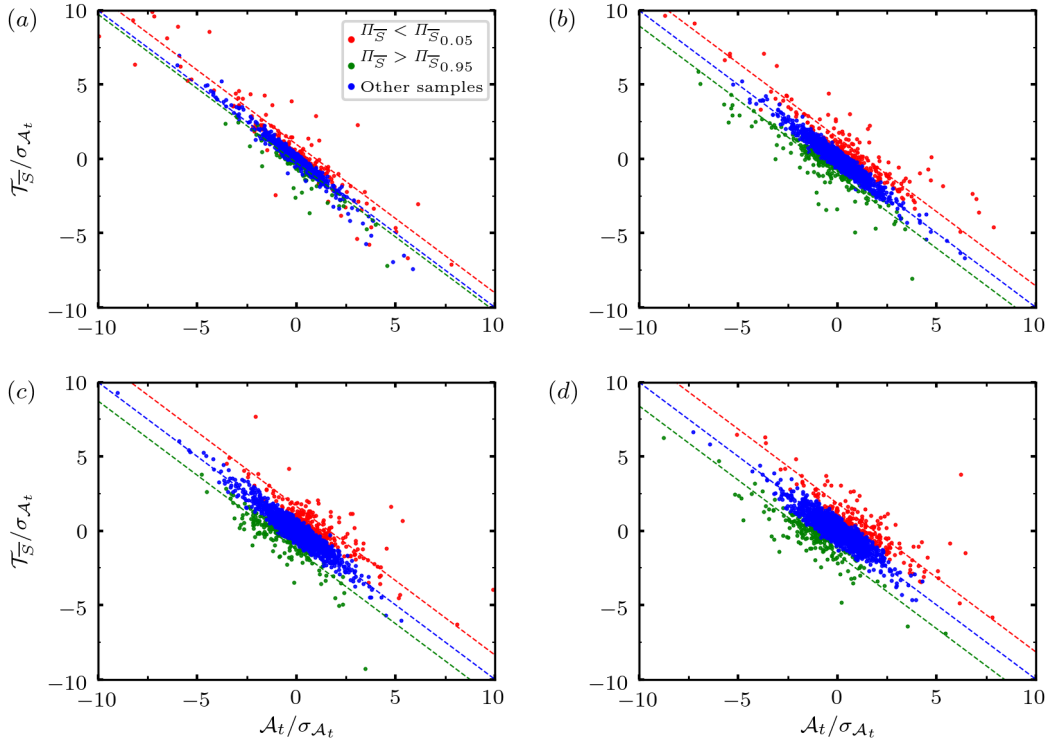


Figure 11: Scatter plots of \mathcal{A}_t and $\mathcal{T}_{\overline{S}}$ at random orientations \mathbf{r} normalised by $\sigma_{\mathcal{A}_t}$ and $\sigma_{\mathcal{T}_{\overline{S}}}$, their respective standard deviations. $\Pi_{\overline{S}_{0.05}}$ is the value of $\Pi_{\overline{S}}$ at the respective r_d for which 5% of the samples are more negative than $\Pi_{\overline{S}_{0.05}}$ and $\Pi_{\overline{S}_{0.95}}$ is the value of $\Pi_{\overline{S}}$ for which 95% of the samples are more positive than $\Pi_{\overline{S}_{0.95}}$. The events $\Pi_{\overline{S}} < \Pi_{\overline{S}_{0.05}}$ and $\Pi_{\overline{S}} > \Pi_{\overline{S}_{0.95}}$ are marked in red and green respectively, while the remaining events are marked in blue. The red line marks $\mathcal{A}_t = -\mathcal{T}_{\overline{S}} - \langle \Pi_{\overline{S}} | \Pi_{\overline{S}} < \Pi_{\overline{S}_{0.05}} \rangle$, where $\langle \Pi_{\overline{S}} | \Pi_{\overline{S}} < \Pi_{\overline{S}_{0.05}} \rangle$ is the average value of $\Pi_{\overline{S}}$ conditioned on $\Pi_{\overline{S}} < \Pi_{\overline{S}_{0.05}}$. The green line marks $\mathcal{A}_t = -\mathcal{T}_{\overline{S}} - \langle \Pi_{\overline{S}} | \Pi_{\overline{S}} > \Pi_{\overline{S}_{0.95}} \rangle$ and the blue line marks $\mathcal{A}_t = -\mathcal{T}_{\overline{S}}$ (with all terms appropriately normalised with $\sigma_{\mathcal{A}_t}$ and $\sigma_{\mathcal{T}_{\overline{S}}}$). $r_d/\langle \lambda \rangle_t = (0.12, 1.45, 3.1, 5.2)$ for (a, b, c, d) and $\langle Re_\lambda \rangle_t = 174$.

749 $\langle \lambda \rangle_t$, the correlations between $\Pi_{\overline{S}}$ and either $-\epsilon'$ or \mathcal{D}' increase up to values between
 750 about 0.3 and about 0.5. This increased correlation may suggest a feeble tendency towards
 751 local/instantaneous equilibrium between interscale transfer rate and dissipation rate at scales
 752 $r_d < \langle \lambda \rangle_t$. However, these scales are strongly affected by direct viscous processes and can
 753 therefore not be inertial range scales.

754 Following the question of local/instantaneous equilibrium, we now look for lo-
 755 cal/instantaneous sweeping. Figure 9 shows strong anti-correlation between \mathcal{A}_t and
 756 $\mathcal{T}_{\overline{S}}$, increasingly so as r_d decreases from large to small scales. Along with the fifth KMH
 757 result at the end of the previous section (that the fluctuation magnitudes of \mathcal{A}_t and $\mathcal{T}_{\overline{S}}$ become
 758 increasingly comparable as r_d decreases), this anti-correlation tendency suggests a tendency
 759 towards $\mathcal{A}_t + \mathcal{T}_{\overline{S}} \approx 0$ at decreasing scales in agreement with the concept of two-point
 760 sweeping introduced in section 3.2. In other words, the sweeping of $|\delta \mathbf{u}|^2$ by the mainly
 761 large scale advection velocity $(\mathbf{u}^+ + \mathbf{u}^-)/2$ becomes increasingly strong with decreasing r_d .

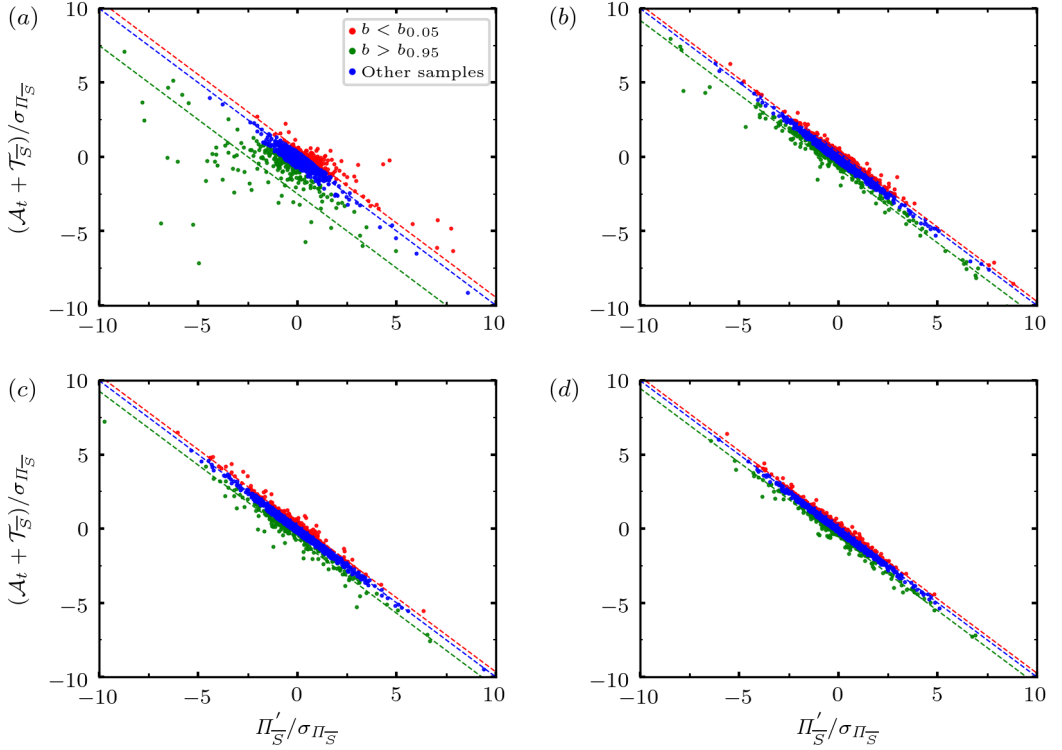


Figure 12: Scatter plots of $\mathcal{A}_t + \mathcal{T}_{\bar{S}}$ and $\Pi'_{\bar{S}}$ at random orientations \mathbf{r} . The residual $-b \equiv \mathcal{A}_t + \mathcal{T}_{\bar{S}} + \Pi'_{\bar{S}}$ and the values $b_{0.05}$ and $b_{0.95}$ are defined analogously as for $\Pi_{\bar{S}_{0.05}}$ and $\Pi_{\bar{S}_{0.95}}$ in the previous figure. The events $b < b_{0.05}$ and $b > b_{0.95}$ are marked in red and green respectively, while the remaining events are marked in blue. The red line marks $\mathcal{A}_t + \mathcal{T}_{\bar{S}} = -\Pi'_{\bar{S}} - \langle b | b < b_{0.05} \rangle$, the green line $\mathcal{A}_t + \mathcal{T}_{\bar{S}} = -\Pi'_{\bar{S}} - \langle b | b > b_{0.95} \rangle$ and the blue line $\mathcal{A}_t + \mathcal{T}_{\bar{S}} = -\Pi'_{\bar{S}}$ (with all terms appropriately normalised with $\sigma_{\Pi_{\bar{S}}}$). $r_d / \langle \lambda \rangle_t = (0.12, 1.45, 3.1, 5.2)$ for (a, b, c, d) and $\langle Re_\lambda \rangle_t = 174$.

762 The scatter plots of \mathcal{A}_t and $\mathcal{T}_{\bar{S}}$ in figure 11 make this local/instantaneous two-point sweeping
 763 tendency with decreasing r_d very evident, but also indicate that significant values of positive
 764 or negative $\Pi_{\bar{S}}$ can cause increasing deviations from $\mathcal{A}_t + \mathcal{T}_{\bar{S}} \approx 0$ as r_d increases. Note
 765 $\mathcal{A}_t + \mathcal{T}_{\bar{S}} + \Pi_{\bar{S}} \approx 0$ as indicated by the correlation coefficients in figure 9 between $\mathcal{A}_t + \mathcal{T}_{\bar{S}}$ and
 766 $-\Pi_{\bar{S}}$ (which exceed 0.95 for $r_d \geq \langle \lambda \rangle_t$ at our Reynolds numbers) and by their overlapping
 767 fluctuation magnitudes in figure 6(a2,b2). The fluctuations of $\Pi_{\bar{S}}$ increase in magnitude as
 768 r_d increases and so do high values of $\Pi_{\bar{S}}$ too. The scatter plots in figure 11 highlight how
 769 the 5% most negative $\Pi_{\bar{S}}$ events (values of $\Pi_{\bar{S}}$ for which the probability that $\Pi_{\bar{S}}$ is smaller
 770 than a negative value $\Pi_{\bar{S}_{0.05}}$ is 0.05) and the 5% most positive $\Pi_{\bar{S}}$ events (values of $\Pi_{\bar{S}}$
 771 for which the probability that $\Pi_{\bar{S}}$ is larger than a positive value $\Pi_{\bar{S}_{0.95}}$ is also 0.05) cause
 772 significant deviations from "perfect sweeping" $\mathcal{A}_t = -\mathcal{T}_{\bar{S}}$, increasingly so for increasing r_d ,
 773 in agreement with $\mathcal{A}_t + \mathcal{T}_{\bar{S}} + \Pi_{\bar{S}} \approx 0$.

774 The scatter plots in figure 12 show that it is only in relatively rare circumstances that
 775 $\mathcal{A}_t + \mathcal{T}_{\bar{S}} + \Pi_{\bar{S}} \approx 0$ is significantly inaccurate for scales $r_d \geq \langle \lambda \rangle_t$. Similarly to NSD
 776 dynamics, $\mathcal{A}_t + \mathcal{T}_{\bar{S}}$ can be viewed as a Lagrangian time-rate of change of $|\delta \mathbf{u}|^2$ moving

777 with $(\mathbf{u}^+ + \mathbf{u}^-)/2$. As more than average $|\delta\mathbf{u}|^2$ is cascaded from larger to smaller scales at a
 778 particular location ($\Pi'_S < 0$), $\mathcal{A}_t + \mathcal{T}_S$ increases; and as more than average $|\delta\mathbf{u}|^2$ is inverse
 779 cascaded from smaller to larger scales ($\Pi'_S > 0$), $\mathcal{A}_t + \mathcal{T}_S$ decreases. Π'_S is to a large extent
 780 determined by $\mathbf{a}_{\Pi'_S}$ which, as we show in appendix C, is a non-local function in space of the
 781 vortex stretching and compression dynamics determining the two-point vorticity difference
 782 $\delta\omega$.

783 A fairly complete way to summarise the details of the balance $\mathcal{A}_t + \mathcal{T}_S + \Pi'_S \approx 0$ at scales
 784 $r_d \geq \langle \lambda \rangle_t$ is by noting that, as r_d decreases towards $\langle \lambda \rangle_t$, (i) the fluctuation magnitude of
 785 \mathcal{T}_S tends to become comparable to that of \mathcal{A}_t while that of Π'_S decreases by comparison,
 786 (ii) the correlation coefficient between \mathcal{A}_t and $-\mathcal{T}_S$ increases towards 0.9, and also (iii) (not
 787 mentioned till now but evident in figure 9) the correlation coefficient between \mathcal{A}_t and $-\Pi'_S$
 788 decreases towards values below 0.2.

789

4.2. Conditional correlations

790 At scales r_d below $\langle \lambda \rangle_t$, the relation $\mathcal{A}_t + \mathcal{T}_S + \Pi'_S \approx 0$ becomes less accurate as the correlation
 791 coefficient between $\mathcal{A}_t + \mathcal{T}_S$ and $-\Pi'_S$ drops from 0.95 to 0.7 with decreasing r_d , reflecting the
 792 increase of correlation between ϵ and $-\Pi'_S$ and the even higher increase towards values close
 793 to 0.5 of the correlation coefficient between \mathcal{D} and Π'_S . This increase of correlation appears
 794 to reflect the impact of relatively rare yet intense local/instantaneous occurrences of interscale
 795 transfer rate as shown in figure 13 where we plot correlations conditional on relatively rare
 796 interscale events where the magnitudes of the spherically-averaged interscale transfer rates
 797 are higher than 95% of all interscale transfer rates of same sign (positive for backward and
 798 negative for forward transfer) in our overall spatio-temporal sample. This impact is highest
 799 at scales smaller than $\langle \lambda \rangle_t$ where the correlation coefficient conditioned on intense forward
 800 or backward interscale transfer rate events of $\pm\Pi'_S$ and either ϵ or \mathcal{D} can be as high as 0.7
 801 ($+\Pi'_S$ in the case of backward events and $-\Pi'_S$ in the case of forward events which causes
 802 significantly higher correlations between $\mathcal{A}_t + \mathcal{T}_S$ and either $-\epsilon$ or \mathcal{D} in the case of backward
 803 events than in the case of forward events as seen in figure 13). However, the impact of
 804 such relatively rare events is also manifest at scales larger than $\langle \lambda \rangle_t$ (see figure 13) where the
 805 conditioned correlation coefficient is significantly higher than the unconditioned one in figure
 806 9. Interestingly, conditioning on these relatively rare events does not change the correlation
 807 coefficients of $\mathcal{A}_t + \mathcal{T}_S$ with $-\Pi'_S$ except at scales r_d smaller than $\langle \lambda \rangle_t$ where, consistently
 808 with the increased conditioned correlations between $-\Pi'_S$ and \mathcal{D} , they are smaller than the
 809 unconditional correlation coefficients of $\mathcal{A}_t + \mathcal{T}_S$ with $-\Pi'_S$, particularly at relatively rare
 810 forward interscale events where this conditional correlation drops to values close to 0.3 at
 811 scales well below $\langle \lambda \rangle_t$.

812 Given that our relatively rare intense interscale transfer rates can be the seat of some
 813 correlation between Π'_S and either $-\epsilon$ or \mathcal{D} particularly for $r_d < \langle \lambda \rangle_t$, and given that
 814 $\mathcal{A}_t + \mathcal{T}_S \approx 0$ is a good approximation at scales smaller than $\langle \lambda \rangle_t$, do we have approximate
 815 two-point sweeping and approximate equilibrium $\Pi'_S \approx \mathcal{D}$ if we condition on relatively
 816 rare forward or backward interscale transfer rate events? In fact the conditional correlations
 817 between \mathcal{A}_t and $-\mathcal{T}_S$ are very high (close to and above 0.95) at all scales (see figure 13), higher
 818 than the corresponding unconditional correlations. However, the conditional averages of \mathcal{A}_t
 819 and $-\mathcal{T}_S$ shown in figure 14 are also significantly different at all scales, implying that these
 820 strong conditional correlations do not actually amount to two-point sweeping at relatively rare
 821 forward and backward events. Furthermore, if we condition on high negative/positive values
 822 of Π'_S , the averages of both \mathcal{A}_t and \mathcal{T}_S are positive/negative (figure 14), even though these
 823 conditional averages do tend to 0 as r_d tends to 0. This has two implications. (i) It implies

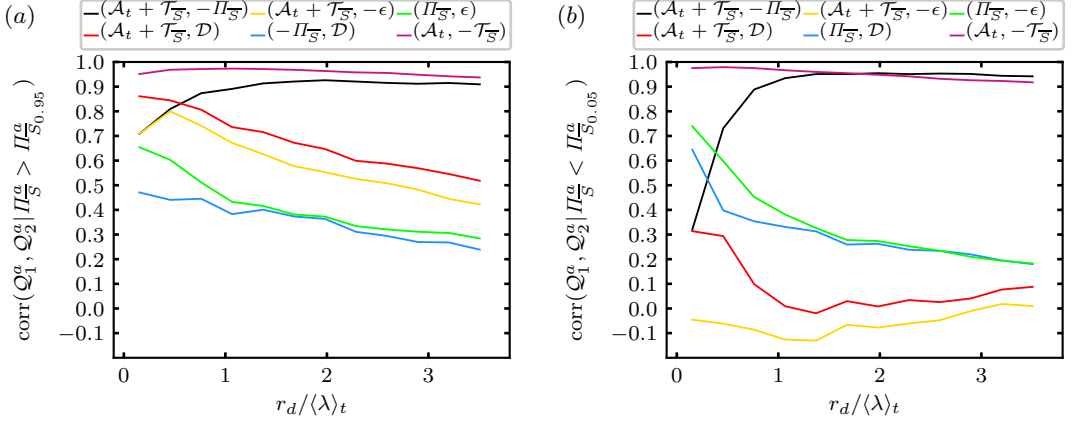


Figure 13: (a) Correlation coefficients among the 5% strongest spherically averaged backward interscale transfer events $\Pi_S^a > \Pi_{S_{0.95}}^a$ for KHMH terms (Q_1^a, Q_2^a) listed on top of the figure. (b) Correlation coefficients among the 5% strongest spherically averaged forward interscale transfer events $\Pi_S^a < \Pi_{S_{0.05}}^a$ for KHMH terms (Q_1^a, Q_2^a) listed on top of the figure. $\langle Re_\lambda \rangle_t = 112$. (Corresponding plots for $\langle Re_\lambda \rangle_t = 174$ are omitted because they are very similar.)

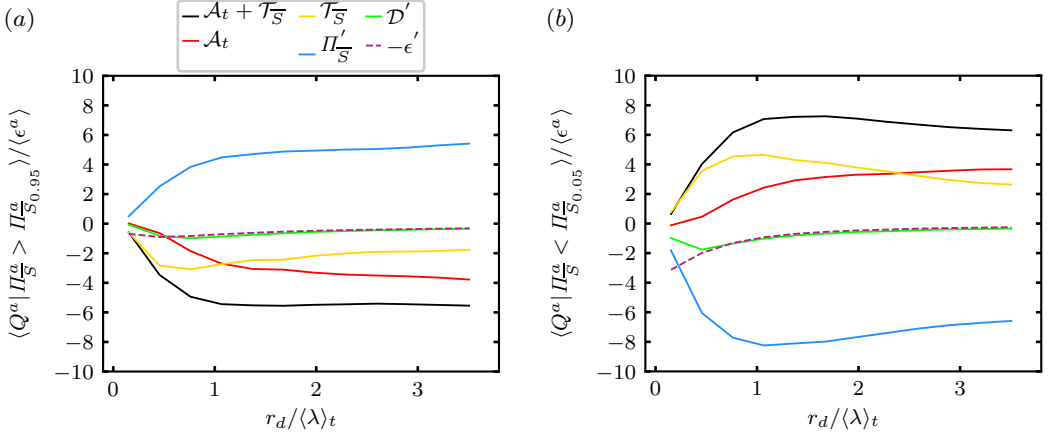


Figure 14: (a) Spatio-temporal averages of KHMH terms Q^a conditioned on the 5% strongest spherically averaged backward (a) and forward (b) interscale transfer events. The KHMH terms are listed above figure (a) and $\langle Re_\lambda \rangle_t = 112$. (Corresponding plots for $\langle Re_\lambda \rangle_t = 174$ are omitted because they are very similar.)

824 that, even though \mathcal{A}_t and $-\mathcal{T}_{\bar{S}}$ are very well correlated at these relatively rare events, $\mathcal{A}_t + \mathcal{T}_{\bar{S}}$
825 fluctuates around a constant C where $C > 0$ if we condition the fluctuations on relatively
826 rare negative $\Pi_{\bar{S}}$ but $C < 0$ if we condition them on relatively rare positive $\Pi_{\bar{S}}$ ($C = 0$ if
827 we do not condition). This amounts to a systematic deviation on the average from two-point
828 sweeping even though the strong correlation between the high magnitude fluctuations of \mathcal{A}_t
829 and $-\mathcal{T}_{\bar{S}}$ point at a tendency towards sweeping which is frustrated by the presence of the
830 comparatively low non-zero local $\Pi_{\bar{S}}$. Given equation (3.29), the presence of this non-zero
831 constant C (clearly non-zero for all scales, and non-zero but tending towards zero as r_d tends

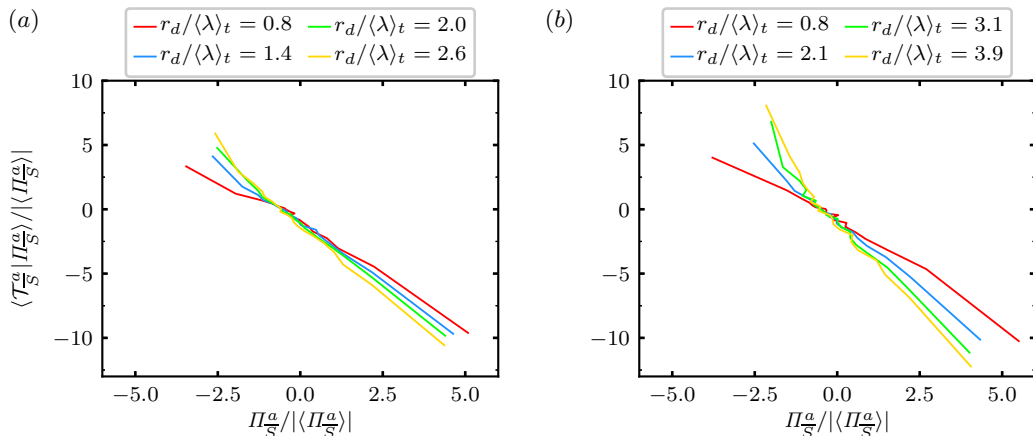


Figure 15: Spatio-temporal averages of \mathcal{T}_S^a across scales r_d conditioned on Π_S^a being within a certain range of Π_S^a values and we consider 20 such ranges of increasing values of Π_S^a : the 5% smallest/most negative Π_S^a , the 5% to 10% smallest/most negative Π_S^a values and so on until the 5% largest/most positive Π_S^a values. (a) $\langle Re \rangle_t = 112$, (b) $\langle Re \rangle_t = 174$.

832 to 0 well below $\langle \lambda \rangle_t$) means that the equilibrium $\Pi_{\bar{S}} \approx \mathcal{D}$ for scales smaller than $\langle \lambda \rangle_t$ does
 833 not hold either, even at scales smaller than $\langle \lambda \rangle_t$ where the conditional correlation between
 834 $\Pi_{\bar{S}}$ and \mathcal{D} is significant. In fact, figure 14 shows that the conditional averages of $\Pi_{\bar{S}}'$ are much
 835 larger than those of both \mathcal{D}' and $-\epsilon'$; they are much closer to those of $\mathcal{A}_t + \mathcal{T}_{\bar{S}}$.

836 (ii) The second implication of the conditional signs of $\mathcal{T}_{\bar{S}}$ is the existence of a relation
 837 between conditional average of solenoidal interspace transfer rate $\mathcal{T}_{\bar{S}}$ and the solenoidal
 838 interspace transfer rate $\Pi_{\bar{S}}$ on which the average is conditioned: when one is positive/negative
 839 the other is negative/positive, and we also find that their absolute magnitudes increase together
 840 (see figure 15). This is an observation which may prove important in the future for both subgrid
 841 scale modeling and the detailed study of the very smallest scales of turbulence fluctuations.

842 In conclusion, $\Pi_{\bar{S}}$ does not fluctuate with neither $-\epsilon$ nor \mathcal{D} . Instead, $\Pi_{\bar{S}}$ and $\mathcal{A}_t + \mathcal{T}_{\bar{S}}$
 843 fluctuate together at all scales, in particular scales larger than $\langle \lambda \rangle_t$, and even at relatively rare
 844 interscale transfer events. At scales smaller than $\langle \lambda \rangle_t$, we have a general tendency towards
 845 two-point sweeping if we do not condition on particular events. At our relatively rare interscale
 846 transfer events this correlation tendency (now conditional) is in fact amplified but there is
 847 nevertheless a systematic average deviation from two-point sweeping consistent with the
 848 absence of equilibrium $\Pi_{\bar{S}} \approx \mathcal{D}$ at these events. Finally, a relation exists between interspace
 849 and interscale transfer rates because the average interspace transfer rate conditioned on
 850 positive/negative values of interscale transfer rate is negative/positive. It must be stressed,
 851 however, that this relation does not imply an anticorrelation between interscale and interspace
 852 transport rates. The unconditioned correlation coefficients between $-\Pi_{\bar{S}}$ and $\mathcal{T}_{\bar{S}}$ are around
 853 0.2 (see figure 9), and we checked that this 0.2 correlation does not change significantly if
 854 we condition on relatively rare intense occurrences of interscale transfer rate.

855 5. Inhomogeneity contribution to interscale transfer

856 5.1. Average values and PDFs

857 The decomposition $\Pi = \Pi_{\overline{I}} + \Pi_{\overline{S}}$ helped us distinguish between the solenoidal vortex
 858 stretching/compression and the pressure-related aspects of the interscale transfer. As recently
 859 shown by Alves Portela *et al.* (2020), the interscale transfer rate Π can also be decomposed
 860 in a way which brings out the fact that it has a direct inhomogeneity contribution to it. This
 861 last part of the present study is an examination of the decomposition introduced by Alves
 862 Portela *et al.* (2020) which is $\Pi = \Pi_I + \Pi_H$ where

$$863 \quad \Pi_I = \frac{1}{2} \delta u_i \frac{\partial}{\partial x_i} (u_k^+ u_k^+ - u_k^- u_k^-), \quad (5.1)$$

$$864 \quad \Pi_H = -2 \delta u_i \frac{\partial}{\partial r_i} (u_k^- u_k^+). \quad (5.2)$$

866 Π_I can be locally/instantaneously non-zero only in the presence of a local/instantaneous
 867 inhomogeneity. However, it averages to zero, i.e. $\langle \Pi_I \rangle = 0$, in periodic/statistically homoge-
 868 neous turbulence. Note that $\Pi = \Pi_I + \Pi_H = 0$ at $\mathbf{r} = \mathbf{0}$. With \mathbf{r} -orientation-averaging, the
 869 decomposition $\Pi^a = \Pi_I^a + \Pi_H^a$ is unique in the sense that any potentially suitable (e.g. such
 870 that it equals 0 at $\mathbf{r} = \mathbf{0}$) \mathbf{x} -gradient term added to Π_I vanishes after \mathbf{r} -orientation-averaging
 871 (see Alves Portela *et al.* (2020)).

872 An equivalent expression for Π_I which immediately reveals where the decomposition
 873 $\Pi = \Pi_I + \Pi_H$ comes from is $\Pi_I = \delta u_i \frac{\partial}{\partial r_i} (u_k^+ u_k^+ + u_k^- u_k^-)$. Given that the total interscale
 874 transfer rate is $\Pi = \delta u_i \frac{\partial}{\partial r_i} (\delta u_k \delta u_k)$, the Π_I part of the interscale transfer concerns the
 875 transferred energy differences coming mostly from differences between velocity amplitudes,
 876 i.e. local/instantaneous inhomogeneities of ‘‘turbulence intensity’’ in the flow; the Π_H
 877 part of the interscale transfer concerns transferred energy differences coming mostly from
 878 differences between velocity orientations. Consistently with its link to local/instantaneous
 879 non-homogeneity, Π_I can be written in the form ((5.1)) making it clear that Π_I is zero where
 880 and when fluctuating velocity magnitudes are locally uniform.

881 In comparing the decompositions $\Pi = \Pi_{\overline{S}} + \Pi_{\overline{I}}$ and $\Pi = \Pi_I + \Pi_H$, it is worth noting that
 882 $\Pi_I = \Pi_{\overline{I}}$ given that $\Pi_{\overline{S}} = 0$ from its centroid gradient form (see equation (5.1)). It therefore
 883 follows that

$$884 \quad \Pi_{\overline{S}} = \Pi_{H_{\overline{S}}}, \quad (5.3)$$

$$885 \quad \Pi_{\overline{I}} = \Pi_I + \Pi_{H_{\overline{I}}}. \quad (5.4)$$

887 The inhomogeneity-based interscale transfer rate influences only the irrotational part of the
 888 total interscale transfer rate whereas Π_H influences both the irrotational and the solenoidal
 889 parts. As $\langle \Pi_I \rangle = 0$ and $\langle \Pi_{\overline{I}} \rangle = 0$, it follows that $\langle \Pi_{H_{\overline{I}}} \rangle = 0$. More to the point, $\langle \Pi_{\overline{S}} \rangle$ equals
 890 $\langle \Pi_{H_{\overline{S}}} \rangle$ and so equation (3.28) reduces to

$$891 \quad \langle \Pi \rangle = \langle \Pi_{H_{\overline{S}}} \rangle = \langle \mathcal{D}_{r,v} \rangle - \langle \epsilon \rangle + \langle \mathcal{I} \rangle. \quad (5.5)$$

892 The part of the interscale transfer rate which is present in the average interscale trans-
 893 fer/cascade dynamics is in fact $\Pi_{H_{\overline{S}}}$.

894 Given that the average interscale transfer is controlled by $\Pi_{H_{\overline{S}}} = \Pi_{\overline{S}}$, it is worth asking
 895 whether the well-known negative skewness of the PDF of Π^a (e.g. see Yasuda & Vassilicos
 896 (2018) and references therein) is also present in the PDF of $\Pi_{\overline{S}}$ or/and whether it is spread
 897 across different terms of our two interscale transfer rate decompositions. In figure 16 we plot
 898 the PDFs of Π^a and of the different \mathbf{r} -orientation-averaged terms in the decompositions of
 899 Π that we use. It is clear that the PDFs of Π and $\Pi_{\overline{S}}$ are nearly identical whilst the PDFs

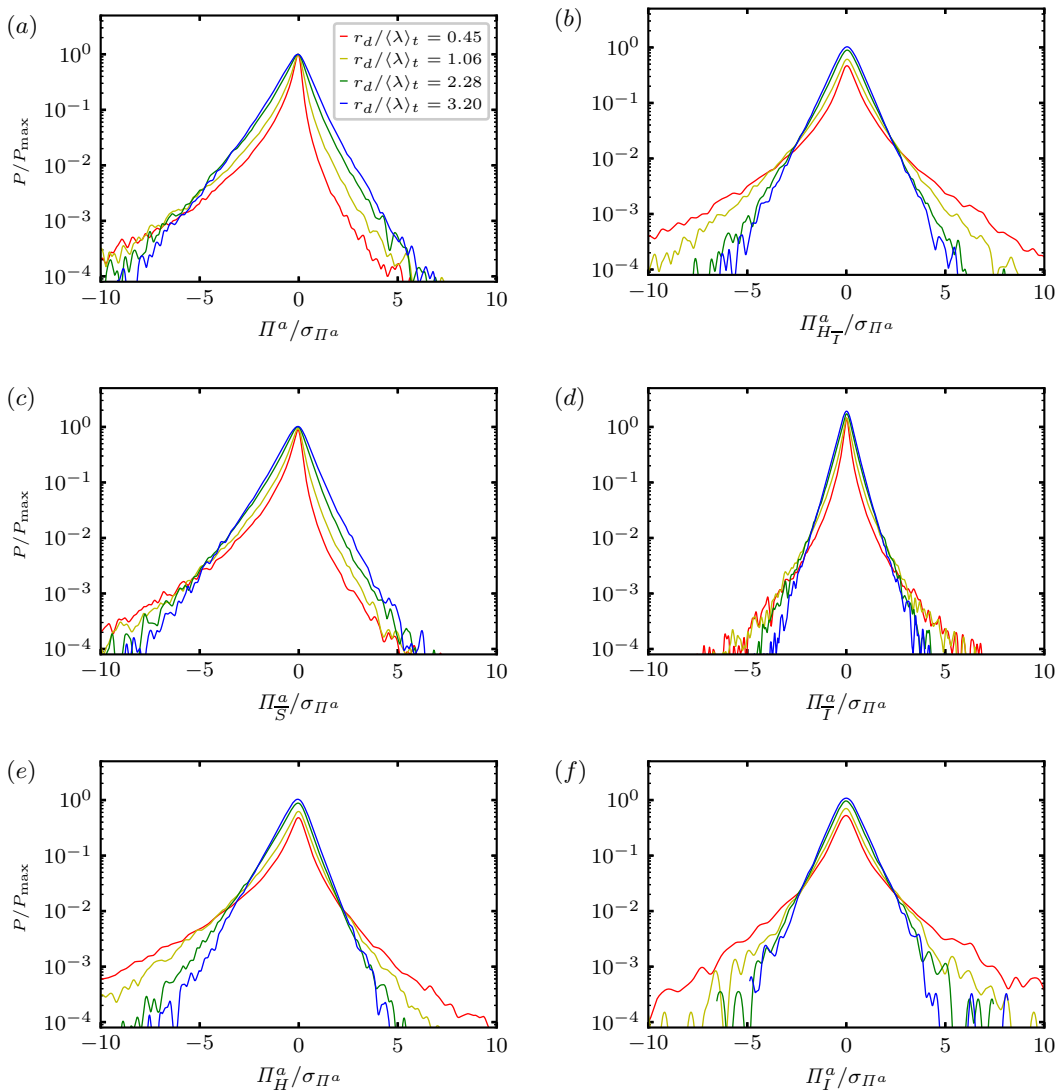


Figure 16: (a, b, c, d, e, f) PDFs of Π decompositions ($\Pi, \Pi_{H_T}, \Pi_S, \Pi_T, \Pi_H, \Pi_I$) at $\langle Re\lambda \rangle_t = 112$. σ_{Π^a} denotes the standard deviation of Π^a and P_{\max} denotes the maximum value of the PDF of Π^a . The inhomogeneity and homogeneity interscale transfer rates Π_I and Π_H are defined in equations (5.1)-(5.2) and the irrotational part of the homogeneity interscale transfer rate Π_{H_T} in equation (5.4).

900 of Π_H are different though also negatively skewed. The PDFs of Π_{H_T} , Π_T and Π_I are not
 901 significantly skewed. In figure 17 we plot the skewness factors of the various interscale transfer
 902 terms as well as some other KMH terms. The inhomogeneity interscale transfer Π_I has
 903 close to zero skewness across scales. Both Π_S and Π_H are negatively skewed, the former
 904 more so than the latter. Given equations (5.3)-(5.4) and $\Pi_H = \Pi_S + \Pi_{H_T}$, this difference
 905 in skewness factors is due to the irrotational part of Π_H which is not significantly skewed
 906 and reduces the skewness of Π_H relative to that of Π_S . All in all, the skewness towards

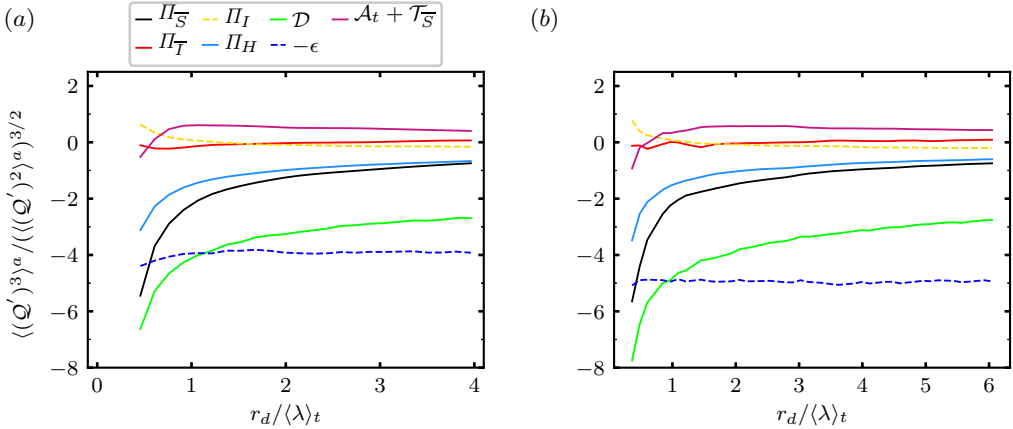


Figure 17: Skewness factors for KHMH terms Q listed on top of (a): (a) $\langle Re_\lambda \rangle_t = 112$,
(b) $\langle Re_\lambda \rangle_t = 174$.

907 forward rather than inverse interscale transfers is present in its homogeneous and solenoidal
908 components but is absent in its non-homogeneous and irrotational parts.

909 Figure 17 also shows that $\mathcal{A}_t + \mathcal{T}_{\overline{S}}$ is slightly positively skewed with flatness factors of
910 approximately 0.5 at scales $r_d \geq \langle \lambda \rangle_t$ and close to 0 or below at scales below $\langle \lambda \rangle_t$. The
911 skewness factor of $-\Pi_{\overline{S}}$ with which $\mathcal{A}_t + \mathcal{T}_{\overline{S}}$ is very well correlated (as we have seen in the
912 previous section) is about the same at scales close to the integral scale but steadily increases
913 to values well above 0.5 as r decreases, reaching nearly 6.0 at scales close to $0.5\langle \lambda \rangle_t$. This is
914 a concrete illustration of the fact already mentioned earlier in this paper that $\mathcal{A}_t + \mathcal{T}_{\overline{S}} \approx -\Pi_{\overline{S}}$
915 is a very good approximation for most locations and most times but not all. Given the very
916 significantly increased correlation/anti-correlation of $\Pi_{\overline{S}}$ with both \mathcal{D} and ϵ at relatively
917 intense forward/inverse interscale transfer events and with decreasing scale r_d , it is natural
918 to expect the skewness factor of $\Pi_{\overline{S}}$ to veer towards the skewness factors of \mathcal{D} and $-\epsilon$ which,
919 as can be seen in figure 17, are highly negative with values between -3.0 and -7.0 .

920

5.2. Correlations

921 We now consider the local/instantaneous relations between the various interscale transfer
922 terms in terms of correlation coefficients plotted in figure 18a. First, note the very strong
923 correlation between Π and $\Pi_{\overline{S}}$ and the moderate correlation between Π and $\Pi_{\overline{T}}$. Even though
924 Π and $\Pi_{\overline{S}}$ are highly correlated, we cannot ignore $\Pi_{\overline{T}}$ and cannot write $\Pi \approx \Pi_{\overline{S}}$. As seen
925 earlier in the paper, we cannot ignore $\Pi_{\overline{T}}$ because it is the part of the interscale transfer
926 which balances the pressure term, but we have also seen that the fluctuation magnitude of
927 $\Pi_{\overline{S}}$ is significantly higher than the fluctuation magnitude of $\Pi_{\overline{T}}$. However, even if smaller, the
928 fluctuation magnitude of $\Pi_{\overline{T}}$ is not negligible. There is no correlation between $\Pi_{\overline{S}}$ and $\Pi_{\overline{T}}$ (see
929 figure 18b), and so Π correlates with both $\Pi_{\overline{S}}$ (strongly) and $\Pi_{\overline{T}}$ (moderately) for different
930 independent reasons. Π feels the influence of solenoidal vortex stretching/compression via
931 $\Pi_{\overline{S}}$ and the influence of pressure fluctuations via $\Pi_{\overline{T}}$, the former influencing Π more than the
932 latter.

933 Figure 18a also shows significantly smaller correlations between Π and Π_H than between
934 Π and $\Pi_{\overline{S}}$. This must be due to a decorrelating effect of $\Pi_{H\overline{T}}$ as $\Pi_H = \Pi_{\overline{S}} + \Pi_{H\overline{T}}$. The
935 correlations between Π and Π_I are even smaller at the smaller scales but at integral size
936 scales these correlations are equal to those between Π and Π_H (figure 18a).

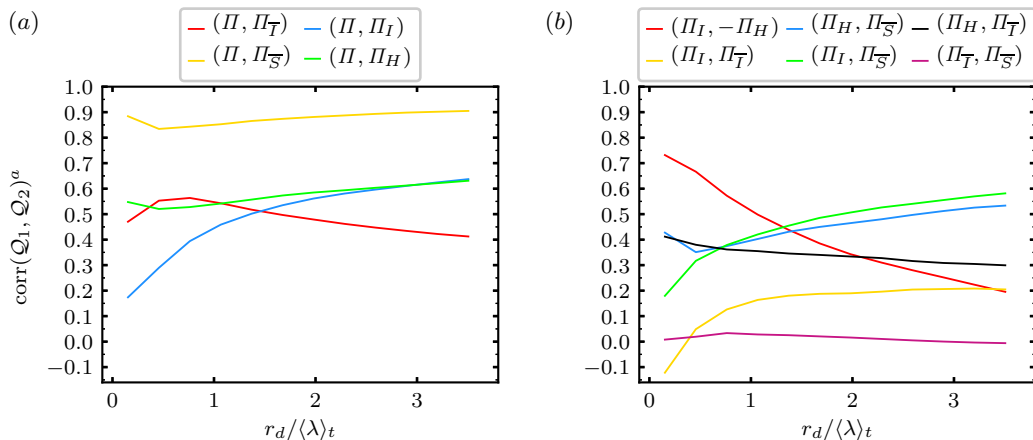


Figure 18: Correlation coefficients between various Π decompositions (Q_1, Q_2) listed on top of the figures at $\langle Re_\lambda \rangle_t = 112$. (Corresponding plots for $\langle Re_\lambda \rangle_t = 174$ are omitted because they are very similar.)

937 Figure 18b reveals a strong anti-correlation between Π_I and Π_H at the small scales and
 938 a weak one at the large scales. As the scales decrease, the interscale transfers of fluctuating
 939 velocity differences caused by local/instantaneous non-homogeneities and the interscale
 940 transfers of fluctuating velocity differences caused by orientation differences get progressively
 941 more anti-correlated. This anti-correlation tendency results in Π_H and Π_I having larger
 942 fluctuation magnitudes than Π at smaller scales, in particular scales smaller than $\langle \lambda \rangle_t$ (verified
 943 with our DNS data but not shown here for economy of space).

944 The other significant correlations revealed in figure 18b are those between Π_H and Π_S and
 945 those between Π_I and Π_S , particularly as r_d increases from around/below $\langle \lambda \rangle_t$ to the integral
 946 length scale. These correlations relate to the very strong correlations between Π and Π_S but
 947 are weaker. One can imagine that Π_S correlates with Π_H sometimes and with Π_I some other
 948 times, but not too often with both given that Π_I and Π_H tend to be anti-correlated, and that
 949 this happens in a way subjected to a continuously strong correlation between $\Pi = \Pi_H + \Pi_I$
 950 and Π_S .

951 We finally consider in figure 19 the average contributions of the various Π -decomposition
 952 terms conditional on relatively rare intense Π -events. We calculate averages conditioned on
 953 5% most negative (forward transfer) Π_S events (values of Π_S for which the probability that
 954 Π_S is smaller than a negative value $\Pi_{S_{0.05}}$ is 0.05) and on 5% most positive Π_S (inverse
 955 transfer) events (values of Π_S for which the probability that Π_S is larger than a positive value
 956 $\Pi_{S_{0.95}}$ is also 0.05). All these averages tend to 0 as r_d tends to 0 below $\langle \lambda \rangle_t$. The largest such
 957 conditional averages are those of Π' followed by those of Π'_S . This is the forward-skewed part
 958 of the interscale transfer (in terms of PDFs) and it is dominant at both forward and backward
 959 intense interscale transfer events. The weakest such conditional averages are those of Π'_T for
 960 all r_d and both forward and inverse extreme interscale transfer events. This is consistent with
 961 our observation in section 3.4 that the unconditional fluctuation magnitude of Π'_T is smaller
 962 than the unconditional fluctuation magnitudes of Π followed by those of Π_S .

963 The most interesting point to notice in figure 19, however, is the difference between
 964 conditional averages of Π'_H and Π'_I when conditioned on intense forward or intense inverse
 965 interscale transfer events. Whilst the conditional averages of these two quantities are about
 966 the same at intense inverse events, they differ substantially at forward transfer events where

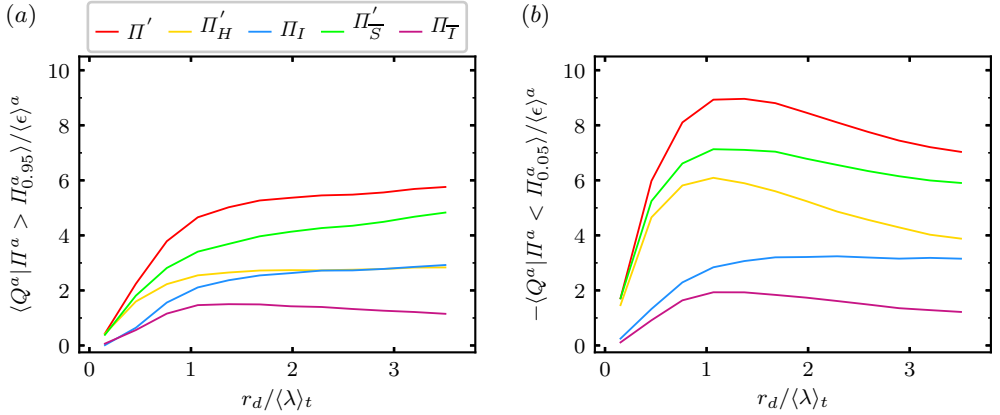


Figure 19: Average values of Π decompositions conditioned on (a) intense backward events, (b) intense forward events at $\langle Re_\lambda \rangle_t = 112$. The top of (a) lists the Π decompositions. (Corresponding plots for $\langle Re_\lambda \rangle_t = 174$ are omitted because they are very similar.)

967 the conditional average of $-\Pi'_H$ is substantially higher than the conditional average of $-\Pi_I$
 968 except close to the integral length-scale.

969 6. Conclusions

970 The balance between space-time-averaged interscale energy transfer rate on the one hand
 971 and space-time-averaged viscous diffusion, turbulence dissipation rate and power input on
 972 the other does not represent in any way the actual energy transfer dynamics in statistically
 973 stationary homogeneous/periodic turbulence. In this paper we have studied the fluctuations of
 974 two-point acceleration terms in the NSD equation and their relation to the various terms of the
 975 KMH equation. We now give a point-by-point summary of our results on KMH dynamics
 976 (A), conditional KMH dynamics (B) and inhomogeneity and homogeneity contributions
 977 to the interscale transfer rate (C).

978 A1. The various corresponding terms in the NSD and KMH equations behave similarly
 979 relative to each other because the two-point velocity difference has a similar tendency of
 980 alignment with each one of the acceleration terms of the NSD equation (see figure 8).

981 A2. The terms in the two-point energy balance which fluctuate with the highest magnitudes
 982 are \mathcal{A}'_c followed closely by the time-derivative term \mathcal{A}_t and the solenoidal interspace transfer
 983 rate \mathcal{T}'_S . The fluctuation intensity of $\mathcal{A}_t + \mathcal{T}'_S$ is much reduced by comparison to both these
 984 terms (two-point sweeping) and is comparable to the fluctuation intensity of the solenoidal
 985 interscale transfer rate. The solenoidal interscale transfer rate, which averages according
 986 to equation (3.28), does not fluctuate with viscous diffusion and/or turbulence dissipation
 987 with which it is negligibly correlated at scales larger than $\langle \lambda \rangle_t$ and rather weakly correlated
 988 at scales smaller than $\langle \lambda \rangle_t$. Its fluctuation magnitude is also significantly larger than that
 989 of $\mathcal{D}_{r,v}$, $-\epsilon$ and \mathcal{I} at all scales (see figure 6 for KMH magnitude results). Instead, the
 990 solenoidal interscale transfer rate fluctuates with $\mathcal{A}_t + \mathcal{T}'_S$ with which it is extremely well
 991 correlated at length scales larger than $\langle \lambda \rangle_t$ and very significantly correlated at length scales
 992 smaller than $\langle \lambda \rangle_t$ (see KMH correlation results in figure 9).

993 A3. In fact, for scales larger than $\langle \lambda \rangle_t$, the relation

$$994 \quad \mathcal{A}_t + \mathcal{T}_{\bar{S}} + \Pi'_{\bar{S}} \approx 0, \quad (6.1)$$

996 is a good approximation for most times and most locations in the flow. $\mathcal{A}_t + \mathcal{T}_{\bar{S}}$ can be viewed
 997 as a Lagrangian time-rate of change of $|\delta \mathbf{u}|^2$ moving with $(\mathbf{u}^+ + \mathbf{u}^-)/2$. As more than average
 998 $|\delta \mathbf{u}|^2$ is cascaded from larger to smaller scales at a particular location ($\Pi'_{\bar{S}} < 0$), $\mathcal{A}_t + \mathcal{T}_{\bar{S}}$
 999 increases; and as more than average $|\delta \mathbf{u}|^2$ is inverse cascaded from smaller to larger scales
 1000 ($\Pi'_{\bar{S}} > 0$), $\mathcal{A}_t + \mathcal{T}_{\bar{S}}$ decreases (see section 4.1). The relatively rare space-time events which do
 1001 not comply with this relation are responsible for the different skewness factors of the PDFs
 1002 of $\mathcal{A}_t + \mathcal{T}_{\bar{S}}$ (small, mostly positive, skewness factor) and of $\Pi'_{\bar{S}}$ (negative skewness factor
 1003 reaching increasingly large negative values with decreasing scale).

1004 A4. As the length scale (i.e. two point separation length) decreases, the correlation between
 1005 \mathcal{A}_t and $-\mathcal{T}_{\bar{S}}$ increases and so do their fluctuation magnitudes relative to the fluctuation
 1006 magnitude of $\Pi'_{\bar{S}}$ which reaches to be an order of magnitude smaller by comparison. In
 1007 this limit, the correlation between \mathcal{A}_t and $-\Pi'_{\bar{S}}$ decreases. At length scales smaller than
 1008 $\langle \lambda \rangle_t$ the correlation between \mathcal{A}_t and $-\mathcal{T}_{\bar{S}}$ is extremely good indicating a tendency towards
 1009 two-point sweeping. However, the correlation between $\mathcal{A}_t + \mathcal{T}_{\bar{S}}$ and $\Pi'_{\bar{S}}$ remains strong even
 1010 if reduced from its near perfect values at length scales larger than $\langle \lambda \rangle_t$ and there remains
 1011 a small difference of fluctuation magnitudes between \mathcal{A}_t and $\mathcal{T}_{\bar{S}}$ which is mostly related to
 1012 the small fluctuation magnitude of $\Pi'_{\bar{S}}$. At the other end of the length scale range, i.e. as the
 1013 length scale tends towards the integral scale and larger, the fluctuation magnitudes of $\mathcal{T}_{\bar{S}}$ and
 1014 $\Pi'_{\bar{S}}$ tend to become the same (the scatter plots in figures 11-12 evidence these behaviours).

1015 A5. The irrotational part of the interscale transfer rate has zero spatio-temporal average but
 1016 is exactly equal to the irrotational part of the interspace transfer rate and half the two-point
 1017 pressure work term in the KMHM equation. A complete dynamic picture of the interscale
 1018 transfer rate needs to also take this into account, even though the fluctuation magnitudes
 1019 of these irrotational terms are smaller than the ones of the terms discussed in the previous
 1020 paragraph. In fact, the exact relation $\Pi_{\bar{T}} = \mathcal{T}_{\bar{T}} = \frac{1}{2} \mathcal{T}_p$ explains the significant correlation
 1021 between interscale transfer rate Π and \mathcal{T}_p reported by Yasuda & Vassilicos (2018).

1022 B1. The increase towards small correlations at length scales below $\langle \lambda \rangle_t$ between $\Pi_{\bar{S}}$ and
 1023 both $\mathcal{D}_{r,v}$ and $-\epsilon$ is accountable to the significant correlations between these terms at these
 1024 viscous scales when conditioned on relatively rare intense $\Pi_{\bar{S}}$ events, both forward cascading
 1025 events with negative values of $\Pi_{\bar{S}}$ of high magnitude and backward cascading events with
 1026 positive values of $\Pi_{\bar{S}}$ of high magnitude. The choice of $\Pi_{\bar{S}}$ to identify relatively rare intense
 1027 events is predicated on the fact that the PDFs of $\Pi_{\bar{S}}$ are negatively skewed similarly to the
 1028 PDFs of Π , whereas the PDFs of $\Pi_{\bar{T}}$ are not (the interscale transfer PDFs are given in figure
 1029 16). The solenoidal part of the interscale transfer rate derives from the integrated two-point
 1030 vorticity equation and includes non-local vortex stretching/compression effects at all scales
 1031 whereas the irrotational part of the interscale transfer rate derives from the integrated Poisson
 1032 equation for two-point pressure fluctuations (see appendix C for mathematical details).

1033 B2. At these relatively rare intense interscale transfer rate events, the tendency for two-
 1034 point sweeping may appear increased because of the extremely good conditional correlation
 1035 between \mathcal{A}_t and $-\mathcal{T}_{\bar{S}}$ at all length-scales, however \mathcal{A}_t and $-\mathcal{T}_{\bar{S}}$ have also very significantly
 1036 different average values given the high absolute values of $\Pi_{\bar{S}}$ at these relatively rare interscale
 1037 transfer events (see figures 13-14). This implies that there is neither local/instantaneous
 1038 sweeping nor local/instantaneous balance between $\Pi_{\bar{S}}$ and \mathcal{D} or $\Pi_{\bar{S}}$ and $-\epsilon$ at these relatively
 1039 rare intense events, a conclusion confirmed by the observation that the conditional averages

1040 and the conditional fluctuation magnitudes of $\Pi_{\bar{S}}$ are much higher than those of \mathcal{D} and $-\epsilon$
 1041 in absolute values.

1042 B3. Another property of these relatively rare intense solenoidal interscale transfer rate
 1043 events is that the conditional averages of solenoidal interscale and interspace transfer rates
 1044 have opposite signs when sampling on these events (see figure 15). There is therefore a
 1045 relation between them which may however be concealed by the fact that the fluctuation
 1046 magnitudes of the interspace transport rate are higher than those of the interscale transfer
 1047 rate.

1048 C1. We have also considered the decomposition into homogeneous and inhomogeneous
 1049 interscale transfer rates recently introduced by Alves Portela *et al.* (2020) (see equations (5.1)-
 1050 (5.2)) and have studied their fluctuations in statistically stationary homogeneous turbulence.
 1051 The PDFs of the homogeneous interscale transfer rate are skewed towards forward cascade
 1052 events whereas the PDFs of the inhomogeneous interscale transfer rate are not significantly
 1053 skewed. However, the skewness factors of the PDFs of the homogeneous interscale transfer
 1054 rate are not as high as those of both the full and the solenoidal interscale transfer rates.
 1055 Relating to this, Π is highly correlated with $\Pi_{\bar{S}}$ more than with $\Pi_{\bar{T}}$, Π_H and Π_I with all of
 1056 which Π is, nevertheless, significantly correlated.

1057 C2. There is an increasing correlation between Π_I and $-\Pi_H$ as the length-scale decreases,
 1058 in particular below $\langle \lambda \rangle_t$ where it reaches values above 0.6 (see figure 18). The interscale
 1059 transfer of velocity difference energy caused by local inhomogeneities in fluctuating velocity
 1060 magnitudes tends to cancel the interscale transfer of fluctuating velocity difference energy
 1061 caused by misalignments between the two neighboring fluctuating velocities, in particular at
 1062 length scales below $\langle \lambda \rangle_t$. As a result, the fluctuation magnitudes of Π are smaller than those
 1063 of both Π_I and $-\Pi_H$.

1064 C3. Finally, the decomposition $\Pi = \Pi_I + \Pi_H$ can be used to physically distinguish between
 1065 intense forward and intense inverse interscale transfer events. The averages of Π'_H and Π_I
 1066 when conditioned on intense inverse interscale transfer events are about the same, but they
 1067 differ substantially when conditioned on intense forward interscale transfer events where the
 1068 conditional average of $-\Pi'_H$ is substantially higher than the conditional average of $-\Pi_I$ except
 1069 close to the integral length-scale (see figure 19).

1070 Future subgrid scale models for Large Eddy Simulations (LES) which are dynamic
 1071 reduced order approaches to turbulent flows and their fluctuating large scales cannot rely
 1072 on average cascade phenomenology describing spatio-temporal averages and should benefit
 1073 from detailed descriptions of the fluctuating dynamics of interscale and interspace energy
 1074 transfers such as the one presented in this paper. Whilst LES models based on local
 1075 equilibrium such as the Smagorinsky model can reproduce structure function exponents and
 1076 correlations between velocity increments and subgrid-scale energy transfers as shown by
 1077 Linkmann *et al.* (2018), Dairay *et al.* (2017) have found that the Smagorinsky model is unable
 1078 to suppress small-scale spurious oscillations arising from numerical errors. Furthermore,
 1079 the recent review by Moser *et al.* (2021) makes it clear that the need for new subgrid models
 1080 which can faithfully operate with coarse resolutions remains unanswered. The results in the
 1081 present paper suggest that LES models based on local equilibrium (e.g. the Smagorinsky
 1082 model) cannot be fully suitable for calculating fluctuations in subgrid stresses, a weakness
 1083 which may become increasingly evident with coarser resolution. On the other hand, the
 1084 good correlations between subgrid stresses from similarity models (Bardina *et al.* 1980;
 1085 Cimarelli *et al.* 2019) and subgrid stresses from DNS suggest that these models might indeed
 1086 approximate (unawarely) at least some of the cascade dynamics reported in this paper, for
 1087 example the fact that $\mathcal{A}_t + \mathcal{T}_{\bar{S}} + \Pi'_{\bar{S}} \approx 0$ holds in most of the flow most of the time. This
 1088 relation incorporates both forward and backward interscale transfers, yet a recent work by

1089 Vela-Martín (2022) argues that backscatter represents spatial fluxes and can therefore be
 1090 ignored. It is not yet clear how such a claim can be understood in the context of the present
 1091 paper’s results. Some new questions are therefore now raised concerning LES subgrid stress
 1092 modeling which also need to be addressed in future work.

1093

1094 **Acknowledgements.** We thank Professor S. Goto for allowing us to use his parallelised pseudo-spectral
 1095 DNS code for periodic turbulence.

1096 **Funding.** HSL and JCV acknowledge support from EPSRC award number EP/L016230/1. JCV also
 1097 acknowledges the Chair of Excellence CoPreFlo funded by I-SITE-ULNE (grant no. R-TALENT-19-001-
 1098 VASSILICOS); MEL (grant no. CONVENTION-219-ESR-06) and Region Hauts de France (grant no.
 1099 20003862).

1100 **Declaration of Interests.** The authors report no conflict of interest.

1101 Appendix A. The Helmholtz decomposition in Fourier space

1102 In this appendix we list the Helmholtz decomposition for periodic fields and note how this
 1103 decomposition relates to the more general solution to the Helmholtz decomposition in the
 1104 case of incompressible fields and fields which can be written as gradients of scalar fields.

1105 Let $\mathbf{q}(\mathbf{x}, t)$ be a periodic, twice continuously differentiable 3D vector field with the
 1106 Helmholtz decomposition $\mathbf{q}(\mathbf{x}, t) = \mathbf{q}_I(\mathbf{x}, t) + \mathbf{q}_S(\mathbf{x}, t)$, where $\mathbf{q}_I(\mathbf{x}, t) = -\nabla_x \phi(\mathbf{x}, t)$,
 1107 $\mathbf{q}_S(\mathbf{x}, t) = \nabla_x \times \mathbf{B}(\mathbf{x}, t)$. The scalar and vector potentials ϕ and \mathbf{B} are unique within constants
 1108 when $\nabla_x \cdot \mathbf{q}$ and $\nabla_x \times \mathbf{q}$ are known in the domain and \mathbf{q} is known at the boundary (Bhatia
 1109 *et al.* 2013). $\mathbf{q}(\mathbf{x}, t)$ has the Fourier representation $\widehat{\mathbf{q}}(\mathbf{k}, t)$, which can be decomposed into a
 1110 component parallel to \mathbf{k} (the longitudinal $\widehat{\mathbf{q}}^L$) and transverse to \mathbf{k} (the transverse $\widehat{\mathbf{q}}^T$)

$$1111 \quad \widehat{\mathbf{q}}^L(\mathbf{k}, t) = \frac{\mathbf{k}[\widehat{\mathbf{q}}(\mathbf{k}, t) \cdot \mathbf{k}]}{k^2}, \quad \widehat{\mathbf{q}}^T(\mathbf{k}, t) = \widehat{\mathbf{q}}(\mathbf{k}, t) - \widehat{\mathbf{q}}^L(\mathbf{k}, t). \quad (\text{A } 1)$$

1112 It can be easily shown (see e.g. Stewart (2012)) that the irrotational part of \mathbf{q} equals its
 1113 longitudinal part $\mathbf{q}_I = \mathbf{q}^L$ and that the solenoidal part of \mathbf{q} equals its transverse part $\mathbf{q}_S = \mathbf{q}^T$.
 1114 Hence, (A 1) provides the Fourier representation of the Helmholtz decomposition of \mathbf{q} .

1115 The Helmholtz decomposition can also be written for very general boundary conditions
 1116 as (Sprössig 2010)

$$1117 \quad \mathbf{q}_{IV}(\mathbf{x}, t) = \frac{1}{4\pi} \int_V d\mathbf{y} \frac{\mathbf{x} - \mathbf{y}}{|\mathbf{x} - \mathbf{y}|^3} [\nabla_y \cdot \mathbf{q}(\mathbf{y}, t)], \quad (\text{A } 2)$$

$$1118 \quad \mathbf{q}_{IB}(\mathbf{x}, t) = -\frac{1}{4\pi} \int_S dS_y \frac{\mathbf{x} - \mathbf{y}}{|\mathbf{x} - \mathbf{y}|^3} [\widehat{\mathbf{n}}_y \cdot \mathbf{q}(\mathbf{y}, t)], \quad (\text{A } 3)$$

$$1119 \quad \mathbf{q}_{SV}(\mathbf{x}, t) = -\frac{1}{4\pi} \int_V d\mathbf{y} \frac{\mathbf{x} - \mathbf{y}}{|\mathbf{x} - \mathbf{y}|^3} \times [\nabla_y \times \mathbf{q}(\mathbf{y}, t)], \quad (\text{A } 4)$$

$$1120 \quad \mathbf{q}_{SB}(\mathbf{x}, t) = \frac{1}{4\pi} \int_S dS_y \frac{\mathbf{x} - \mathbf{y}}{|\mathbf{x} - \mathbf{y}|^3} \times [\widehat{\mathbf{n}}_y \times \mathbf{q}(\mathbf{y}, t)]. \quad (\text{A } 5)$$

1122 where $\mathbf{q}_I = \mathbf{q}_{IV} + \mathbf{q}_{IB}$, $\mathbf{q}_S = \mathbf{q}_{SV} + \mathbf{q}_{SB}$ and $\widehat{\mathbf{n}}_y$ denotes the unit surface normal at \mathbf{y} and dS_y is
 1123 the differential surface element at \mathbf{y} . For periodic vector fields $\mathbf{q}(\mathbf{x}, t)$ that are incompressible
 1124 or that can be written as the gradient of a scalar, this solution simplifies. In the case of a field
 1125 $\mathbf{q}(\mathbf{x}, t)$ which is incompressible $\nabla_x \cdot \mathbf{q}(\mathbf{x}, t) = 0$, it can be shown that $\widehat{\mathbf{q}}(\mathbf{k}, t) \cdot \mathbf{k} = 0$ for every \mathbf{k}
 1126 (Pope 2000). By inspection of (A 1), it is clear that this condition yields $\widehat{\mathbf{q}}^L(\mathbf{k}, t) = 0$ for every
 1127 \mathbf{k} such that $\widehat{\mathbf{q}}(\mathbf{k}, t) = \widehat{\mathbf{q}}(\mathbf{k}, t)^T$. By applying the Fourier transform to this relation and apply
 1128 $\mathbf{q}^T(\mathbf{x}, t) = \mathbf{q}_S(\mathbf{x}, t)$ from above, we have that $\mathbf{q}(\mathbf{x}, t) = \mathbf{q}_S(\mathbf{x}, t)$ for incompressible periodic

1129 vector fields. In the case of $\mathbf{q}(\mathbf{x}, t) = \nabla_x \psi(\mathbf{x}, t)$, where $\psi(\mathbf{x}, t)$ is some scalar field, it can be
 1130 shown that $\widehat{\mathbf{q}}(\mathbf{k}, t) = ik\widehat{\psi}(\mathbf{k}, t)$ (Pope 2000). If we insert this expression into the definition
 1131 of $\widehat{\mathbf{q}}^L(\mathbf{k}, t)$, it follows that $\widehat{\mathbf{q}}(\mathbf{k}, t) = \widehat{\mathbf{q}}^L(\mathbf{k}, t)$, which implies that $\mathbf{q}(\mathbf{x}, t) = \mathbf{q}_I(\mathbf{x}, t)$. If these
 1132 properties are combined with equations (A 2)–(A 5), we have that a periodic incompressible
 1133 vector field will have $\mathbf{q}_{IB} = \mathbf{q}_{IV} = 0$ and that a periodic vector field that can be written as a
 1134 gradient of a scalar field has $\mathbf{q}_{SB} = \mathbf{q}_{SV} = 0$.

1135 Appendix B. Irrotational and solenoidal NSD tranport terms in Fourier space

1136 We start this appendix with demonstrating that $\delta\mathbf{q}_I = \delta\mathbf{q}_I^-$ and $\delta\mathbf{q}_S = \delta\mathbf{q}_S^-$ for a periodic vector
 1137 field \mathbf{q} (see the second pararaph of section 3.3). The field \mathbf{q} has the Fourier representation

$$1138 \quad \mathbf{q}(\mathbf{x}, t) = \sum_{\mathbf{k}} \widehat{\mathbf{q}}(\mathbf{k}, t) e^{ik \cdot \mathbf{x}}, \quad (\text{B } 1)$$

1139 with the shifted fields

$$1140 \quad \mathbf{q}^+(\mathbf{x}, \mathbf{r}, t) = \mathbf{q}(\mathbf{x} + \mathbf{r}/2, t) = \sum_{\mathbf{k}} \widehat{\mathbf{q}}(\mathbf{k}, t) e^{ik \cdot (\mathbf{x} + \mathbf{r}/2)}, \quad (\text{B } 2)$$

$$1141 \quad \mathbf{q}^-(\mathbf{x}, \mathbf{r}, t) = \mathbf{q}(\mathbf{x} - \mathbf{r}/2, t) = \sum_{\mathbf{k}} \widehat{\mathbf{q}}(\mathbf{k}, t) e^{ik \cdot (\mathbf{x} - \mathbf{r}/2)}, \quad (\text{B } 3)$$

1142

1143 which have the Fourier coefficients

$$1144 \quad \widehat{\mathbf{q}}^+(\mathbf{k}, \mathbf{r}, t) = \widehat{\mathbf{q}}(\mathbf{k}, t) e^{ik \cdot \mathbf{r}/2}, \quad (\text{B } 4)$$

$$1145 \quad \widehat{\mathbf{q}}^-(\mathbf{k}, \mathbf{r}, t) = \widehat{\mathbf{q}}(\mathbf{k}, t) e^{-ik \cdot \mathbf{r}/2}. \quad (\text{B } 5)$$

1147 From the definition of the irrotational part of a vector field in (A 1), it follows

$$1148 \quad \delta\mathbf{q}_I(\mathbf{x}, \mathbf{r}, t) = \mathbf{q}_I^+(\mathbf{x}, \mathbf{r}, t) - \mathbf{q}_I^-(\mathbf{x}, \mathbf{r}, t), \quad (\text{B } 6)$$

$$1149 \quad = \sum_{\mathbf{k}} [\widehat{\mathbf{q}}_I^+(\mathbf{k}, \mathbf{r}, t) - \widehat{\mathbf{q}}_I^-(\mathbf{k}, \mathbf{r}, t)] e^{ik \cdot \mathbf{x}}, \quad (\text{B } 7)$$

$$1150 \quad = \sum_{\mathbf{k}} \frac{\mathbf{k}}{k^2} [\widehat{\mathbf{q}}(\mathbf{k}, t) \cdot \mathbf{k}] (e^{ik \cdot \mathbf{r}/2} - e^{-ik \cdot \mathbf{r}/2}) e^{ik \cdot \mathbf{x}}, \quad (\text{B } 8)$$

$$1151 \quad = \sum_{\mathbf{k}} \frac{\mathbf{k}}{k^2} [\widehat{\mathbf{q}}(\mathbf{k}, t) \cdot \mathbf{k}] 2i \sin(\mathbf{k} \cdot \mathbf{r}/2) e^{ik \cdot \mathbf{x}}. \quad (\text{B } 9)$$

1152

1153 Similarly, we can write

$$1154 \quad \delta\mathbf{q}(\mathbf{x}, \mathbf{r}, t) = \mathbf{q}^+(\mathbf{x}, \mathbf{r}, t) - \mathbf{q}^-(\mathbf{x}, \mathbf{r}, t), \quad (\text{B } 10)$$

$$1155 \quad = \sum_{\mathbf{k}} \widehat{\mathbf{q}}(\mathbf{k}, t) 2i \sin(\mathbf{k} \cdot \mathbf{r}/2) e^{ik \cdot \mathbf{x}}, \quad (\text{B } 11)$$

1156

1157 and then calculate its irrotational centroid part

$$1158 \quad \delta\mathbf{q}_I^-(\mathbf{x}, \mathbf{r}, t) = \sum_{\mathbf{k}} \frac{\mathbf{k}}{k^2} [\widehat{\mathbf{q}}(\mathbf{k}, t) \cdot \mathbf{k}] 2i \sin(\mathbf{k} \cdot \mathbf{r}/2) e^{ik \cdot \mathbf{x}}, \quad (\text{B } 12)$$

1159 which shows that $\delta\mathbf{q}_I(\mathbf{x}, \mathbf{r}, t) = \delta\mathbf{q}_I^-(\mathbf{x}, \mathbf{r}, t)$. By combining this with $\delta\mathbf{q} = \delta\mathbf{q}_I + \delta\mathbf{q}_S =$
 1160 $\delta\mathbf{q}_I^- + \delta\mathbf{q}_S^-$, we have also $\delta\mathbf{q}_S(\mathbf{x}, \mathbf{r}, t) = \delta\mathbf{q}_S^-(\mathbf{x}, \mathbf{r}, t)$, which is what we wanted to show.

1161 Next we demonstrate that $\mathbf{a}_{\Pi_I}(\mathbf{k}, \mathbf{r}, t) = \mathbf{a}_{\mathcal{T}_I}(\mathbf{x}, \mathbf{r}, t)$ in homogeneous/periodic turbulence.

1162 We list the following expressions for the vectors and tensors related to these two terms

$$1163 \quad \widehat{\delta u_j}(\mathbf{k}, \mathbf{r}, t) = 2i \sin(\mathbf{k} \cdot \mathbf{r}/2) \widehat{u}_j(\mathbf{k}, t), \quad (\text{B } 13)$$

$$1164 \quad (\widehat{u_j^+ + u_j^-})/2(\mathbf{k}, \mathbf{r}, t) = \cos(\mathbf{k} \cdot \mathbf{r}/2) \widehat{u}_j(\mathbf{k}, t), \quad (\text{B } 14)$$

$$1165 \quad \frac{\partial \widehat{\delta u_i}}{\partial r_j}(\mathbf{k}, \mathbf{r}, t) = ik_j \cos(\mathbf{k} \cdot \mathbf{r}/2) \widehat{u}_i(\mathbf{k}, t), \quad (\text{B } 15)$$

$$1166 \quad \frac{\partial \widehat{\delta u_i}}{\partial x_j}(\mathbf{k}, \mathbf{r}, t) = -2k_j \sin(\mathbf{k} \cdot \mathbf{r}/2) \widehat{u}_i(\mathbf{k}, t). \quad (\text{B } 16)$$

1168 By use of these equations, we have that the Fourier coefficients of the transport terms read

$$1169 \quad \widehat{\mathbf{a}}_{\mathcal{T}}(\mathbf{k}, \mathbf{r}, t) = \sum_{\mathbf{k}=\mathbf{k}'+\mathbf{k}''} -2 \sin(\mathbf{k}'' \cdot \mathbf{r}/2) \cos(\mathbf{k}' \cdot \mathbf{r}/2) \widehat{u}_j(\mathbf{k}') k_j'' \widehat{u}(\mathbf{k}''), \quad (\text{B } 17)$$

$$1170 \quad \widehat{\mathbf{a}}_{\Pi}(\mathbf{k}, \mathbf{r}, t) = \sum_{\mathbf{k}=\mathbf{k}'+\mathbf{k}''} -2 \sin(\mathbf{k}' \cdot \mathbf{r}/2) \cos(\mathbf{k}'' \cdot \mathbf{r}/2) \widehat{u}_j(\mathbf{k}') k_j'' \widehat{u}(\mathbf{k}''). \quad (\text{B } 18)$$

1172 Their irrotational parts are given per (A 1)

$$1173 \quad \widehat{\mathbf{a}}_{\mathcal{T}_I}(\mathbf{k}, \mathbf{r}, t) = -\frac{\mathbf{k}}{k^2} \sum_{\mathbf{k}=\mathbf{k}'+\mathbf{k}''} 2 \sin(\mathbf{k}'' \cdot \mathbf{r}/2) \cos(\mathbf{k}' \cdot \mathbf{r}/2) \widehat{u}_j(\mathbf{k}') k_j'' \widehat{u}_l(\mathbf{k}'') k_l', \quad (\text{B } 19)$$

$$1174 \quad \widehat{\mathbf{a}}_{\Pi_I}(\mathbf{k}, \mathbf{r}, t) = -\frac{\mathbf{k}}{k^2} \sum_{\mathbf{k}=\mathbf{k}'+\mathbf{k}''} 2 \sin(\mathbf{k}' \cdot \mathbf{r}/2) \cos(\mathbf{k}'' \cdot \mathbf{r}/2) \widehat{u}_j(\mathbf{k}') k_j'' \widehat{u}_l(\mathbf{k}'') k_l'. \quad (\text{B } 20)$$

1176 If we employ the trigonometric identity $\sin x \cos y = \frac{1}{2} [\sin(x+y) + \sin(x-y)]$, we get

$$1177 \quad \widehat{\mathbf{a}}_{\mathcal{T}_I}(\mathbf{k}, \mathbf{r}, t) = -\frac{\mathbf{k}}{k^2} \sum_{\mathbf{k}=\mathbf{k}'+\mathbf{k}''} [\sin(\mathbf{k} \cdot \mathbf{r}/2) + \sin(\mathbf{k}'' \cdot \mathbf{r}/2 - \mathbf{k}' \cdot \mathbf{r}/2)] \widehat{u}_j(\mathbf{k}') k_j'' \widehat{u}_l(\mathbf{k}'') k_l', \quad (\text{B } 21)$$

$$1178 \quad \widehat{\mathbf{a}}_{\Pi_I}(\mathbf{k}, \mathbf{r}, t) = -\frac{\mathbf{k}}{k^2} \sum_{\mathbf{k}=\mathbf{k}'+\mathbf{k}''} [\sin(\mathbf{k} \cdot \mathbf{r}/2) - \sin(\mathbf{k}'' \cdot \mathbf{r}/2 - \mathbf{k}' \cdot \mathbf{r}/2)] \widehat{u}_j(\mathbf{k}') k_j'' \widehat{u}_l(\mathbf{k}'') k_l'. \quad (\text{B } 22)$$

1180 Consider the term $\sin(\mathbf{k}'' \cdot \mathbf{r}/2 - \mathbf{k}' \cdot \mathbf{r}/2) \widehat{u}_j(\mathbf{k}') k_j'' \widehat{u}_l(\mathbf{k}'') k_l'$. If one adds this term with the
 1181 wavenumber triad $\mathbf{k}' = \mathbf{k}^a$ and $\mathbf{k}'' = \mathbf{k}^b \neq \mathbf{k}^a$ with the same term with the wavenumber triad
 1182 $\mathbf{k}' = \mathbf{k}^b$ and $\mathbf{k}'' = \mathbf{k}^a$ the result is zero. Furthermore, in the case of $\mathbf{k}^a = \mathbf{k}^b$ this term is zero
 1183 per incompressibility. This yields that this term does not contribute instantaneously in the
 1184 above expressions such that we attain the final result (see section 3.3 and equation (3.22))

$$1185 \quad \widehat{\mathbf{a}}_{\mathcal{T}_I}(\mathbf{k}, \mathbf{r}, t) = \widehat{\mathbf{a}}_{\Pi_I}(\mathbf{k}, \mathbf{r}, t) = -\frac{\mathbf{k}}{k^2} \sin(\mathbf{k} \cdot \mathbf{r}/2) \sum_{\mathbf{k}=\mathbf{k}'+\mathbf{k}''} \widehat{u}_j(\mathbf{k}') k_j'' \widehat{u}_l(\mathbf{k}'') k_l'. \quad (\text{B } 23)$$

1186 Appendix C. Irrotational and solenoidal dynamics in non-homogeneous 1187 turbulence

1188 Here we deduce the generalised Tsinober equations and the irrotational and solenoidal
 1189 NSD and KMH equations applicable to non-homogeneous turbulence. Consider the twice
 1190 continuously differentiable vector field vector field $\mathbf{q}(\mathbf{x}, t)$ defined on a domain $V \subseteq \mathbb{R}^3$ with

1191 the bounding surface S . This field can be uniquely decomposed into the irrotational and
1192 solenoidal vector fields

$$1193 \quad \mathbf{q}(\mathbf{x}, t) = \mathbf{q}_I(\mathbf{x}, t) + \mathbf{q}_S(\mathbf{x}, t) = -\nabla_x \phi(\mathbf{x}, t) + \nabla_x \times \mathbf{B}(\mathbf{x}, t), \quad (\text{C } 1)$$

1194 The solution to this problem under very general conditions (Sprössig 2010) is $\mathbf{q}_I = \mathbf{q}_{IV} + \mathbf{q}_{IB}$
1195 and $\mathbf{q}_S = \mathbf{q}_{SV} + \mathbf{q}_{SB}$, where the solenoidal and irrotational volume and boundary terms are
1196 given in equations (A 2)-(A 5).

1197 Consider an incompressible fluid that satisfies the incompressible vorticity equation

$$1198 \quad \nabla_y \times \left(\frac{\partial \mathbf{u}}{\partial t} + \mathbf{u} \cdot \nabla_y \mathbf{u} - \nu \nabla_y^2 \mathbf{u} - \mathbf{f} \right) = 0. \quad (\text{C } 2)$$

1199 By comparing this equation with (A 4), it is clear that the vorticity equation can be used to
1200 derive an evolution equation for the solenoidal volume parts of the NS terms. We can apply
1201 the following operator to this equation

$$1202 \quad -\frac{1}{4\pi} \int_V d\mathbf{y} \frac{\mathbf{x} - \mathbf{y}}{|\mathbf{x} - \mathbf{y}|^3} \times \left[\nabla_y \times \left(\frac{\partial \mathbf{u}}{\partial t} + (\mathbf{u} \cdot \nabla_y) \mathbf{u} - \nu \nabla_y^2 \mathbf{u} - \mathbf{f} \right) \right] = 0, \quad (\text{C } 3)$$

1203 and use (A 4) to rewrite this equation as

$$1204 \quad \left(\frac{\partial \mathbf{u}}{\partial t} \right)_{SV} + (\mathbf{u} \cdot \nabla_x \mathbf{u})_{SV} = (\nu \nabla_x^2 \mathbf{u})_{SV} + \mathbf{f}_{SV}. \quad (\text{C } 4)$$

1205 We can in a similar manner obtain the evolution equation for the irrotational volume NS
1206 terms from the Poisson equation for pressure

$$1207 \quad \frac{1}{4\pi} \int_V d\mathbf{y} \frac{\mathbf{x} - \mathbf{y}}{|\mathbf{x} - \mathbf{y}|^3} \left[\nabla_y \cdot (\mathbf{u} \cdot \nabla_y \mathbf{u} + \frac{1}{\rho} \nabla_y p - \mathbf{f}) \right] = 0, \quad (\text{C } 5)$$

1208 which yields

$$1209 \quad (\mathbf{u} \cdot \nabla_x \mathbf{u})_{IV} = \left(-\frac{1}{\rho} \nabla_x p \right)_{IV} + \mathbf{f}_{IV}, \quad (\text{C } 6)$$

1210 The equations (C 4) and (C 6) state that in all incompressible turbulent flows the solenoidal
1211 accelerations from volume contributions balance with solenoidal forces from volume con-
1212 tributions and irrotational accelerations from volume contributions balance with irrotational
1213 forces from volume contributions. The former can be viewed as an integrated vorticity
1214 equation which dictates a part of the solenoidal NS dynamics, while the latter equation
1215 as an integrated pressure Poisson equation which dictates a part of the irrotational NS
1216 dynamics. Due to the non-local character of the solenoidal and irrotational volume terms,
1217 we reformulate these equations in terms of full NS term minus boundary terms. E.g., for
1218 the time-derivative $\left(\frac{\partial \mathbf{u}}{\partial t} \right)_{SV} = \frac{\partial \mathbf{u}}{\partial t} - \left(\frac{\partial \mathbf{u}}{\partial t} \right)_{IB} - \left(\frac{\partial \mathbf{u}}{\partial t} \right)_{SB}$. The irrotational volume component
1219 (see (A 2)) involves an integral of the divergence of the respective term $(\nabla_y \cdot \mathbf{q}(\mathbf{y}))$. Thus,
1220 due to incompressibility, the time derivative and viscous terms have zero volume irrotational
1221 components, $\left(\frac{\partial \mathbf{u}}{\partial t} \right)_{IV} = (\nu \nabla_x^2 \mathbf{u})_{IV} = 0$. The solenoidal volume component (see (A 4))
1222 involves an integral of the curl of the respective term, and as the curl of the pressure gradient
1223 equals zero, this term will have a zero solenoidal volume component, $\left(-\frac{1}{\rho} \nabla_x p \right)_{SV} = 0$. We
1224 rewrite the solenoidal volume terms in equation (C 4) in terms of combinations of full terms
1225 and boundary terms to obtain

$$1226 \quad \frac{\partial \mathbf{u}}{\partial t} + ((\mathbf{u} \cdot \nabla_x) \mathbf{u})_S = \nu \nabla_x^2 \mathbf{u} + \mathbf{f}_S +$$

$$1227 \quad \left(\frac{\partial \mathbf{u}}{\partial t} \right)_{IB} - (\nu \nabla_x^2 \mathbf{u})_{IB} + \left(\frac{\partial \mathbf{u}}{\partial t} \right)_{SB} + ((\mathbf{u} \cdot \nabla_x) \mathbf{u})_{SB} - (\nu \nabla_x^2 \mathbf{u})_{SB} - \mathbf{f}_{SB}, \quad (\text{C } 7)$$

1228 where the sum of the four rightmost terms on the RHS equals $(-\frac{1}{\rho}\nabla_x p)_{SB}$ as the NS equations
1229 are satisfied at the boundary. By using this simplification and writing out all the boundary
1230 terms, we arrive at

$$1231 \quad \frac{\partial \mathbf{u}}{\partial t} + ((\mathbf{u} \cdot \nabla_x) \mathbf{u})_S = \nu \nabla_x^2 \mathbf{u} + \mathbf{f}_S$$

$$1232 \quad - \frac{1}{4\pi} \int_S dS_y \frac{\mathbf{x} - \mathbf{y}}{|\mathbf{x} - \mathbf{y}|^3} [\widehat{\mathbf{n}}_y \cdot (\frac{\partial \mathbf{u}}{\partial t} - \nu \nabla_y^2 \mathbf{u})] - \frac{1}{4\pi} \int_S dS_y \frac{\mathbf{x} - \mathbf{y}}{|\mathbf{x} - \mathbf{y}|^3} \times [\widehat{\mathbf{n}}_y \times \nabla_y \frac{1}{\rho} p]. \quad (\text{C } 8)$$

1233 By rewriting the irrotational volume components in equation (C 6) in terms of the full terms
1234 and the boundary terms, we have

$$1235 \quad ((\mathbf{u} \cdot \nabla_x) \mathbf{u})_I = -\frac{1}{\rho} \nabla_x p + \mathbf{f}_I + ((\mathbf{u} \cdot \nabla_x) \mathbf{u})_{IB} - (-\frac{1}{\rho} \nabla_x p)_{IB} - \mathbf{f}_{IB} - (-\frac{1}{\rho} \nabla_x p)_{SB}, \quad (\text{C } 9)$$

1236 where the sum of the irrotational boundary terms equals $-(\frac{\partial \mathbf{u}}{\partial t})_{IB} + (\nu \nabla_x^2 \mathbf{u})_{IB}$ by the NS
1237 equations at the boundary. If we use this relation and write out all boundary terms, we have

$$1238 \quad ((\mathbf{u} \cdot \nabla_x) \mathbf{u})_I = -\frac{1}{\rho} \nabla_x p + \mathbf{f}_I$$

$$1239 \quad + \frac{1}{4\pi} \int_S dS_y \frac{\mathbf{x} - \mathbf{y}}{|\mathbf{x} - \mathbf{y}|^3} [\widehat{\mathbf{n}}_y \cdot (\frac{\partial \mathbf{u}}{\partial t} - \nu \nabla_y^2 \mathbf{u})] + \frac{1}{4\pi} \int_S dS_y \frac{\mathbf{x} - \mathbf{y}}{|\mathbf{x} - \mathbf{y}|^3} \times [\widehat{\mathbf{n}}_y \times \nabla_y \frac{1}{\rho} p]. \quad (\text{C } 10)$$

1240 The equations (C 8) and (C 10) are generalisations of equations (3.4)-(3.5) for homo-
1241 geneous/periodic turbulence and these equations are valid for all incompressible turbulent
1242 flows. The difference from homogeneous/periodic turbulence is the collection of boundary
1243 terms

$$1244 \quad \mathbf{R}(\mathbf{x}, t) \equiv \frac{1}{4\pi} \int_S dS_y \frac{\mathbf{x} - \mathbf{y}}{|\mathbf{x} - \mathbf{y}|^3} [\mathbf{n}_y \cdot (\frac{\partial \mathbf{u}}{\partial t} - \nu \nabla_y^2 \mathbf{u})] + \frac{1}{4\pi} \int_S dS_y \frac{\mathbf{x} - \mathbf{y}}{|\mathbf{x} - \mathbf{y}|^3} \times [\mathbf{n}_y \times \nabla_y \frac{1}{\rho} p], \quad (\text{C } 11)$$

$$1245 \quad = -(\mathbf{a}_I)_{IB} + (\mathbf{a}_\nu)_{IB} - (\mathbf{a}_p)_{SB}, \quad (\text{C } 12)$$

1247 which yields the final expressions for the general irrotational and solenoidal NS equations

$$1248 \quad \frac{\partial \mathbf{u}}{\partial t} + ((\mathbf{u} \cdot \nabla_x) \mathbf{u})_S = \nu \nabla_x^2 \mathbf{u} + \mathbf{f}_S - \mathbf{R}(\mathbf{x}, t) \quad (\text{C } 13)$$

$$1249 \quad ((\mathbf{u} \cdot \nabla_x) \mathbf{u})_I = -\frac{1}{\rho} \nabla_x p + \mathbf{f}_I + \mathbf{R}(\mathbf{x}, t) \quad (\text{C } 14)$$

1251 In homogeneous/periodic turbulence all the boundary terms in $\mathbf{R}(\mathbf{x}, t)$ equal zero individ-
1252 ually (see the last paragraph of A), such that we recover equations (3.4)-(3.5). In general,
1253 the boundary terms will be non-zero and differ in different flows. E.g., at a solid wall the
1254 boundary term from the time-derivative will vanish because of no-slip and the NS equations
1255 at the wall can be used to rewrite the boundary terms as a non-local function of the pressure
1256 gradient only.

1257 The NSD irrotational and solenoidal equations in general turbulent flows are obtained by
1258 subtracting the solenoidal and irrotational NS equations (C 13)-(C 14) at $\mathbf{x} - \mathbf{r}/2$ from the
1259 same equations at $\mathbf{x} + \mathbf{r}/2$

$$1260 \quad \frac{\partial \delta \mathbf{u}}{\partial t} + \delta \mathbf{a}_{cS} = \delta \mathbf{a}_\nu + \delta \mathbf{f}_S - \delta \mathbf{R}, \quad (\text{C } 15)$$

$$1261 \quad \delta \mathbf{a}_{cI} = -\frac{1}{\rho} \nabla_x \delta p + \delta \mathbf{f}_I + \delta \mathbf{R}, \quad (\text{C } 16)$$

1262

1263 The rephrasing of the irrotational and solenoidal NSD equations in terms of the interscale
 1264 and interspace transport terms can also be performed for non-homogeneous turbulence.
 1265 We derive the centroid irrotational and solenoidal NSD equations similarly as for the NS
 1266 irrotational and solenoidal equations by starting with the NSD equation (3.9). This yields the
 1267 equations

$$1268 \quad \delta \mathbf{a}_l + \mathbf{a}_{\mathcal{T}_{\bar{S}}} + \mathbf{a}_{\Pi_{\bar{S}}} = \delta \mathbf{a}_v + \delta \mathbf{f}_{\bar{S}} - \bar{\mathbf{R}}, \quad (\text{C } 17)$$

$$1269 \quad \mathbf{a}_{\mathcal{T}_{\bar{I}}} + \mathbf{a}_{\Pi_{\bar{I}}} = \delta \mathbf{a}_p + \delta \mathbf{f}_{\bar{I}} + \bar{\mathbf{R}}, \quad (\text{C } 18)$$

1271 where

$$1272 \quad \bar{\mathbf{R}}(\mathbf{x}, \mathbf{r}, t) \equiv \frac{1}{4\pi} \int_S dS_y \frac{\mathbf{x} - \mathbf{y}}{|\mathbf{x} - \mathbf{y}|^3} [\hat{\mathbf{n}}_y \cdot (\delta \mathbf{a}_l - \delta \mathbf{a}_v)] - \frac{1}{4\pi} \int_S dS_y \frac{\mathbf{x} - \mathbf{y}}{|\mathbf{x} - \mathbf{y}|^3} \times [\hat{\mathbf{n}}_y \times \delta \mathbf{a}_p], \quad (\text{C } 19)$$

$$1273 \quad = -(\delta \mathbf{a}_l)_{IB} + (\delta \mathbf{a}_v)_{IB} - (\delta \mathbf{a}_p)_{SB}. \quad (\text{C } 20)$$

1275 These boundary terms are individually equal to zero in homogeneous/periodic turbulence
 1276 for the analogue reason as for the NS dynamics. Regarding the irrotational dynamics, in
 1277 general, $\mathbf{a}_{\mathcal{T}_{\bar{I}}} \neq \mathbf{a}_{\Pi_{\bar{I}}}$, but the irrotational volume terms are always equal, $(\mathbf{a}_{\mathcal{T}})_{IV} = (\mathbf{a}_{\Pi})_{IV}$
 1278 from equation (A 2) and

$$1279 \quad \nabla_{\mathbf{x}} \cdot \mathbf{a}_{\Pi} = \nabla_{\mathbf{x}} \cdot \mathbf{a}_{\mathcal{T}} = \frac{1}{2} \left(\frac{\partial u_k^+}{\partial x_i^+} \frac{\partial u_i^+}{\partial x_k^+} - \frac{\partial u_k^-}{\partial x_i^-} \frac{\partial u_i^-}{\partial x_k^-} \right). \quad (\text{C } 21)$$

1280 The solenoidal interscale transfer term $\mathbf{a}_{\Pi_{\bar{S}}}$ in non-homogeneous turbulence can be written
 1281 as

$$1282 \quad \mathbf{a}_{\Pi_{\bar{S}}}(\mathbf{x}, \mathbf{r}, t) = -\frac{1}{4\pi} \int_V dy \frac{\mathbf{x} - \mathbf{y}}{|\mathbf{x} - \mathbf{y}|^3} \times [\nabla_{\mathbf{y}} \times \mathbf{a}_{\Pi}(\mathbf{y}, \mathbf{r}, t)] +$$

$$1283 \quad \frac{1}{4\pi} \int_S dS_y \frac{\mathbf{x} - \mathbf{y}}{|\mathbf{x} - \mathbf{y}|^3} \times [\hat{\mathbf{n}}_y \times \mathbf{a}_{\Pi}(\mathbf{y}, \mathbf{r}, t)], \quad (\text{C } 22)$$

1284 where the surface integral is of smaller order of magnitude than the volume integral away
 1285 from boundaries and increasingly so with increasing $\langle Re_{\lambda} \rangle_t$ (verified in our periodic DNS).
 1286 Hence, for a qualitative interpretation of $\mathbf{a}_{\Pi_{\bar{S}}}$, we consider $\mathbf{a}_{\Pi_{\bar{S}}} \approx \mathbf{a}_{\Pi_{\bar{S}V}}$ with

$$1287 \quad (\nabla_{\mathbf{x}} \times \mathbf{a}_{\Pi})_i = \delta u_k \frac{\partial \delta \omega_i}{\partial r_k} - \frac{\delta \omega_k}{2} \frac{s_{ij}^+ + s_{ij}^-}{2} - \frac{\omega_k^+ + \omega_k^-}{4} \delta s_{ij} + \frac{\epsilon_{ijk}}{2} \left[\frac{\partial u_l^+}{\partial x_j^+} \frac{\partial u_k^-}{\partial x_l^-} - \frac{\partial u_l^-}{\partial x_j^-} \frac{\partial u_k^+}{\partial x_l^+} \right], \quad (\text{C } 23)$$

1288 where s_{ij} is the strain-rate tensor and ϵ_{ijk} is the Levi-Civita tensor. This set of terms
 1289 constitutes a part of the non-linear term in the evolution equation for the vorticity
 1290 difference $\delta \boldsymbol{\omega}(\mathbf{x}, \mathbf{r}, t)$, i.e. vorticity at scales $|\mathbf{r}|$ and smaller, as $\nabla_{\mathbf{x}} \times \delta \mathbf{a}_c = \nabla_{\mathbf{x}} \times (\mathbf{a}_{\Pi} + \mathbf{a}_{\mathcal{T}})$.
 1291 If one contracts (C 23) with $2\delta \boldsymbol{\omega}$, the RHS corresponds to non-linear terms which determine
 1292 the evolution of the enstrophy $|\delta \boldsymbol{\omega}|^2$ at scales smaller or comparable to $|\mathbf{r}|$. We interpret the
 1293 first term on the RHS in (C 23) as vorticity interscale transfer. By the connection to $|\delta \boldsymbol{\omega}|^2$,
 1294 we interpret the second and third terms as related to the enstrophy production/destruction
 1295 at scales smaller or comparable to $|\mathbf{r}|$ due to interactions between the vorticity and strain
 1296 fields. These three terms justify the interpretation of $\mathbf{a}_{\Pi_{\bar{S}}}$ being related non-locally in space
 1297 to vortex stretching and compression dynamics. The last term in (C 23) appears in $\nabla_{\mathbf{x}} \times \mathbf{a}_{\mathcal{T}_{\bar{S}V}}$
 1298 with a negative sign such that these terms cancel.

1299 The exact solenoidal and irrotational KMH equations follows from contracting equations

1300 (C 17)-(C 18) with $2\delta u$

$$1301 \quad \mathcal{A}_t + \mathcal{T}_{\bar{S}} + \Pi_{\bar{S}} = \mathcal{D}_{r,v} + \mathcal{D}_{X,v} - \epsilon + I_{\bar{S}} - 2\delta u \cdot \bar{\mathbf{R}}, \quad (\text{C } 24)$$

$$1302 \quad \mathcal{T}_{\bar{I}} + \Pi_{\bar{I}} = \mathcal{T}_p + I_{\bar{I}} + 2\delta u \cdot \bar{\mathbf{R}}, \quad (\text{C } 25)$$

1304 where $\mathcal{T}_{\bar{I}V} = \Pi_{\bar{I}V}$. This shows that the solenoidal and irrotational KMH equations can be
 1305 extended to non-homogeneous turbulence. In contrast to homogeneous/periodic turbulence,
 1306 in general boundary terms couple the irrotational and solenoidal dynamics.

REFERENCES

- 1307 ALVES PORTELA, F., PAPADAKIS, G. & VASSILICOS, J. C. 2020 The role of coherent structures and
 1308 inhomogeneity in near-field interscale turbulent energy transfers. *J. Fluid Mech.* **896**, A16.
- 1309 BARDINA, J., FERZIGER, J. & REYNOLDS, W. 1980 Improved subgrid-scale models for large-eddy simulation.
 1310 In *13th Fluid and Plasma Dynamics Conference*. AIAA.
- 1311 BHATIA, H., NORGARD, G., PASCUCCI, V. & BREMER, P. 2013 The Helmholtz-Hodge decomposition—a
 1312 survey. *IEEE Trans. Vis. Comput. Graph.* **19** (8), 1386–1404.
- 1313 CHEN, J. G., CUVIER, C., FOUCAUT, J.-M., OSTOVAN, Y. & VASSILICOS, J. C. 2021 A turbulence dissipation
 1314 inhomogeneity scaling in the wake of two side-by-side square prisms. *J. Fluid Mech.* **924**, A4.
- 1315 CHEN, J. G. & VASSILICOS, J. C. 2022 Scalings of scale-by-scale turbulence energy in non-homogeneous
 1316 turbulence. *J. Fluid Mech.* **938**, A7.
- 1317 CHEVILLARD, L., ROUX, S. G., LÉVÊQUE, E., MORDANT, N., PINTON, J.-F. & ARNÉODO, A. 2005 Intermittency
 1318 of velocity time increments in turbulence. *Phys. Rev. Lett.* **95** (6), 64501.
- 1319 CIMARELLI, A., ABBÀ, A. & GERMANO, M. 2019 General formalism for a reduced description and modelling
 1320 of momentum and energy transfer in turbulence. *J. Fluid Mech.* **866**, 865–896.
- 1321 DAIRAY, THIBAUT, LAMBALLAIS, ÉRIC, LAIZET, SYLVAIN & VASSILICOS, JOHN CHRISTOS 2017 Numerical
 1322 dissipation vs. subgrid-scale modelling for large eddy simulation. *J. Comput. Phys.* **337**, 252–274.
- 1323 FRISCH, U. 1995 *Turbulence: the legacy of A. N. Kolmogorov*. Cambridge University Press.
- 1324 GALANTI, B. & TSINOBER, A. 2000 Self-amplification of the field of velocity derivatives in quasi-isotropic
 1325 turbulence. *Phys. Fluids* **12** (12), 3097–3099.
- 1326 GOTO, S. & VASSILICOS, J. C. 2016 Unsteady turbulence cascades. *Phys. Rev. E* **94** (5), 53108.
- 1327 GULITSKI, G., KholmYANSKY, M., KINZELBACH, W., LÜTHI, B., TSINOBER, A. & YORISH, S. 2007 Velocity
 1328 and temperature derivatives in high-Reynolds-number turbulent flows in the atmospheric surface
 1329 layer. Part 2. Accelerations and related matters. *J. Fluid Mech.* **589**, 83–102.
- 1330 HELMHOLTZ, H. 1867 On Integrals of the hydrodynamical equations, which express vortex-motion. *Lond.*
 1331 *Edinb. Dubl. Phil. Mag.* **33** (226), 485–512.
- 1332 HILL, R. J. 2002 Exact second-order structure-function relationships. *J. Fluid Mech.* **468**, 317–326.
- 1333 HILL, R. J. & THORODDSEN, S. T. 1997 Experimental evaluation of acceleration correlations for locally
 1334 isotropic turbulence. *Phys. Rev. E* **55** (2), 1600–1606.
- 1335 KOLMOGOROV, A. N. 1941a Dissipation of energy in locally isotropic turbulence. *Dokl. Akad. Nauk SSSR*
 1336 **32**, 16–18.
- 1337 KOLMOGOROV, A. N. 1941b On the degeneration of isotropic turbulence in an incompressible viscous fluid.
 1338 *Dokl. Akad. Nauk SSSR* **31**, 538–540.
- 1339 KOLMOGOROV, A. N. 1941c The local structure of turbulence in incompressible viscous fluid for very large
 1340 Reynolds numbers. *Dokl. Akad. Nauk SSSR* **30**, 301–305.
- 1341 LESCHZNER, M. 2016 *Statistical turbulence modelling for fluid dynamics, demystified : an introductory text*
 1342 *for graduate engineering students*. Imperial College Press.
- 1343 LINKMANN, MORITZ 2018 Effects of helicity on dissipation in homogeneous box turbulence. *J. Fluid Mech.*
 1344 **856**, 79–102.
- 1345 LINKMANN, MORITZ, BUZZICOTTI, MICHELE & BIFERALE, LUCA 2018 Multi-scale properties of large
 1346 eddy simulations: correlations between resolved-scale velocity-field increments and subgrid-scale
 1347 quantities. *J. Turb.* **19** (6), 493–527.
- 1348 LINKMANN, MORITZ F & MOROZOV, ALEXANDER 2015 Sudden relaminarization and lifetimes in forced
 1349 isotropic turbulence. *Phys. Rev. Lett.* **115** (13), 134502.
- 1350 MCCOMB, W D, BERERA, A, YOFFE, S R & LINKMANN, M F 2015a Energy transfer and dissipation in forced
 1351 isotropic turbulence. *Phys. Rev. E* **91** (4), 43013.

- 1352 McCOMB, W. D., LINKMANN, M. F., BERERA, A., YOFFE, S. R. & JANKAUSKAS, B. 2015*b* Self-organization
1353 and transition to turbulence in isotropic fluid motion driven by negative damping at low wavenumbers.
1354 *J. Phys. A* **48** (25), 25FT01.
- 1355 MONIN, A. S., YAGLOM, A. M. & LUMLEY, J. L. 1975 *Statistical fluid mechanics*, , vol. 2. M.I.T. Press.
- 1356 MOSER, ROBERT D, HAERING, SIGFRIED W & YALLA, GOPAL R 2021 Statistical properties of subgrid-scale
1357 turbulence models. *Annu. Rev. Fluid Mech.* **53** (1), 255–286.
- 1358 PATTERSON, G. S. & ORSZAG, S. A. 1971 Spectral calculations of isotropic turbulence: efficient removal of
1359 aliasing interactions. *Phys. Fluids* **14** (11), 2538–2541.
- 1360 PODVIGINA, O. & POUQUET, A. 1994 On the non-linear stability of the 1:1:1 ABC flow. *Physica D* **75** (4),
1361 471–508.
- 1362 POPE, S. B. 2000 *Turbulent flows*. Cambridge University Press.
- 1363 SAGAUT, P. 2000 *Large eddy simulation for incompressible flows: an introduction*, 1st edn. Springer.
- 1364 SCHUMACHER, J., SCHEEL, J. D., KRASNOV, D., DONZIS, D. A., YAKHOT, V. & SREENIVASAN, K. R. 2014
1365 Small-scale universality in fluid turbulence. *PNAS* **111** (30), 10961–10965.
- 1366 SPRÖSSIG, W. 2010 On Helmholtz decompositions and their generalizations—an overview. *Math. Methods*
1367 *Appl. Sci.* **33** (4), 374–383.
- 1368 SREENIVASAN, K. R. & ANTONIA, R. A. 1997 The phenomenology of small-scale turbulence. *Annu. Rev.*
1369 *Fluid Mech.* **29** (1), 435–472.
- 1370 STEIROS, K. 2022 Balanced nonstationary turbulence. *Phys. Rev. E* **105** (3), 35109.
- 1371 STEWART, A. M. 2012 Longitudinal and transverse components of a vector field. *Sri Lankan J. Phys.* **12** (0),
1372 33.
- 1373 TANG, S L, ANTONIA, R A & DJENIDI, L 2022 Transport equations for the normalized nth-order moments of
1374 velocity derivatives in grid turbulence. *J. Fluid Mech.* **930**, A31.
- 1375 TENNEKES, H. 1975 Eulerian and lagrangian time microscales in isotropic turbulence. *J. Fluid Mech.* **67** (3),
1376 561–567.
- 1377 TSIINOBER, A., VEDULA, P. & YEUNG, P. K. 2001 Random Taylor hypothesis and the behavior of local and
1378 convective accelerations in asotropic turbulence. *Phys. Fluids* **13** (7), 1974–1984.
- 1379 VASSILICOS, J. C. 2015 Dissipation in turbulent flows. *Annu. Rev. Fluid Mech.* **47** (1), 95–114.
- 1380 VEDULA, P. & YEUNG, P. K. 1999 Similarity scaling of acceleration and pressure statistics in numerical
1381 simulations of isotropic turbulence. *Phys. Fluids* **11** (5), 1208–1220.
- 1382 VELA-MARTÍN, ALBERTO 2022 Subgrid-scale models of isotropic turbulence need not produce energy
1383 backscatter. *J. Fluid Mech.* **937**, A14.
- 1384 XU, H., OUELLETTE, N. T., VINCENZI, D. & BODENSCHATZ, E. 2007 Acceleration correlations and pressure
1385 structure functions in high-Reynolds number turbulence. *Phys. Rev. Lett.* **99** (20), 204501.
- 1386 YASUDA, T. & VASSILICOS, J. C. 2018 Spatio-temporal intermittency of the turbulent energy cascade. *J.*
1387 *Fluid Mech.* **853**, 235–252.
- 1388 YEUNG, P. K., POPE, S. B., LAMORGESE, A. G. & DONZIS, D. A. 2006 Acceleration and dissipation statistics
1389 of numerically simulated isotropic turbulence. *Phys. Fluids* **18** (6), 65103.